

NORTHWESTERN UNIVERSITY

Hybrid Organic Materials Comprising Polymers and Small Molecules for Biodiagnostic and  
Electronic Applications

A DISSERTATION

SUBMITTED TO THE GRADUATE SCHOOL IN PARTIAL FULFILLMENT OF THE  
REQUIREMENTS

for the degree

DOCTOR OF PHILOSOPHY

Field of Chemistry

By

Brian Richard Stepp

EVANSTON ILLINOIS

December 2008



## **Acknowledgements**

I will begin with thanking my advisor, Professor SonBinh T. Nguyen, for his guidance, perseverance, and willingness to let me explore multiple areas of interest; and for keeping me on track. I also thank the other members of my committee: Professors Frederick D. Lewis, Chad A. Mirkin, and Samuel I. Stupp for their helpful advice over the last few years. In addition I would also like to thank Professors Franz M. Geiger and George C. Schatz with whom I have had the opportunity to form fruitful collaborations.

I am grateful to all the past and current members of the Nguyen group, who have made the laboratory both enjoyable and rewarding. I especially thank Dr. Julianne M. Gibbs-Davis, with whom I have worked closely for a number of years, and all the undergrads I have had the privilege to mentor.

I am deeply indebted to my family, particularly my parents, who have always encouraged me and had faith in me. I am also indebted to my friends, both old and new, whose support is immensely appreciated.

Most importantly, I would like to thank my wife, Patricia, for keeping me grounded by making sure I occasionally stop to smell the roses, and for the love and friendship that make each day a little brighter.

## Abstract

### Hybrid Organic Materials Comprising Polymers and Small Molecules for Biodiagnostic and Electronic Applications

Brian R. Stepp

This thesis focuses on the design of hybrid organic materials comprising polymers and small molecules for biodiagnostic and electronic applications. Specifically, the electrochemical and fluorescent signaling properties of terthiophene-functionalized polymers are combined with the enhanced recognition properties of DNA hybrid materials, culminating in the development of a “loaded” probe for amplified DNA detection.

Poly(norbornene) with pendant terthiophene side chains was synthesized such that oxidative cross-linking of the terthiophene groups led to new polymeric materials with enhanced thermal stability. Films of the cross-linked material demonstrated improved surface smoothness compared to the parent poly(terthiophene), which facilitated the synthesis of multicomponent nanoscale rods synthesized by the electrochemical deposition of gold, silver, and cross-linked polymer into the pores of anodized aluminum oxide templates. Importantly, it is found that inclusion of the poly(norbornene) backbone has no negative effect on either the fluorescence or the electrochemical properties of the poly(terthiophene).

Rigid small-molecule DNA hybrids (rSMDH<sub>3</sub>'s); where three DNA strands are attached to a rigid tris(phenylacetylene) core through benzyl phosphate bonds, and flexible SMDHs (fSMDHs) with alternating poly(ethylene glycol) spacers between three DNA strands were also synthesized. Dimers of rSMDH<sub>3</sub>:rSMDH<sub>3</sub> possessing three parallel duplexes exhibited both an

increase in melting temperature (by 12 °C) and a sharp melting transition (full width at half max of the derivative curve, FWHM = 2.5 °C), while double-clips of fSMDH materials with two closely bound duplexes only showed a 5 °C increase in melting temperature. Notably, these well-defined DNA hybrid systems reveal important roles that local geometry and ion concentration play in DNA hybridization/dehybridization processes and point the way for designing new DNA-based materials with enhanced recognition properties.

Merging the signaling properties of the terthiophene materials with the recognition properties of the DNA hybrid materials allowed for the development of a “loaded” probe for amplified DNA diagnostics. Polymer nanoparticles (PNPs) assembled from amphiphilic block copolymers containing terthiophene groups were functionalized with DNA to create a PNP-DNA hybrid material which was implemented as a probe in a DNA detection assay. In comparison to the free polymer-based probe, the PNP-based probe gave signals that are amplified by at least two orders of magnitude.

## Table of Contents

Acknowledgements .....	3
Abstract .....	4
Table of Contents .....	6
List of Figures .....	13
List of Schemes .....	18
List of Schemes .....	18
List of Tables.....	19
List of Tables.....	19
<b>Chapter 1. Introduction: Examples of Hybrid Materials</b> .....	<b>20</b>
1.1. Definition of hybrid materials .....	21
1.2. Natural hybrid materials.....	21
1.2.1. Bone .....	21
1.2.2. Nacre .....	22
1.2.3. Wood.....	23
1.3. Artificial hybrid materials .....	23
1.3.1. Ancient hybrid materials .....	24
1.3.1.1. Hybrid building materials .....	24
1.3.1.2. Colored glass .....	24
1.3.1.3. Ancient dyes .....	25
1.3.1.4. Artificial bone .....	26
1.3.1.5. Dye-sensitized solar cells .....	27
1.3.1.6. DNA hybrid materials .....	28
1.4. Thesis overview .....	29

	7
<b>Chapter 2. Cross-Linked Films and Rods of Poly((2-terthiophenyl)norbornene)</b> .....	32
2.1. Background .....	33
2.1.1. Poly(thiophenes) .....	33
2.2. Enhanced properties of cross-linked poly((2-terthiophenyl)norbornene).....	35
2.2.1. Introduction .....	35
2.2.2. Results and discussion .....	36
2.2.2.1. Ring-opening metathesis polymerizations of monomer 2.1.....	36
2.2.2.2. Electrochemical and FeCl <sub>3</sub> -induced polymerization ROMP-poly1 .....	37
2.2.2.3. Visual microscopy of cross-linked films.....	38
2.2.2.4. <i>In-situ</i> conductivity measurements of cross-linked ROMP-poly1 and poly(terthiophene).....	39
2.2.2.5. Thermal gravimetric analyses of cross-linked ROMP-poly1 and poly(terthiophene).....	41
2.2.2.6. Electrochromic behavior of cross-linked ROMP-poly1 and poly(terthiophene).....	43
2.2.2.7. Optical properties of cross-linked ROMP-poly1 .....	45
2.2.2.8. Surface studies of cross-linked ROMP-poly1 and poly(terthiophene) using tapping-mode AFM.....	46
2.2.3. Conclusions.....	48
2.3. Synthesis of poly(thiophene)-derived metal-polymer nanorods using porous anodized aluminum oxide (AAO) templates.....	50
2.3.1. Introduction.....	50
2.3.1.1. Templating nanoscale rods with anodized aluminum oxide (AAO) membranes .....	50
2.3.2. Results and discussion .....	51
2.3.2.1. Synthesis of Au-polymer-Au rods.....	51
2.3.2.2. SEM characterization of Au-polymer-Au rods .....	52

2.3.2.3. Optical and fluorescence microscopy of Au-polymer-Au rods .....	8
2.3.3. Conclusion .....	53
2.4. Experimental .....	57
2.4.1. General considerations and instrumentation .....	58
2.4.2. Materials.....	59
2.4.3. Conditions for ROMP of 2.1.....	60
2.4.4. Oxidative cross-linking of ROMP-poly1 and polymerization of terthiophene with FeCl <sub>3</sub> .....	60
2.4.5. Electrochemical cross-linking of ROMP-poly1 and polymerization of terthiophene.....	61
2.4.6. <i>In-situ</i> conductivity measurements of cross-linked films .....	61
2.4.7. Thermal gravimetric analysis (TGA) of poly(terthiophene) and ROMP-poly1 materials.....	62
2.4.8. Electrochemical doping of cross-linked ROMP-poly1 and poly(terthiophene) with ClO <sub>4</sub> <sup>-</sup> .....	63
2.4.9. Fluorescence microscopy imaging of cross-linked ROMP-poly1 and poly(terthiophene).....	63
2.4.10. Fluorescence spectra of cross-linked ROMP-poly1 and poly(terthiophene) .....	63
2.4.11. Atomic force microscopy.....	63
2.4.12. General synthesis of Au-polymer-Au rods .....	64
<b>Chapter 3. Small Molecule-DNA Hybrids .....</b>	<b>65</b>
3.1. Aggregates of DNA hybrid materials .....	66
3.1.1. Background.....	66
3.1.2. Melting properties of DNA hybrid aggregates.....	67
3.1.3. Use of SMDHs to elucidate factors affecting enhanced melting .....	69
3.2. Benzyl phosphate-linked rigid small molecule-DNA hybrids.....	71



	9
3.2.1. Introduction .....	71
3.2.1.1. Aggregates of rSMDH <sub>3</sub> -enhanced melting by design .....	72
3.2.2. Results and discussion .....	73
3.2.2.1. Synthesis of rSMDH <sub>3</sub> hybrids .....	73
3.2.2.2. Hybridization and melting of rSMDH <sub>3</sub> aggregates .....	74
3.2.2.3. The number of cooperative duplexes in rSMDH aggregates .....	76
3.2.3. Conclusions .....	77
3.3. Synthesis and melting properties of flexible SMDHs .....	78
3.3.1. Introduction .....	78
3.3.1.1. Flexible SMDHs .....	79
3.3.2. Results and discussion .....	80
3.3.2.1. Synthesis of fSMDHs .....	80
3.3.2.2. Melting experiments .....	81
3.3.3. Conclusions .....	84
3.4. Triazole-linked rigid small molecule-DNA hybrids .....	85
3.4.1. Introduction .....	85
3.4.1.1. Triazole-linked rSMDHs .....	85
3.4.2. Results and discussion .....	86
3.4.2.1. Synthesis of core molecules .....	86
3.4.2.1.1. Synthesis of acetylene arm 3.23 .....	86
3.4.2.1.2. Coupling to acetylene arm 3.23 .....	87
3.4.2.2. DNA attachment .....	88
3.4.3. Conclusion and future work .....	88
3.5. Experimental .....	89

3.5.1. General procedures, materials, and instrumentation .....	10
3.5.2. Synthesis .....	89
3.5.3. Melting experiments (Section 3.2).....	91
3.5.4. Demonstration of rSMDH <sub>3</sub> dimer formation by PAGE analysis.....	104
3.5.5. Determining the number of cooperative duplexes N <sub>c</sub> for rSMDH <sub>3</sub> aggregates .....	104
3.5.6. Melting experiments for Section 3.3.....	105
<b>Chapter 4. Terthiophene-Based Polymer Nanoparticle Probes for DNA Detection .....</b>	<b>106</b>
4.1. DNA detection and signal amplification.....	108
4.2. Assembly of fluorescent/electrochemically active terthiophene-containing amphiphilic polynorbornenes into labeled polymer nanoparticles .....	110
4.2.1. Introduction .....	110
4.2.1.1. Eisenberg strategy for the synthesis of PNPs from amphiphilic block copolymers.....	110
4.2.1.2. Payload-containing PNPs.....	111
4.2.2. Results and discussion .....	112
4.2.2.1. Synthesis of block copolymers TTT <sub>m</sub> - <i>b</i> -(PEG-OTs) <sub>n</sub> .....	112
4.2.2.2. Fluorescence studies of terthiophene-containing materials .....	113
4.2.3. Electrochemical studies of terthiophene-containing materials .....	114
4.2.4. PNP assembly .....	115
4.2.4.1. Solvent optimization for the assembly of PNPs.....	115
4.2.4.2. Optimization of polymer loading in solutions for used for the formation of PNPs.....	117
4.2.4.3. Stability of PNPs .....	118
4.2.5. Surface modification .....	119
4.2.6. Conclusions.....	120

	11
4.3. Labeled polymer nanoparticles as “loaded” probes for DNA detection .....	122
4.3.1. Introduction .....	122
4.3.2. Loaded Probes .....	122
4.3.3. Results and discussion .....	123
4.3.3.1. PNP probe formation.....	123
4.3.3.2. DNA detection with PNP-based probes .....	124
4.3.4. Conclusions .....	126
4.4. Experimental .....	127
4.4.1. General considerations .....	127
4.4.2. Materials.....	128
4.4.3. General polymer synthesis .....	129
4.4.4. Fluorescence of terthiophene, monomer 2.1, and polymer TTT <sub>60</sub> - <i>b</i> -(PEG-OTs) <sub>15</sub> .....	130
4.4.5. Electrochemistry of terthiophene, monomer 2.1, and polymer TTT <sub>60</sub> - <i>b</i> -(PEG-OTs) <sub>15</sub> .....	130
4.4.6. General preparation of PNPs.....	130
4.4.7. Functionalization of PNPs with ethidium bromide monoazide .....	131
4.4.8. General procedure for the preparation of DNA-functionalized PNPs .....	132
4.4.9. Preparation of DNA modified TTT <sub>60</sub> - <i>b</i> -(PEG-OTs) <sub>15</sub> .....	133
4.4.10. DNA Detection using PNP and polymer probes.....	133
<b>Chapter 5. Epilogue .....</b>	<b>134</b>
5.1. Summary and outlook for chapter 2.....	135
5.2. Summary and outlook for chapter 3.....	136
5.3. Summary and outlook for chapter 4.....	137
References .....	139

Chapter 1 .....	12
Chapter 1 .....	140
Chapter 2 .....	142
Chapter 3 .....	146
Chapter 4 .....	149
Chapter 5 .....	151
Curriculum Vitae.....	152

## List of Figures

### Chapter 1

- Figure 1.1.** Left: A cut away image of a nautilus shell, showing the iridescent nacre.<sup>3</sup> Right: A scanning electron microscopy (SEM) image of a fractured abalone shell showing offset aragonite platelets. .... 22
- Figure 1.2.** Left: A diagram showing the various orientations of fibers in the multiple layers of a tree's cell wall. Right: An SEM image with arrow pointing to a break between two cell wall layers where fiber orientation is easily observed. .... 23
- Figure 1.3.** Images of the Lycurgus Chalice with reflected (a), and transmitted (b) light. .... 25
- Figure 1.4.** Left: An image of a mural representing a quetzal made using Maya blue. Right: A diagram of the structure of Maya blue showing indigo molecules intercalated into the palygorskite matrix. .... 26
- Figure 1.5.** SEM image of nucleating hydroxyapatite crystals on a peptide amphiphile nanofiber matrix, templated by titanium foam. .... 27
- Figure 1.6.** Left: The solar radiation spectrum, showing a peak intensity at ~500 nm. Right: The incident photon-to-current efficiencies (IPEC) for TiO<sub>2</sub> and two Ru<sup>+2</sup>(bpy)<sub>3</sub> derivatives. More substantial overlap of the solar radiation spectrum is observed for the Ru<sup>+2</sup>(bpy)<sub>3</sub> derivatives compared to TiO<sub>2</sub>. .... 28

### Chapter 2

- Figure 2.1.** a) A three-dimensional growth model for poly(thiophene) proposing that it is kinetically favored that oligomeric monomer units (M) join a growing nucleus of poly(thiophene) as they precipitate from solution. b) An SEM image of a poly(thiophene) nucleus formed on an electrode surface. .... 34
- Figure 2.2.** A proposed two-dimensional growth mechanism for films of cross-linked poly((2-terthiophenyl)norbornene): extended polymer chains bring multiple terthiophene groups to the surface over a larger area than that of native terthiophene, resulting in smoother films on the electrode surface. .... 35
- Figure 2.3.** The number-average molecular weight (M<sub>n</sub>) for **ROMP-poly1** polymers plotted against the monomer-to-catalyst ratio. .... 36

- Figure 2.4.** a) Films of **ROMP-poly1** are electrochemically cross-linked on ITO-coated glass by repeated scanning from  $-0.35$  to  $1.27$  V (red traces) and  $-0.35$  to  $1.80$  V (black traces). Peak current increases and peak potential shifts as subsequent layers (1-3) are deposited. b) A 3-layer film of cross-linked **ROMP-poly1** (deposited on ITO-coated glass) is electrochemically cycled at  $0.1$  V/s,  $0.5$  V/s, and  $1$  V/s in  $[0.1$  M TBAPF<sub>6</sub>/CH<sub>2</sub>Cl<sub>2</sub>]. Increasing the rate attenuates ion mobility in and out of the film, thereby increases peak-to-peak separation. .... 38
- Figure 2.5.** Optical (left column, 50x magnification, differential interference contrast (DIC) mode) and fluorescence (right column, excitation 533-587 nm and emission 608-668 nm) microscopic images show that films of **ROMP-poly1** generated between  $0.0$  and  $1.27$  V (a and b) are more uniform than those generated between  $0.0$  and  $1.80$  V (c and d). .... 39
- Figure 2.6.** *In-situ* conductivity plots of poly(terthiophene) and cross-linked **ROMP-poly1** versus doping potential. The inset plots show the difference in turn-on voltages for poly(terthiophene) and cross-linked **ROMP-poly1**. The drops in conductivity after  $1.25$  V are a consequence of over-oxidation. .... 40
- Figure 2.7.** (a) TGA curves for powders of poly(terthiophene) prepared by FeCl<sub>3</sub>-induced polymerization, three **ROMP-poly1** samples of different chain-lengths (monomer/catalyst ratio of 20, 50, and 100), and the corresponding cross-linked polymers prepared by FeCl<sub>3</sub>-induced polymerization. (b) TGA results illustrating the effect of incomplete drying for a powder sample of cross-linked 50-mer **ROMP-poly1** prepared by FeCl<sub>3</sub>-induced polymerization. (c) TGA curves illustrating the effect of re-exposing a powder sample of cross-linked 50-mer **ROMP-poly1** prepared by FeCl<sub>3</sub>-induced polymerization to MeOH followed by drying over different periods of time. (d) TGA results for 50-layer films of electrochemically cross-linked 50-mer **ROMP-poly1** and polyterthiophene on Au/Si substrates. .... 42
- Figure 2.8.** A three-layer film of electrochemically cross-linked 20-mer **ROMP-poly1** changes from orange (left) to dark blue (right) in a perchlorate-containing electrolyte as the cell voltage is increased from  $-0.35$  to  $1.27$  V. This dopant-induced color change is reversible over 20 or more cycles. .... 44
- Figure 2.9.** Current-voltage plots of two separate 3-layer films comprised of electrochemically cross-linked 20-mer **ROMP-poly1** immersed in methylene chloride containing  $0.1$  M tetrabutylammonium perchlorate. (a) Due to overoxidation, peak current decreases with each subsequent cycle when one film is scanned between  $-0.35$  and  $1.80$  V. (b) The I-V behavior remains constant over 5 cycles when another identical film is scanned between  $-0.35$  and  $1.27$  V. .... 44

- Figure 2.10.** Digital images of 3-layer films of poly(terthiophene) (top row) and **ROMP-poly1** (bottom row) taken from fluorescence microscopy experiments. a) Ex. 340-380 nm, Em. No Filter. b) Ex. 340-380 nm, Em. 435-485 nm. c) Ex. 460-500 nm, Em. 510-560 nm. d) Ex. 533-587 nm, Em. 608-668 nm. e) Ex. 340-380 nm, Em. 510-560 nm. .... 45
- Figure 2.11.** The UV-vis (a) and emission (b) spectra for 3-layer films of poly(terthiophene) and **ROMP-poly1** that have been deposited on an ITO electrode were very similar. Fluorescence spectra were taken using excitation wavelengths of 322 nm, 366 nm, and 418 nm. .... 46
- Figure 2.12.** AFM images of electrochemically prepared: (a) cross-linked 30-mer **ROMP-poly1** film deposited between  $-0.35$  and  $1.27$  V (inset with reduced z-range to show detail), (b) cross-linked 30-mer **ROMP-poly1** film deposited between  $-0.35$  and  $1.80$  V, (c) poly(terthiophene) film deposited between  $-0.35$  and  $1.27$  V, and (d) poly(terthiophene) film deposited between  $-0.35$  and  $1.80$  V. Each film is the result of three deposition scans. .... 47
- Figure 2.13.** SEM images of: A-C) Rods containing poly(thiophene) showing disjointed junctions which are not well-attached to the gold. D-F) Rods containing cross-linked **ROMP-poly1** are more continuous and show very little breakage between the polymer and the gold segments. .... 53
- Figure 2.14.** Optical (left column) and fluorescence (right column) microscopy images taken from the side of a small bundle of rods (top row) and from the top of a large sheet (bottom row). As a visual guide, the bundles of rods are outlined in the fluorescence microscopy images. .... 54
- Figure 2.15.** Black-and-white time-lapse fluorescence microscopy images taken from the top of a large sheet of bundled rods (5 frames per second), demonstrating the observed fluorescence “blinking.” .... 55
- Figure 2.16.** Three continuous time-lapse fluorescence microscopy images taken from the top of a large sheet of Au-polymer-Au rods (5 frames per second), demonstrating the observed fluorescence “skipping” from site 1 to 2 and from site 2 to 3. Lines at the edge of the images mark each fluorescent site. .... 56

### Chapter 3

- Figure 3.1** Distinct sharpening of the melting profiles between free DNA (A) and aggregates of GNP-DNA hybrids (B). In each graph the red curve is for an SNP-containing DNA duplex, and the black curve is perfectly complementary (Figure adapted from Taton et al. *Science* **2000**, 289, 1757-1760). .... 68

	16
<b>Figure 3.2.</b> Structure of our polymer precursor to the polymer-DNA hybrid prior to DNA coupling to the pendant phosphoramidites. The side chain contains the rigid diphenylacetylene linker found in the rigid small molecule-DNA hybrids (Figure 3.3). .....	71
<b>Figure 3.3.</b> Examples of rigid small-molecule-DNA hybrids (rSMDHs). .....	72
<b>Figure 3.4.</b> Melting curves for rSMDH <sub>3</sub> :rSMDH <sub>3</sub> hybridization mixtures at high (3.80 μM) and low (0.38 μM) concentrations in saline buffer (10 mM PBS, pH = 7.0, 150 mM NaCl). Inset: First derivatives of the melting curves. ....	75
<b>Figure 3.5.</b> Digital images of the non-denaturing PAGE gel of rSMDH hybridization mixtures. Right: Grayscale image; Left: Black-and-white image with background subtraction. Lane 1: A:B rSMDH cage dimers formed in dilute solution. Lane 2: Purified non-hybridized rSMDH-A. Lane 3: Crude sample of non-hybridized rSMHD-A before purification. Lane 4: A:B rSMDH aggregates formed in concentrated solution. ....	76
<b>Figure 3.6.</b> Four DNA duplexes (colored waves) held together by flexible linkers (black lines), and the proposed melting curves of the free duplexes and the four-duplex aggregate. ....	79
<b>Figure 3.7.</b> Two length variants of commercially available PEG-phosphoramidites for use in solid-phase synthesis of spacer-interrupted DNA strands. ....	80
<b>Figure 3.8.</b> Twelve DNA sequences synthesized for use in the fSMDH studies. ....	81
<b>Figure 3.9.</b> Melting profile of four-duplex aggregate comprised of <b>3.9</b> , <b>3.10</b> , <b>3.11</b> , and <b>3.14</b> . ....	83
<b>Figure 3.10</b> Library of synthesized rSMDH core molecules, possessing a range of substitution densities and spacing. ....	88
<b>Figure 3.11.</b> Digital images of denaturing PAGE gels following the purification of rSMDH <sub>3</sub> materials after successive dialysis runs. Top row: rSMDH <sub>3</sub> -B; Bottom row: rSMDH <sub>3</sub> -A. Column 1: Unmodified image of crude rSMDH <sub>3</sub> products. Column 2: Unmodified image of rSMDH <sub>3</sub> 's after dialyzing through 8-K MWCO tubes. Column 3: Grayscale-inversion image of rSMDH <sub>3</sub> after dialyzing through 8-K MWCO tubes. Column 4: Black-and-white conversion image of rSMDH <sub>3</sub> after dialyzing through 8-K MWCO tubes. Column 5: Modified image (with background subtracted from black-and-white conversion image) of rSMDH <sub>3</sub> after dialyzing through 8-K MWCO tubes. Column 6: Modified image after dialyzing through 15-K MWCO tubes. Column 7: Modified image after dialyzing through 25-K MWCO tubes. ....	98



	17
<b>Figure 3.12.</b> MALDI-TOF mass spectrum of purified rSMHD <sub>3</sub> , showing product peak and two major fragmentations peaks due to loss of 1 or 2 DNA strands. ....	99

## Chapter 4

<b>Figure 4.1.</b> A typical DNA detection sandwich assay where a fully complimentary DNA duplex is formed via a surface-bound capture strand recruiting a target strand to the surface and the subsequent engagement of a probe-linked strand. A subsequent signaling event will allow a macroscale readout of this detection process; however, in such a case each detection event will yield only a single signal. ....	109
<b>Figure 4.2.</b> The fluorescence spectra of chloroform solutions of terthiophene, monomer <b>4.1</b> , and block copolymer TTT <sub>60</sub> - <i>b</i> -(PEG-OTs) <sub>15</sub> . ....	114
<b>Figure 4.3.</b> Cyclic voltammograms of terthiophene, monomer <b>4.1</b> , and block copolymer TTT <sub>60</sub> - <i>b</i> -(PEG-OTs) <sub>15</sub> after nine cycles between 0.0 and 1.30 V. ....	115
<b>Figure 4.4.</b> Static light-scattering data taken during water addition to solutions of TTT <sub>60</sub> - <i>b</i> -(PEG-OTs) <sub>15</sub> (0.010 wt%) in THF and DMF. ....	116
<b>Figure 4.5.</b> TEM images of two different dried PNP solutions before (left column) and after centrifugation (right column, 20 min at 1000 rpm). A and B are of TTT <sub>45</sub> - <i>b</i> -(PEG-OTs) <sub>15</sub> , while C and D are of TTT <sub>60</sub> - <i>b</i> -(PEG-OTs) <sub>15</sub> . ....	118
<b>Figure 4.6.</b> Fluorescence spectra of DMF solutions of bare PNPs and ethidium-modified PNPs. ....	120
<b>Figure 4.7.</b> Fluorescence microscopy images of unmodified PNPs and ethidium-modified PNP after being dissolved in DMF and dried. ....	120
<b>Figure 4.8.</b> TEM images of PNP Probes (large gray spheres) with complementary (left) and non-complementary (right) DNA-GNPs (small black spheres). ....	124
<b>Figure 4.9.</b> Glass slides with either one or two spherical depressions (16 mm diameter; 0.50 mm depth) for holding liquid samples. ....	125
<b>Figure 4.10.</b> Fluorescence microscopy images following sandwich assays using glass slides with bound capture strands, 100 pM target DNA, and either PNP probes (Left) or polymer probes (Right). After dissolving probes in methylene chloride, solvent is allowed to dry and a polymer film is formed which is subsequently viewed by fluorescence microscopy. ....	125

## List of Schemes

### Chapter 2

- Scheme 2.1.** Synthesis of Au-Polymer-Au rods comprising either poly(thiophene) or cross-linked **ROMP-poly1** using an AAO template. .... 52

### Chapter 3

- Scheme 3.1.** Two aggregate pathways for mixture of complementary rSMDH<sub>3</sub> molecules: rSMDH-A and rSMDH-B. .... 73
- Scheme 3.2.** Synthesis of rSMDH<sub>3</sub>. .... 74
- Scheme 3.3.** Proposed triazole “click” chemistry linkage. .... 86
- Scheme 3.4.** Proposed synthesis route of the desired core molecule library. .... 87

### Chapter 4

- Scheme 4.1.** The Eisenberg strategy for inducing the self-assembly of an amphiphilic block copolymer into a polymer nanoparticle. .... 111
- Scheme 4.2.** Reaction scheme for the general synthesis of a TTT<sub>m</sub>-*b*-(PEG-OTs)<sub>n</sub> block copolymer. .... 113
- Scheme 4.3.** In a sandwich assay similar to that described in Figure 4.1, a PNP probe is brought to the surface through duplex formation with capture and a target strand. Unbound probes are washed away with aqueous rinses, and the PNPs are dissolved in organic solvent. As thousands of TTT groups are contained in a single PNP, one binding event should lead to amplified signal. .... 123

## List of Tables

### Chapter 2

<b>Table 2.1.</b>	Root-mean-square (rms) of roughness values of cross-linked <b>ROMP-poly1</b> and poly(terthiophene) films on ITO-coated glass. Each film is the result of three deposition scans. ....	47
<b>Table 2.2.</b>	Polymer characterization data for the ROMP of <b>2.1</b> . ....	60

### Chapter 3

<b>Table 3.1.</b>	Melting data for unmodified DNA (DNA:DNA) and rSMDH <sub>3</sub> (rSMDH <sub>3</sub> :rSMDH <sub>3</sub> ) aggregates. ....	75
<b>Table 3.2.</b>	Summary of melting data for free duplexes and the four-duplex aggregates. ....	83
<b>Table 3.3.</b>	Melting data for unmodified DNA (DNA:DNA) duplexes and rSMDH <sub>3</sub> (rSMDH <sub>3</sub> :rSMDH <sub>3</sub> ) aggregates. ....	106

### Chapter 4

<b>Table 4.1.</b>	Copolymer synthesis and analysis. ....	113
<b>Table 4.2.</b>	Synthetic and characterization data for the PNPs used in this study. ....	117

## **Chapter 1**

### **Introduction: Examples of Hybrid Materials**

## 1.1. Definition of hybrid materials

Hybrid materials are generally defined as “materials that include two moieties blended on the molecular scale.”<sup>1</sup> As this definition is quite broad, the brief review presented herein concentrates on a few natural and artificial materials whose advanced properties arise from chemically linking components from two or more traditional classes of materials.

## 1.2. Natural hybrid materials

In the synthesis of its myriad materials, nature employs many diverse building blocks including metals, metal oxides, polymers, and small organic compounds. Each of these component materials impart specific advantages; however, in the biological realm it is rare that any of are found alone, as the properties of one are often enhanced by, if not reliant on, the inclusion of another.

### 1.2.1. Bone

While the most palpable functions of bone are support and protection of vital organs, bone is also critical in the production of new blood cells and acts as a reservoir for calcium, phosphate, and other ions. The versatility of bone is made possible by the intrinsic interactions between its main components; hydroxyapatite ( $\text{Ca}_2(\text{PO}_4)_3\text{OH}$ , 43%) and type-I collagen (a fibrous protein triple helix, 36%), with the remainder comprised of bone matrix proteins and osteocyte cells.

As the main constituents of bone, the rigid inorganic mineral hydroxyapatite and the flexible biopolymer collagen hybridize into a composite with remarkable elasticity and tensile strength. The importance of having both of these orthogonal properties in one material, is emphasized by the disease *osteogenesis imperfecta*,<sup>2</sup> or brittle bone disease, which results in easily broken bones due to low collagen production. From a materials point-of-view,

*osteogenesis imperfecta* offsets the delicate balance between the inorganic and biopolymer components, leading to bones that are too high in mineral content and thus too rigid to absorb significant shock.

### 1.2.2. Nacre

A second naturally occurring hybrid material is nacre, or mother of pearl, which many families of mollusk form as shells to protect the delicate tissue of these organisms (Figure 1.1, left panel). Similar to bone, nacre is both strong and resilient despite being composed almost entirely (>96%) of the weak ceramic calcium carbonate, commonly known as chalk, with the remainder being chitin and proteins. The hexagonal calcium carbonate platelets, in the form of aragonite, are stacked in offset layers (Figure 1.1, right panel) that are held together by an organic matrix. This brick-like pattern is important in preventing crack propagation, while glycine- and alanine-rich proteins act as glue between the layers, and chitin provides toughness to the composite.

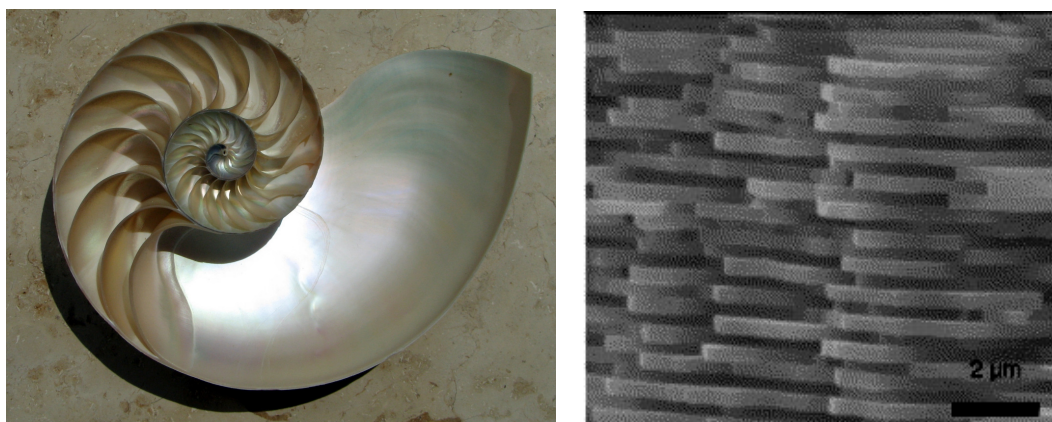


**Figure 1.1.** Left: A cut-away image of a nautilus shell, showing the iridescent nacre.<sup>3</sup> Right: A scanning electron microscopy (SEM) image of a fractured abalone shell showing offset aragonite platelets.<sup>4</sup>

### 1.2.3. Wood

Unlike animals, plants do not use skeletons or shells of inorganic minerals for structural support; yet many tree species can grow over 100 ft in height. This towering feat is based on an entirely organic hybrid material, wood, which makes up the cell walls of trees and is composed of cellulose fibers and phenolic small molecules known as lignin. Cellulose is a polymer of  $\beta$ -(D)-glucose that can hydrogen-bond together to form macroscopic fibers. In wood, these fibers are specifically oriented to withstand both compression and tension (Figure 1.2); however, the fibers would easily separate and splinter without the adhesion properties of the resinous lignin. This process has been closely imitated by man through the inclusion of graphite fibers in an epoxy matrix, which has found numerous commercial uses, especially in sports equipment and transportation vehicles.

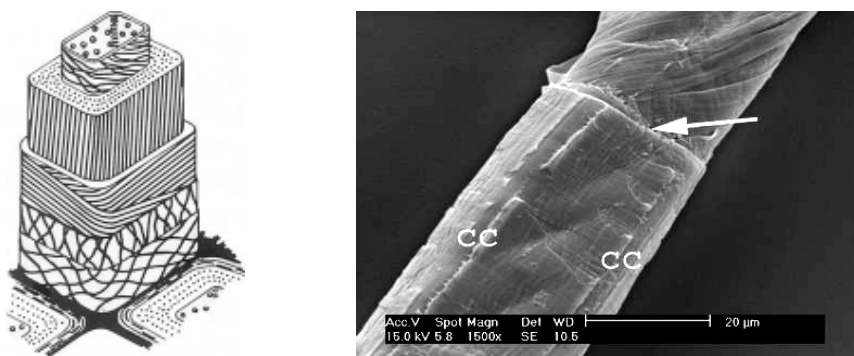


**Figure 1.2.** Left: A diagram showing the various orientations of fibers in the multiple layers of a tree's cell wall.<sup>5</sup> Right: An SEM image with arrow pointing to a break between two cell wall layers where fiber orientation is easily observed.<sup>6</sup>

### 1.3. Artificial hybrid materials

Similar to their natural occurring analogues, the advantage of manmade hybrid materials is that the composite often have enhanced properties over those of the individual parts. From the simplicity of the mud-and-grass used in housing construction to the complexity of

macromolecular engineering, hybrid materials have been an enduring element in mankind's quest for survival and improvement of their surroundings.

### **1.3.1. Ancient hybrid materials**

#### **1.3.1.1. Hybrid building materials**

Originating in prehistoric times and still in-use today, adobe, cob, and mudbrick are all straightforward examples of artificial hybrid materials. With compositions functionally similar to the nacre discussed in section 1.2.2, each of these building materials consists of an inorganic component such as clay, which provides both structural adhesion and solidity, and an organic constituent like straw, which forms a reinforcing matrix to strengthen the composite. While the individual components are not stable for long periods of time, buildings made from these hybrid materials have stood for thousands of years

#### **1.3.1.2. Colored glass**

Dating back to the 4<sup>th</sup> Century A.D., the Lycurgus Chalice is among the earliest artifacts made from an artificial hybrid material (Figure 1.3). Interestingly, the glass used to make the chalice appears jade green in reflected light and translucent red when light is shone directly through the glass. This unusual optical effect is caused by the presence of small amounts of gold (40 ppm) and silver (300 ppm) within the glass in the form of alloy nanoparticles ~70 nm in diameter.<sup>7</sup> The glass matrix suspends the colloidal particles, allowing them to scatter light and results in the remarkable optical properties of the glass.



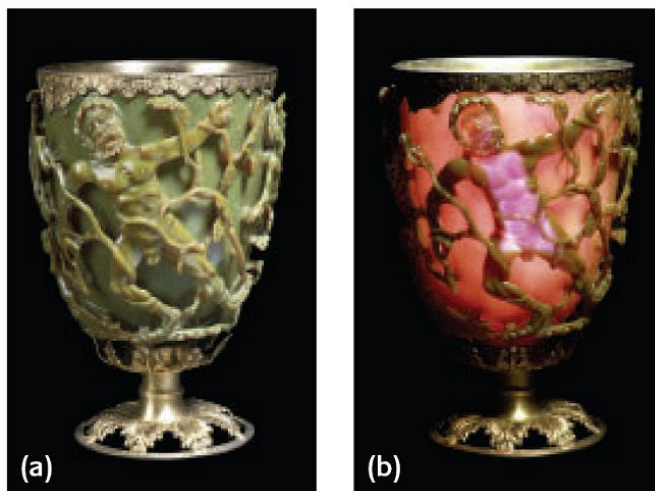


**Figure 1.3.** Images of the Lycurgus Chalice with reflected (a), and transmitted (b) light.<sup>7</sup>

### 1.3.1.3. Ancient dyes

A third ancient hybrid material is the dye Maya blue, developed by the cultures of pre-Columbian Mesoamerica as early as A.D. 500. Composed mainly of the clay palygorskite and intercalated indigo molecules, Maya blue was used in murals such as those at Bonampak and has retained its vibrancy well over a thousand years despite the harsh tropical environment of the Yucatán peninsula (Figure 1.4).<sup>8</sup> Outside of the protective clay matrix, indigo would readily decompose; however, the hybrid material is so stable that refluxing nitric acid is required to destroy it.

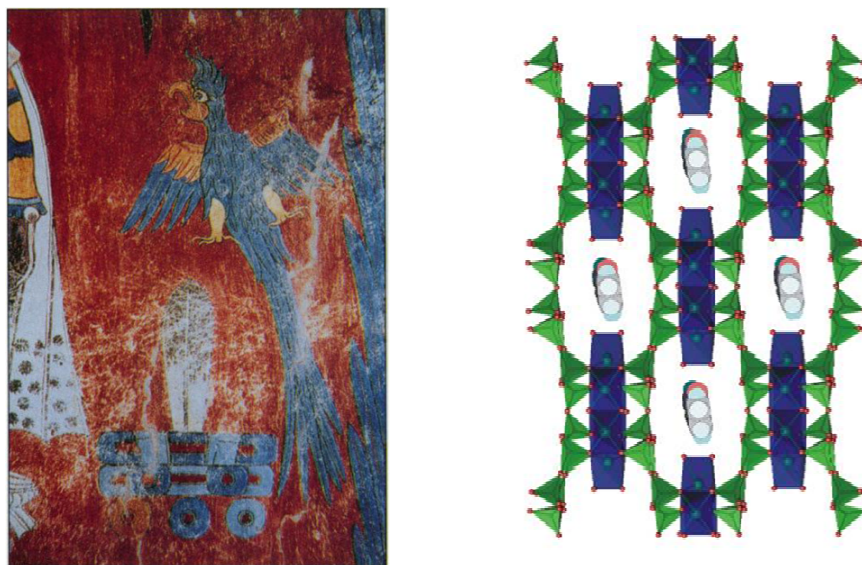


**Figure 1.4.** Left: An image of a mural depicting a quetzal made using Maya blue. Right: A diagram of the structure of Maya blue showing indigo molecules intercalated into the palygorskite matrix.<sup>8</sup>

#### 1.3.1.4. Artificial bone

The Stupp group recently reported a method to prepare a hybrid bone implant material consisting of a titanium foam whose pores were filled with matrix of a peptide amphiphile (PA) nanofibers.<sup>9</sup> The self-assembling PA nanofibers are biologically active by design, and are used to transform the inert titanium foam into a bioactive implant. In an *in vivo* experiment, a titanium foam plug was inserted into the femur of a rat, followed by injection of a PA solution. After four weeks of growth, analysis of these hybrid implants showed that the PA molecules have self-assembled into a nanofiber matrix within the pores of the metallic foam; fully occupying the interconnected porosity. Importantly, there was no cytotoxic response; and unlike contemporary implants, the nanofiber matrix nucleated mineralization of hydroxyapatite crystals to unify the hybrid implant with naturally growing bone (Figure 1.5).

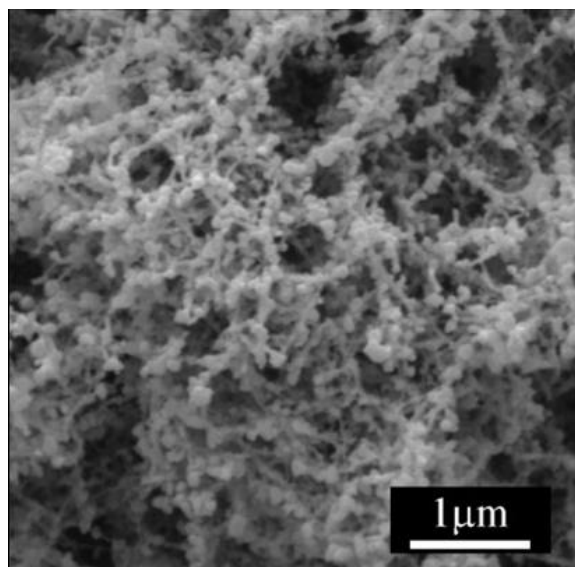


**Figure 1.5.** SEM image of nucleating hydroxyapatite crystals on a matrix of peptide amphiphile nanofibers templated by titanium foam.<sup>9</sup>

#### 1.3.1.5. Dye-sensitized solar cells

One promising technology for capturing solar energy and converting it to useful electricity is the dye-sensitized solar cell (DSC), which combines dyes, such as the coordination complex ruthenium trisbipyridine ( $\text{Ru}^{+2}(\text{bpy})_3$ ) and its derivatives, with inorganic semiconductor nanoparticles, such as titanium dioxide ( $\text{TiO}_2$ ) to make efficient low-cost solar cells.<sup>10</sup> Upon irradiation, the inexpensive semiconductor  $\text{TiO}_2$  can successfully split an electron-hole pair and inject the electron into a circuit to give an electrical current. Unfortunately, the excitation energy required to effect this process in  $\text{TiO}_2$  is relatively high and can only be provided by a narrow portion of the solar spectrum (Figure 1.6), significantly wasting a wide range of energy. In contrast, derivatives of  $\text{Ru}^{+2}(\text{bpy})_3$  can absorb over a large portion of the solar spectrum and can inject photoelectrons into the conduction band of a semiconductor. However, they are limited by a low cross-sectional absorptivity that necessitates a large number of molecules to efficiently absorb light, leading to prohibitively higher costs. In DSCs the  $\text{TiO}_2$  nanoparticles serve double-

duty, acting as a scaffold to hold large numbers of the dye molecules in a 3-D matrix, thereby increasing the solar absorptivity of the solar cell, and as the semiconductor. The resulting hybrid DSC materials rectify the intrinsic shortcomings of each component, permit the fabrication of relatively efficient (11%) solar cells, and hold promise for use in low-cost applications where silicon-based solar cells are uneconomical.

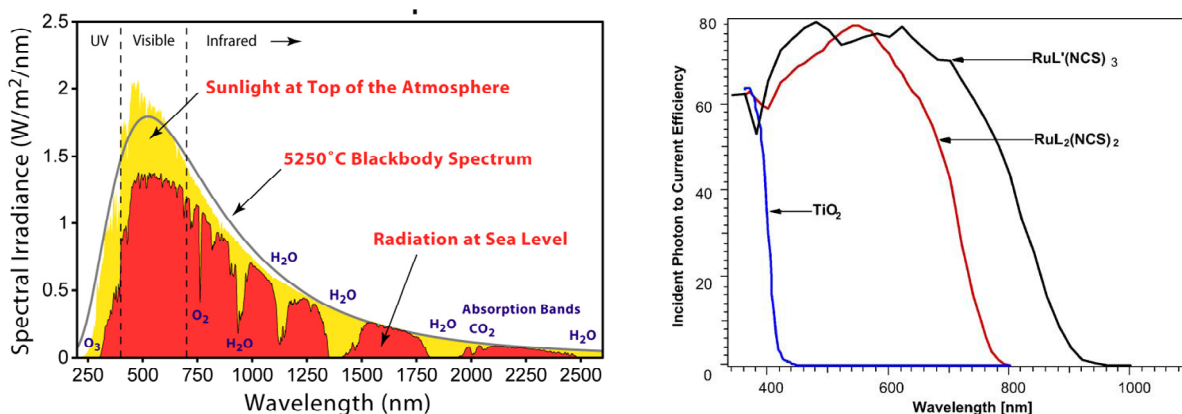


**Figure 1.6.** Left: The solar radiation spectrum, showing a peak intensity at  $\sim 500$  nm.<sup>11</sup> Right: The incident photon-to-current efficiencies (IPEC) for  $\text{TiO}_2$  and two  $\text{Ru}^{+2}(\text{bpy})_3$  derivatives.<sup>10</sup> More substantial overlap of the solar radiation spectrum is observed for the  $\text{Ru}^{+2}(\text{bpy})_3$  derivatives compared to  $\text{TiO}_2$ .

### 1.3.1.6. DNA hybrid materials

DNA hybrids are made by attaching the biopolymer DNA to a second material such as a polymer, an inorganic nanoparticle, or a small molecule. Over the last two decades, DNA hybrid materials have been utilized in various areas, including but not limited to: programmed self-assembly,<sup>12-17</sup> molecular computing,<sup>18-20</sup> templated synthesis,<sup>21-25</sup> and the development of new strategies for genetic detection.<sup>26-28</sup> Most relevant to the work described in this thesis, it has recently been shown that aggregates comprised of materials containing multiple DNA strands, such as DNA-functionalized comb polymers<sup>29</sup> and DNA-functionalized gold nanoparticles

(GNPs),<sup>30</sup> have notably sharpened melting profiles compared to unmodified DNA:DNA duplexes.

The enhanced melting properties of the aforementioned DNA hybrid materials have been attributed to the *cooperative* melting of the numerous DNA strands on each unit-structure,<sup>31</sup> and can be used to improve selectivity in DNA detection platforms. While the central core in each of these DNA hybrids varies, each feature closely spaced (25-40 Å) arrangements of multiple DNA strands stemming from a core and result in hybrid materials that have the native recognition properties of DNA in addition to enhanced hybridization selectivity made possible by multivalent interactions. Chapter 3 of this thesis expands on the importance of these cooperative melting transitions, that until recently have only been observed for large polymer-DNA<sup>29</sup> and GNP-DNA aggregates<sup>30</sup> linked through numerous DNA duplexes. It also describes the first observation of cooperative melting in discrete DNA-hybrid structures formed from small molecule-DNA hybrids possessing *only* three DNA strands around a rigid small-molecule core.

#### **1.4. Thesis overview**

The examples reviewed in sections 1.2 and 1.3 demonstrate the ubiquity of hybrid materials (both naturally occurring and artificial) and the tremendous potential of combining seemingly dissimilar materials into new hybrid materials with novel properties.

Chapter 2 consist of two sections, both describing materials synthesized via cross-linking pendant terthiophene side chains on a poly(norbornene) backbone. The first section illustrates the enhanced thermal-stability of chemically cross-linked poly(norbornene-terthiophene) powders and the improved surface smoothness of poly(norbornene-terthiophene) thin-films electrochemically cross-linked on indium tin-oxide (ITO)-coated glass electrodes. The inclusion

of the poly(norbornene) backbone has no negative effect on either the fluorescence or the conductivity of the poly(terthiophene). In the second section, the improved surface properties of the electrochemically cross-linked poly(norbornene-terthiophene) are exploited in the fabrication of multicomponent nano-scale rods synthesized by the electrochemical deposition of gold, silver, and cross-linked polymer into the pores of an anodized aluminum oxide template.

Chapter 3 is comprised of three sections, and focuses on the use of small molecule-DNA hybrids (SMDHs) to elucidate the parameters that lead to the enhanced melting properties observed for aggregates of polymer-DNA and gold nanoparticle-DNA (GNP-DNA) hybrids (*vide supra*). The first section describes the synthesis and melting properties of rigid small-molecule DNA hybrids (rSMDHs) where three DNA strands are attached to a rigid tris(phenylacetylene) core through benzyl phosphate bonds. In the second section, the synthesis of flexible SMDHs (fSMDHs) with a poly(ethylene glycol) spacer between two DNA strands is outlined, and the melting properties of their hybridized structures are evaluated. Section three details the progress towards modularly constructed rSMDHs with DNA strands linked to the small-molecule core via triazole linkages.

Combining our understanding of the signaling properties of the terthiophene materials used in chapter 2 and the recognition properties of the DNA hybrid materials used in chapter 3, the two sections of chapter 4 outline the development of a “loaded,” intrinsically amplified polymer nanoparticle (PNP)-based probe for DNA diagnostics. The first section describes the assembly of PNPs from amphiphilic block copolymers containing fluorescent terthiophene groups. The second section illustrates the DNA functionalization of these PNPs to create a PNP-

DNA hybrid material and its implementation into an intrinsically amplified DNA detection assay.

## Chapter 2

### Cross-Linked Films and Rods of Poly((2-terthiophenyl)norbornene)

Portions of this chapter appear in the following manuscript:

Stepp, B. R.; Nguyen, S. T. *Macromolecules* **2004**, *37*, 8222-8229.



## 2.1. Background

Since the groundbreaking discovery of electrically conducting organic polymers in 1977 by Heeger, MacDiarmid, and Shirakawa,<sup>1</sup> these materials have attracted considerable attention due to their potential applications in electronic devices.<sup>2</sup> The subsequent Nobel Prize in 2000 awarded to the three aforementioned pioneers enunciated the unequivocal importance of this class of materials.

Organic conducting polymers are attractive for device application in view of their light weight, their easy processability, and their ready tailorability. Exciting developments have been made in the application of conducting polymers to light-emitting diodes (PLEDS),<sup>3,4</sup> energy-storage devices,<sup>5</sup> photovoltaics,<sup>6</sup> and electrochromic materials for displays and smart windows.<sup>7</sup> Over the past three decades, numerous types of conducting polymers have been explored for such applications with conjugated heterocyclic polymers such as poly(pyrrole), poly(furan), poly(thiophene), and their derivatives, being an important sub-class.

### 2.1.1. Poly(thiophenes)

Extensive studies have been carried out on conducting polymers obtained from the oxidative polymerization of thiophenes,<sup>8</sup> bithiophenes,<sup>9</sup> and terthiophenes.<sup>10</sup> Recently, terthiophene polymers have been used successfully in the creation of white<sup>11</sup> and multicolor<sup>12</sup> PLED devices. It has also been shown that judicious placement of alkyl chains on the thiophene sub-units,<sup>13</sup> or bridging polymers with conducting crosslinks<sup>14</sup> allows for the tuning of polymer conductivity, processability, and local morphology.

However, a potential problem with the use of the “native,” unmodified, polymers of thiophene and its derivatives in thin-film applications is the low surface uniformity (or high

surface roughness) which can make device applications difficult due to poor interfacial contacts.<sup>15-17</sup> For example, in the preparation of poly(thiophene) thin-films by electrochemical polymerization, polymeric units precipitate onto an electrode surface as small islands.<sup>18</sup> The high surface roughness of these thin-films is thought to arise via an Ostwald ripening process; it is energetically more favorable for newly precipitated particles to join existing nuclei than form a new nucleation site, resulting in uneven three-dimensional growth (Figure 2.1).

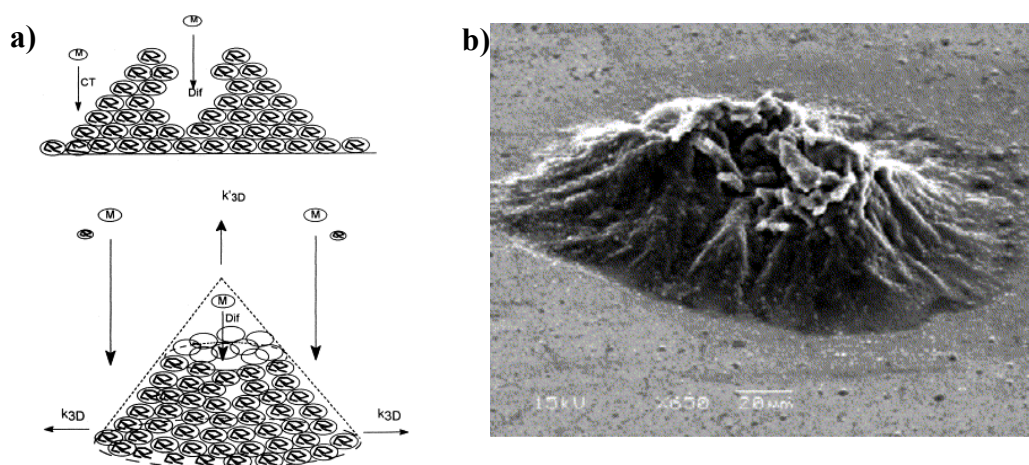


**Figure 2.1.** a) A three-dimensional growth model for poly(thiophene) proposing that it is kinetically favored that oligomeric monomer units (M) join a growing nucleus of poly(thiophene) as they precipitate from solution. b) An SEM image of a poly(thiophene) nucleus formed on an electrode surface.<sup>18</sup>

## 2.2. Enhanced properties of cross-linked poly((2-terthiophenyl)norbornene)

### 2.2.1. Introduction

Watson et al. previously reported the synthesis of norbornenyl-substituted thiophene monomers, which can be doubly polymerized via ring-opening metathesis polymerization followed by oxidative polymerization.<sup>19</sup> Because the second step can be carried out electrochemically, we hypothesize that such an oxidative polymerization of poly((2-terthiophenyl)norbornene) would undergo a film-growth mechanism different from that of native terthiophene, potentially leading to improved surface properties. The numerous terthiophenes on a single polymer backbone dictates that multiple groups will reach the surface at the same time, incurring more uniform two-dimensional growth (Figure 2.2). Additionally, the presence of the norbornene backbone should significantly improve the thermal stability of the resulting material compared to native poly(terthiophene).

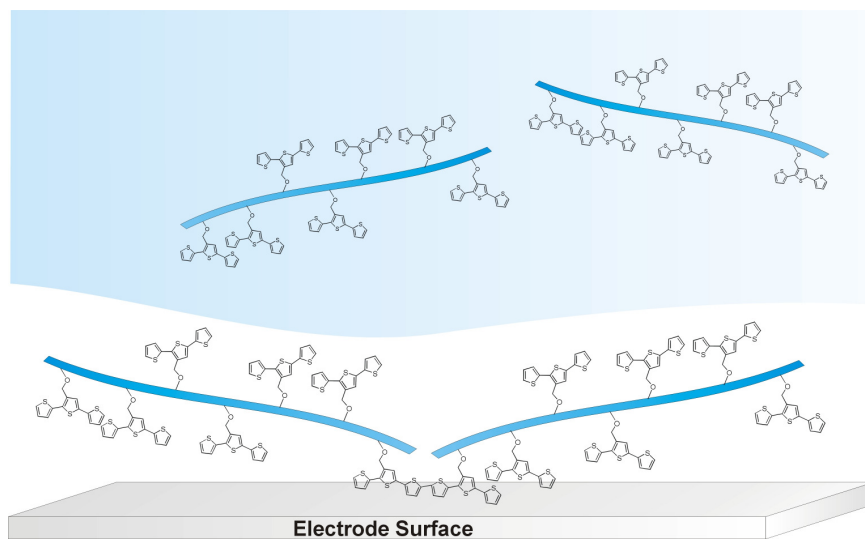
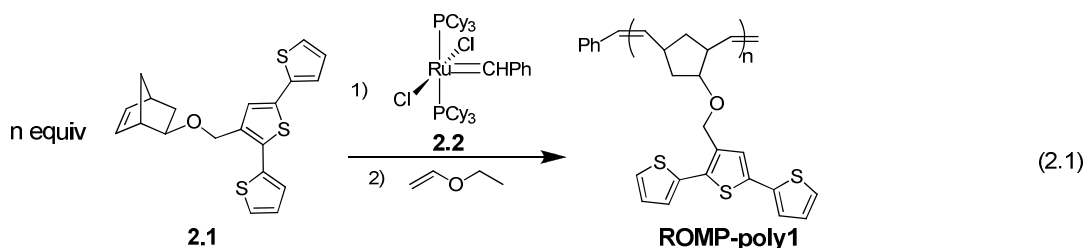


**Figure 2.2.** A proposed two-dimensional growth mechanism for films of cross-linked poly((2-terthiophenyl)norbornene): extended polymer chains bring multiple terthiophene groups to the surface over a larger area than that of native terthiophene, resulting in smoother films on the electrode surface.

In this section, the synthesis of ROMP polymers of 3'-(*exo*-5-Norbornene-2-oxy)methyl-2,2':5',2''-terthiophene (**2.1**) and the effects of chain length on the physical properties of the resulting ROMP polymers under a variety of cross-linking conditions are discussed.

## 2.2.2. Results and discussion

### 2.2.2.1. Ring-opening metathesis polymerizations of monomer **2.1**



ROMP reactions were carried out using catalyst **2.2** at monomer/catalyst ratios of 15, 20, 25, 30, 50, 100, and 200 (Eq 2.1). The resulting **ROMP-poly1** polymers are reasonably monodispersed (Table 2.2 in section 2.4.3) and the plot of  $M_n$  vs. monomer/catalyst ratio is linear (Figure 2.3), as would be expected for a living polymerization.<sup>20,21</sup>

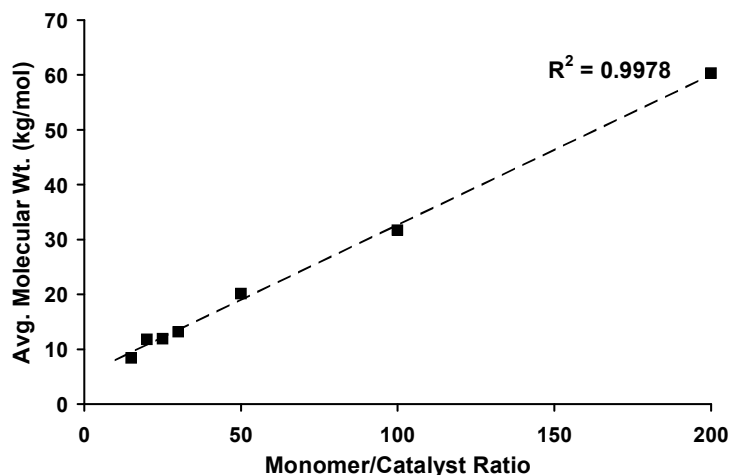


**Figure 2.3.** The number-average molecular weight ( $M_n$ ) for **ROMP-poly1** polymers plotted against the monomer-to-catalyst ratio.

### 2.2.2.2. Electrochemical and FeCl<sub>3</sub>-induced polymerization ROMP-poly1

Terthiophenes are known to undergo oxidative polymerization, either electrochemically<sup>22,23</sup> or in the presence of FeCl<sub>3</sub>,<sup>24-26</sup> to form poly(terthiophene). Hence, oxidative coupling of pendant terthiophene groups on pre-existing polymer chains such as **ROMP-poly1** will result in cross-linked polymers.

Solutions of either **ROMP-poly1** or terthiophene undergo electrochemical oxidation to form orange films on ITO-coated glass. Growth of film layers is evidenced by an increase in peak current as the electrode is cycled (Figure 2.4, a). Using this technique, 1- to 6-layer films were made from five different **ROMP-poly1** samples and terthiophene. Consistent with the slow diffusion of ions in and out of the film as it gets thicker, the absolute current increases and the oxidation ( $E_{ox}$ ) and reduction ( $E_{red}$ ) potentials shift to higher  $E_{ox}$  and lower  $E_{red}$  values as the number of scans increases. Further, electrochemically cycling a pre-made film of cross-linked **ROMP-poly1** at various scan rates leads to an increase in current and separation of  $E_{ox}$  and  $E_{red}$  peaks as the scan rate increases (Figure 2.4 b). These results exemplify the effects of slow ion diffusion, and are similar to those observed by Wrighton and coworkers for a derivatized gold electrode.<sup>27</sup>

Alternatively, FeCl<sub>3</sub>-induced oxidative polymerization led to dark insoluble powder samples of cross-linked **ROMP-poly1** and poly(terthiophene) after Soxhlet extraction of the spent oxidant with methanol. To determine the thermal stability of the cross-linked **ROMP-poly1** compared to native poly(terthiophene), these powder samples were subsequently analyzed by thermal gravimetric analysis (TGA) (Section 2.2.2.5).

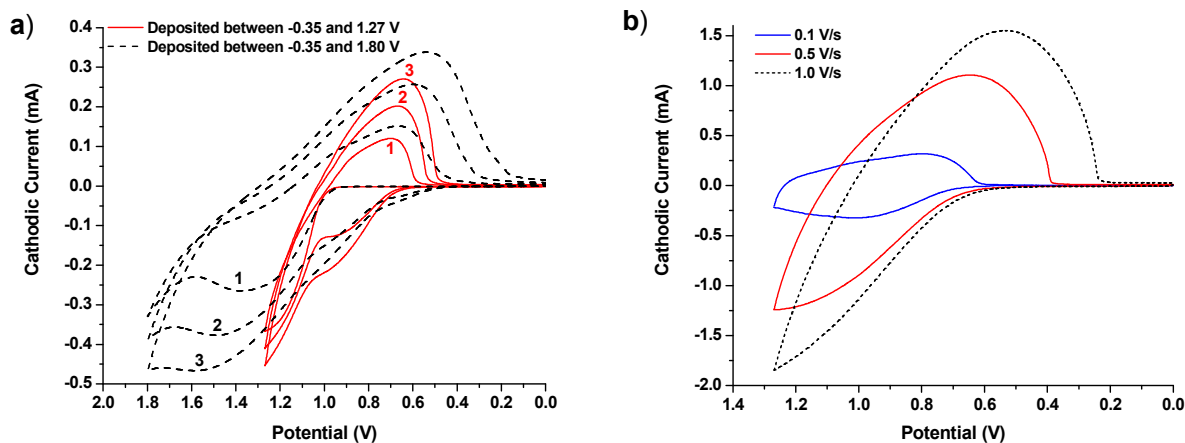


**Figure 2.4.** a) Films of **ROMP-poly1** are electrochemically cross-linked on ITO-coated glass by repeated scanning from  $-0.35$  to  $1.27$  V (red traces) and  $-0.35$  to  $1.80$  V (black traces). Peak current increases and peak potential shifts as subsequent layers (1-3) are deposited. b) A 3-layer film of cross-linked **ROMP-poly1** (deposited on ITO-coated glass) is electrochemically cycled at  $0.1$  V/s,  $0.5$  V/s, and  $1$  V/s in  $[0.1$  M TBAPF<sub>6</sub>/CH<sub>2</sub>Cl<sub>2</sub>]. Increasing the rate attenuates ion mobility in and out of the film, thereby increases peak-to-peak separation.<sup>27</sup>

### 2.2.2.3. Visual microscopy of cross-linked films

Visually, the films of cross-linked **ROMP-poly1** were more uniform than films of poly(terthiophene). Films formed by scanning from  $-0.35$  to  $1.80$  V were opaque, while those formed by scanning up to a maximum voltage of  $1.27$  V were transparent and had better optical and thermal properties than those formed at  $1.80$  V (Figure 2.5). These observations are consistent with formation of the irreversible over-oxidation product described by Koßmehl.<sup>28</sup> Over-oxidation results in an insulating film,<sup>29</sup> indicated by a gradual reduction in peak current after three cycles from  $-0.35$  to  $1.80$  V (*vide infra* section 2.2.2.6).

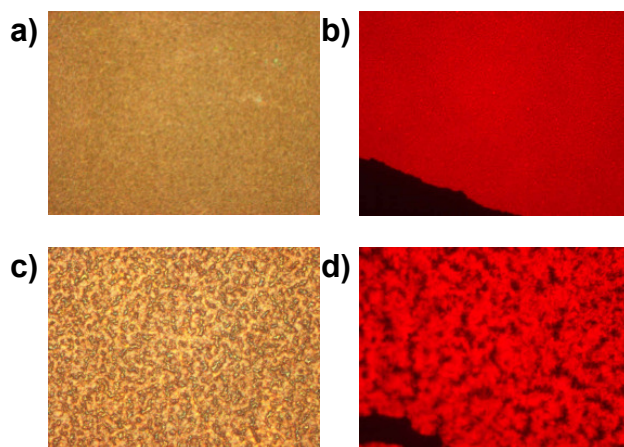


**Figure 2.5.** Optical (left column, 50x magnification, differential interference contrast (DIC) mode) and fluorescence (right column, excitation 533-587 nm and emission 608-668 nm) microscopic images show that films of **ROMP-poly1** generated between 0.0 and 1.27 V (a and b) are more uniform than those generated between 0.0 and 1.80 V (c and d).

#### 2.2.2.4. *In-situ* conductivity measurements of cross-linked **ROMP-poly1** and poly(terthiophene)

Films of cross-linked **ROMP-poly1** and poly(terthiophene) were deposited over the surface of gold IDA electrodes and the *in-situ* conductivity of each polymer film was then measured as a function of doping potentials (Figure 2.6).<sup>30-33</sup> Films derived from cross-linked 50-mer and 25-mer samples of **ROMP-poly1** both show appreciable conductivity, albeit lower (about 2.5x for the cross-linked 50-mer **ROMP-poly1**) than that obtained for native poly(terthiophene) films prepared in the same manner. This is likely due to a loss of rotational freedom caused by the presence of the poly(norbornene) backbone in **ROMP-poly1**.<sup>14</sup> Conductivity may potentially be enhanced if longer oligothiophene units are used in place of the terthiophene substituent on monomer **2.1**. For example, penta- or heptathiophene should improve conductivity by increasing the conjugation length of the poly(terthiophene) crosslinks. We note that the turn-on voltages for poly(terthiophene) and cross-linked **ROMP-poly1** are quite

different. While the former is considerably more conductive, it has a broad turn-on voltage region that spans from 0.4 V to greater than 1.0 V. On the other hand, cross-linked **ROMP-poly1** demonstrates a sharper and more distinct turn-on voltage range of 0.7-0.9 V, presumably due to a narrower distribution of conjugation segments. This well-defined transition between off and on conductive states is a potential advantage for our cross-linked ROMP polymer in switching applications.

Interestingly, attempts to measure the *in-situ* conductivity of cross-linked 100-mer and 200-mer samples of **ROMP-poly1** were unsuccessful due to our inability to grow continuous films across the two bands of the IDA electrode in several solvents and solvent mixtures. For these polymers, films were observed to only grow directly on the surface of the Au fingers of the IDA and did not spread across the two bands of electrodes, as seen for the lower molecular weight polymers (*vide supra*). This is probably due to a reduced solvation of the longer polymers, which results in more intra-chain cross-linking and less radial growth.

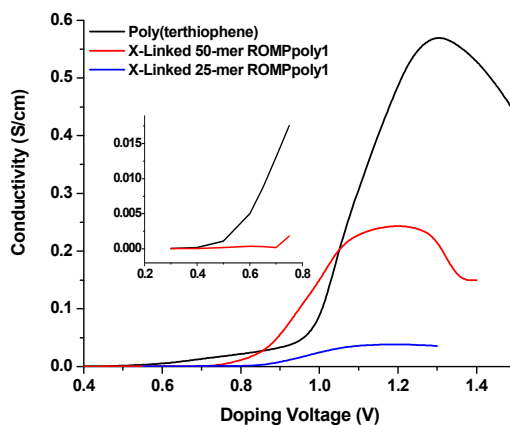


**Figure 2.6.** *In-situ* conductivity plots of poly(terthiophene) and cross-linked **ROMP-poly1** versus doping potential. The inset plots show the difference in turn-on voltages for poly(terthiophene) and cross-linked **ROMP-poly1**. The drops in conductivity after 1.25 V are a consequence of over-oxidation.



### 2.2.2.5. Thermal gravimetric analyses of cross-linked ROMP-poly1 and poly(terthiophene)

To test the effects of chain length and cross-linking methods on the thermal stability of cross-linked **ROMP-poly1**, TGA scans were performed on samples of various chain lengths of the parent **ROMP-poly1** and on samples from both FeCl<sub>3</sub>-induced and electrochemical polymerization of cross-linked **ROMP-poly1** and poly(terthiophene) under N<sub>2</sub> (Figure 2.7). The thermal stability of both the parent polymers and the corresponding cross-linked ROMP polymers showed no appreciable dependence on the length of the former. Cross-linked **ROMP-poly1** exhibited an increase in thermal stability, and displayed temperature profiles that are much more stable than those of the parent ROMP polymers and only slightly inferior to those of poly(terthiophene).

For accurate measurements of thermal stability of the samples prepared via FeCl<sub>3</sub>-induced polymerization, it is critical to completely dry all samples following Soxhlet extraction. Incomplete drying can lead to a significant reduction of thermal stability (Figure 2.7 b). This apparent reduced thermal stability can be attributed to “incomplete curing”: as the temperature rises, detrimental reaction between the trapped protic solvent and the polymer can occur. The potential reducing ability of protic solvents has been noted for oxidized polyterthiophene.<sup>34</sup> Exposure of a “cured” sample, which had been previously dried under high vacuum for 12 h, to methanol and running TGA after short (1.5 h) and long (12 h) drying times supported this hypothesis (Figure 2.7 c). After 1.5 h of drying under vacuum, the methanol-exposed sample shows a significant decrease in stability compared to the 12-h dried sample; however, the thermal stability does not decrease to the extent of the initial incompletely dried sample (Figure

2.7 b). On the other hand, the methanol-exposed sample that went through the long drying time shows the same stability as the parent sample.

The thermal stability of electrochemically cross-linked films of **ROMP-poly1** and poly(terthiophene) deposited on Au/Si substrates was also tested by TGA (Figure 2.7 d).

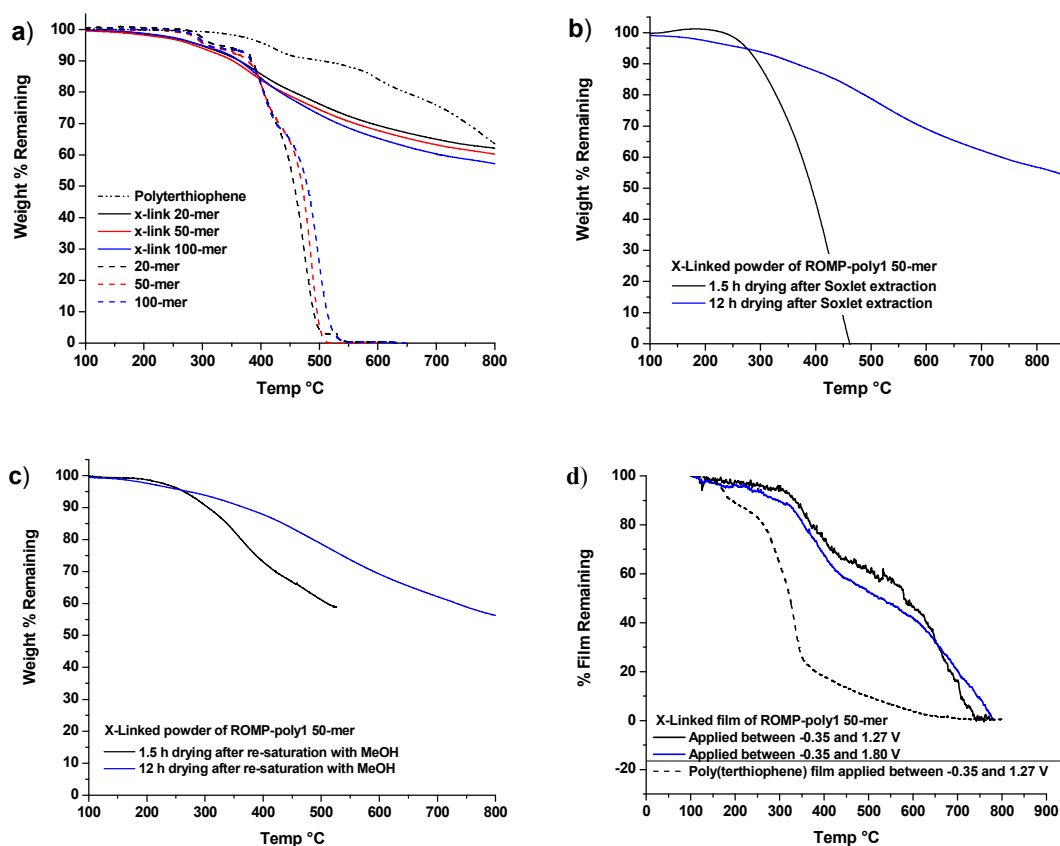


**Figure 2.7.** (a) TGA curves for powders of poly(terthiophene) prepared by  $\text{FeCl}_3$ -induced polymerization, three **ROMP-poly1** samples of different chain-lengths (monomer/catalyst ratio of 20, 50, and 100), and the corresponding cross-linked polymers prepared by  $\text{FeCl}_3$ -induced polymerization. (b) TGA results illustrating the effect of incomplete drying for a powder sample of cross-linked 50-mer **ROMP-poly1** prepared by  $\text{FeCl}_3$ -induced polymerization. (c) TGA curves illustrating the effect of re-exposing a powder sample of cross-linked 50-mer **ROMP-poly1** prepared by  $\text{FeCl}_3$ -induced polymerization to MeOH followed by drying over different periods of time. (d) TGA results for 50-layer films of electrochemically cross-linked 50-mer **ROMP-poly1** and poly(terthiophene) on Au/Si substrates.

Compared to the powder samples of FeCl<sub>3</sub>-induced cross-linked polymers, the film samples are not as stable. However, cross-linked films of **ROMP-poly1** possesses higher overall stability compared to films of poly(terthiophene) prepared in the same way, which can be a potential advantage in device applications. Thermal stability was moderately improved for films deposited between -0.35 and 1.27 V compared to those deposited between -0.35 and 1.80 V.

#### **2.2.2.6. Electrochromic behavior of cross-linked ROMP-poly1 and poly(terthiophene)**

Similar to observations made for other thiophene-based and terthiophene-modified polymers,<sup>35-37</sup> films of electrochemically cross-linked **ROMP-poly1** and poly(terthiophene) displayed electrochromic properties when oxidatively doped (Figure 2.8) in perchlorate electrolyte. The color change was visibly identical for both polymer films; however, scans between -0.35 and 1.80 V were irreversible while those between -0.35 and 1.27 V were reversible (Figure 2.9). For the former potential range, the color change for films become less distinguishable and became noticeably darker after each cycle. This behavior can also be observed in PF<sub>6</sub><sup>-</sup>-containing electrolytes.

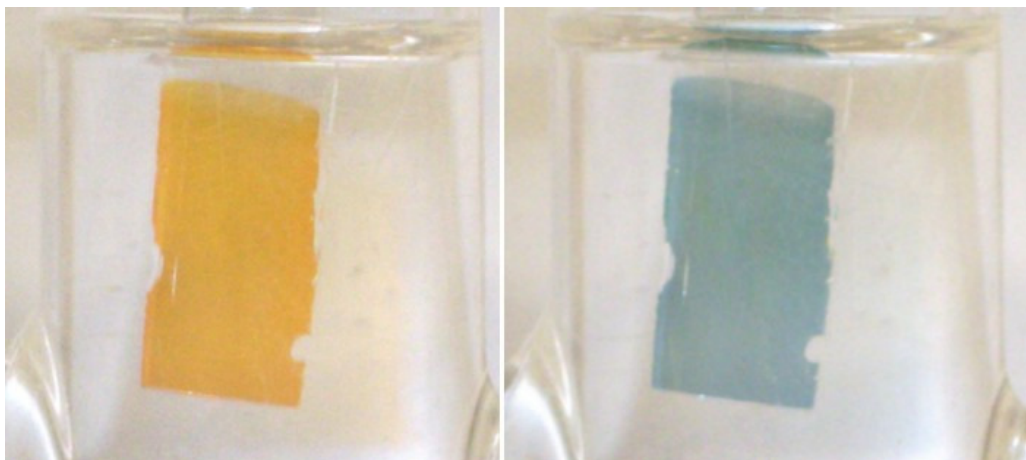


**Figure 2.8.** A three-layer film of electrochemically cross-linked 20-mer **ROMP-poly1** changes from orange (left) to dark blue (right) in a perchlorate-containing electrolyte as the cell voltage is increased from  $-0.35$  to  $1.27$  V. This dopant-induced color change is reversible over 20 or more cycles.

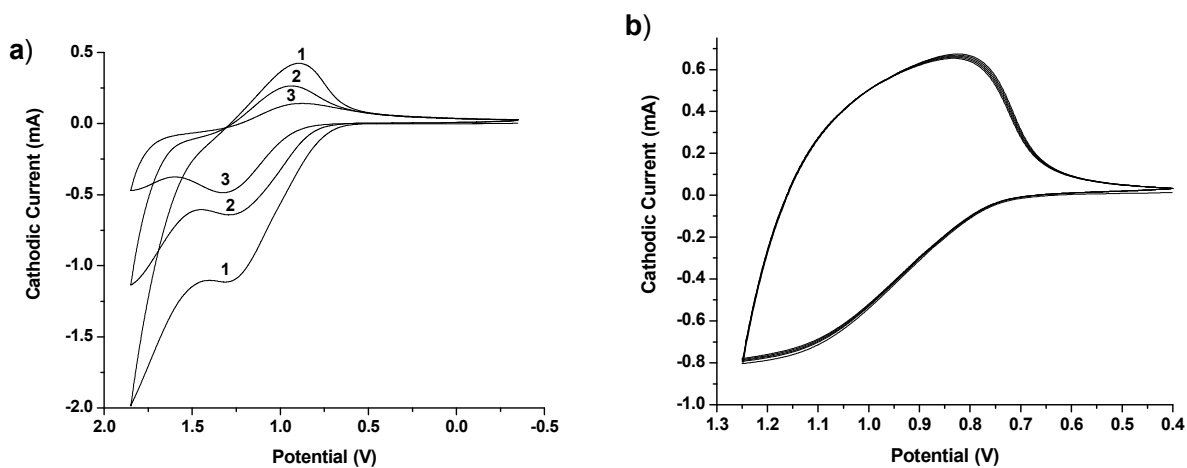


**Figure 2.9.** Current-voltage plots of two separate 3-layer films comprised of electrochemically cross-linked 20-mer **ROMP-poly1** immersed in methylene chloride containing  $0.1$  M tetrabutylammonium perchlorate. (a) Due to overoxidation, peak current decreases with each subsequent cycle when one film is scanned between  $-0.35$  and  $1.80$  V. (b) The I-V behavior remains constant over 5 cycles when another identical film is scanned between  $-0.35$  and  $1.27$  V.

### 2.2.2.7. Optical properties of cross-linked ROMP-poly1.

The use of fluorescence microscopy facilitated the macroscopic observation of fluorescence from electrochemically cross-linked 20-mer **ROMP-poly1** and poly(terthiophene) films on ITO-coated glass. Films were excited by filtered light at various wavelengths, causing an emission, which was also filtered before viewing (Figure 2.10). Additionally, the emission spectra of films that have been deposited on ITO electrodes were collected upon irradiation at three different pre-determined absorbance maxima (obtained from UV-vis measurements) (Figure 2.11).

In general, both macroscopic fluorescence and emission from **ROMP-poly1** films were chain-length independent and are very similar to those of poly(terthiophene). However, **ROMP-poly1** films were consistently of a better quality with fewer defects, in accordance with AFM studies (section 2.2.2.8).

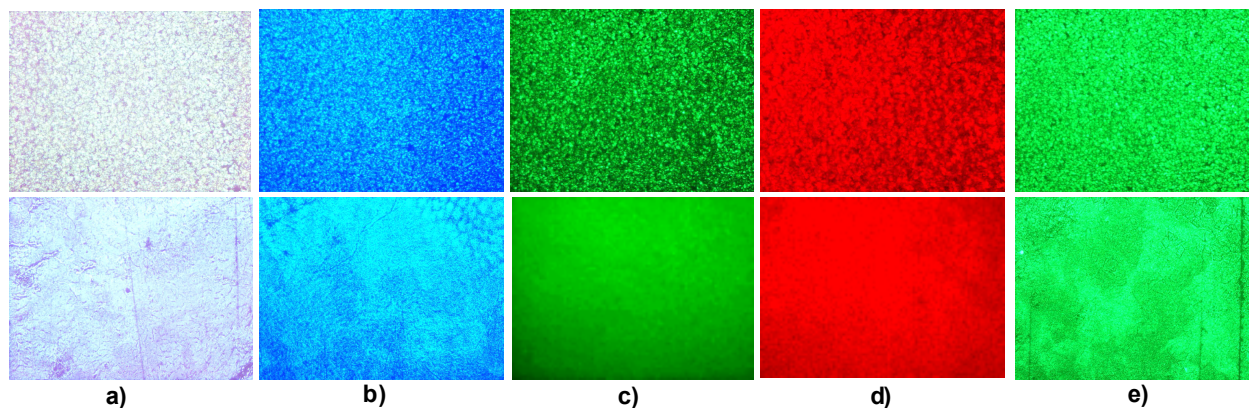


**Figure 2.10.** Digital images of 3-layer films of poly(terthiophene) (top row) and **ROMP-poly1** (bottom row) taken from fluorescence microscopy experiments. a) Ex. 340-380 nm, Em. No Filter. b) Ex. 340-380 nm, Em. 435-485 nm. c) Ex. 460-500 nm, Em. 510-560 nm. d) Ex. 533-587 nm, Em. 608-668 nm. e) Ex. 340-380 nm, Em. 510-560 nm.

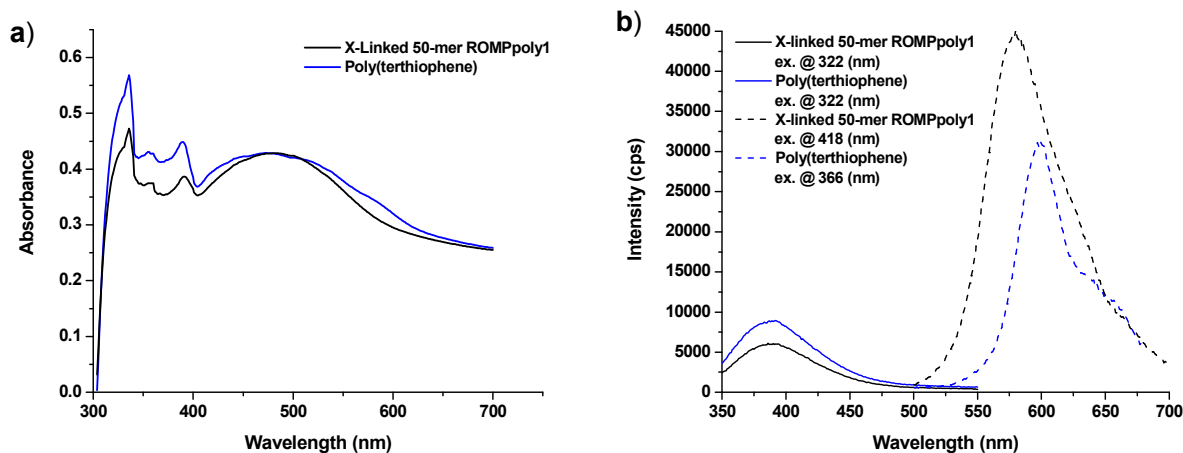


**Figure 2.11.** The UV-vis (a) and emission (b) spectra for 3-layer films of poly(terthiophene) and **ROMP-poly1** that have been deposited on an ITO electrode were very similar. Fluorescence spectra were taken using excitation wavelengths of 322 nm, 366 nm, and 418 nm.

#### 2.2.2.8. Surface studies of cross-linked **ROMP-poly1** and poly(terthiophene) using tapping-mode AFM

AFM topographic images demonstrate the smoother texture of films cross-linked **ROMP-poly1** applied between  $-0.35$  and  $1.27$  V compared to those deposited between  $-0.35$  and  $1.80$  V and those of poly(terthiophene) (Figure 2.12). The latter are remarkably similar to those of the SEM images of poly(thiophene) taken by del Valle and co-workers.<sup>18</sup> Phase images of AFM scans suggest that cross-linked films of **ROMP-poly1** are amorphous solids with no obvious phase segregation. Based on root-mean-square (rms) of roughness calculations, all films of cross-linked ROMP-polymers (15-mer, 30-mer, and 50-mer) deposited at lower potentials ( $-0.35$  to  $1.27$  V) were much smoother ( $<10$ -nm rms) than those applied at higher potentials ( $-0.35$  to  $1.80$  V) or films of poly(terthiophene) ( $>100$ -nm rms). The better planarity of the cross-linked **ROMP-poly1** films is likely due to a 2-dimensional layer-by-layer initiation and growth mechanism as described by Alberty and co-workers for films of poly(thiophene-3-acetic acid),<sup>38</sup>

while the less ordered poly(terthiophene) films are consistent with the three-dimensional growth mechanism described by del Valle.<sup>18,39</sup>

**Table 2.1.** Root-mean-square (rms) of roughness values of cross-linked **ROMP-poly1** and poly(terthiophene) films on ITO-coated glass. Each film is the result of three deposition scans.

Polymer	rms roughness (nm)	
	Deposited from −0.35 to 1.27 V	Deposited from −0.35 to 1.80 V
Polyterthiophene	117.9	531.0
Cross-linked 15-mer of <b>ROMP-poly1</b>	7.2	199.7
Cross-linked 30-mer of <b>ROMP-poly1</b>	5.1	340.8
Cross-linked 50-mer of <b>ROMP-poly1</b>	5.8	127.8

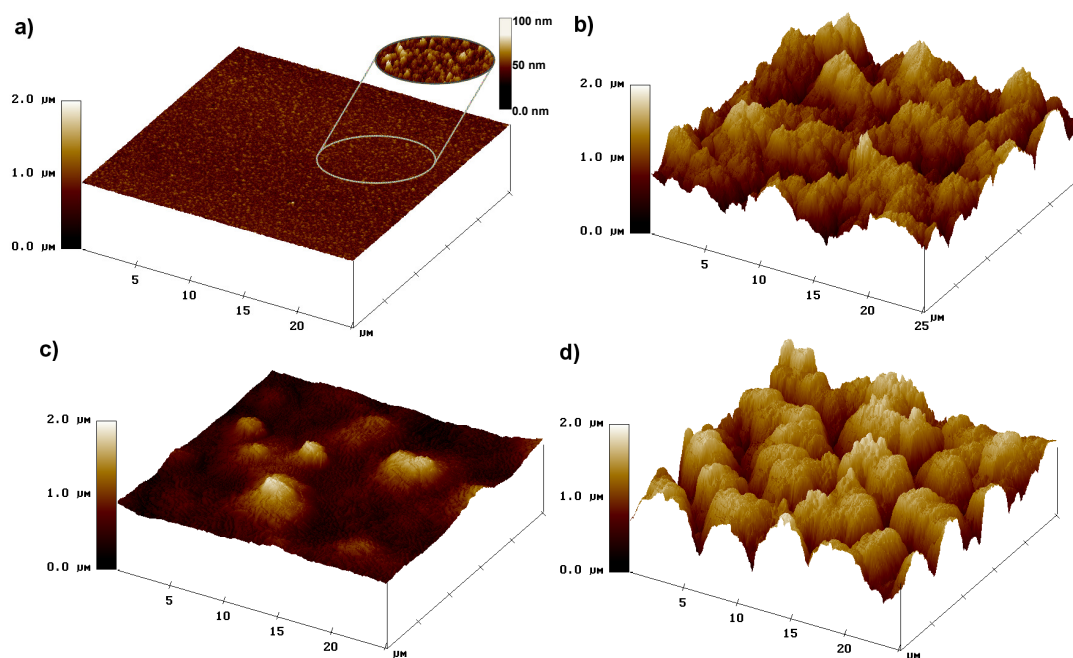


**Figure 2.12.** AFM images of electrochemically prepared: (a) cross-linked 30-mer **ROMP-poly1** film deposited between −0.35 and 1.27 V (inset with reduced z-range to show detail), (b) cross-linked 30-mer **ROMP-poly1** film deposited between −0.35 and 1.80 V, (c) poly(terthiophene) film deposited between −0.35 and 1.27 V, and (d) poly(terthiophene) film deposited between −0.35 and 1.80 V. Each film is the result of three deposition scans.

### 2.2.3. Conclusions

ROMP polymerization of **2.1** at monomer/catalyst ratios of 15, 20, 25, 30, 50, 100, and 200 proceeded well and resulted in near monodispersed polymers (PDI < 1.30). Oxidative polymerization of the resulting **ROMP-poly1**, by either FeCl<sub>3</sub> or electrochemistry, yielded dark powders or orange films of cross-linked **ROMP-poly1**, respectively.

TGA experiments under N<sub>2</sub> atmosphere showed that bulk samples of the FeCl<sub>3</sub>-induced cross-linked ROMP-polymers are considerably more heat-resistant than the non-cross-linked ROMP-polymers, and that increasing the chain-length of polymer backbone beyond 20 monomer units has little effect on the stability of the cross-linked polymer. Of note is the high stability of electrochemically deposited films of cross-linked **ROMP poly1** compared to poly(terthiophene) films prepared in the same manner.

The electrochemically cross-linked films of **ROMP-poly1** deposited between -0.35 and 1.27 V are transparent and of better quality than those deposited between -0.35 and 1.80 V which suffer from overoxidation. Films of cross-linked **ROMP-poly1** are smoother and more uniform than films of poly(terthiophene), as evidenced by optical and atomic force microscopy. *In-situ* conductivity measurements demonstrated dopant-induced conductivity, with improved on/off characteristics for cross-linked **ROMP poly1** films in comparison to poly(terthiophene) films. Similar to films of other poly(thiophene)-based materials, doping the cross-linked films with ClO<sub>4</sub><sup>-</sup> revealed a reversible electrochromic color change from orange to blue. The better switching characteristics, along with improved film uniformity and thermal stability of the materials obtained by cross-linking pendant terthiophene groups on a poly((2-terthiophenyl)norbornene) backbone, make these materials good leads for device fabrication and



this is investigated further in section 3.1. Additionally, the fluorescence properties of **ROMP-poly1** and cross-linked films of **ROMP-poly1** make these materials of interest for polymer based probes for biodiagnostic applications (chapter 4).

## **2.3. Synthesis of poly(thiophene)-derived metal-polymer nanorods using porous anodized aluminum oxide (AAO) templates**

### **2.3.1. Introduction**

Given their unique size-dependent properties, nanoscale materials are an active area of research in numerous areas of science and technology. In the medical fields, these materials offer the promise of improved biodiagnostics and drug-delivery vehicles,<sup>40</sup> while the electronics industry hopes that they will make available more efficient photovoltaics, superior light emitting diodes (LEDs), and better computing platforms.<sup>41,42</sup>

In electronics, where the drive to make devices that are faster and more powerful without increase the size means that individual components must do more in a smaller space and requires the development of higher precision fabrication platforms. Numerous methods for the fabrication of devices based on nanoscale materials have been developed, ranging from lithographic techniques to chemical processes,<sup>43</sup> however, integration of these nanoscale materials into macroscopic devices remains an immense challenge. Incorporation into a circuit would be facilitated by including attachment sites on the discrete nanoscale device. Multilayer nanoscale rods comprising conjugated polymers and metals could be an interesting solution to this problem, with the polymer section providing the electronic property of choice and the metal layers acting as contact points.

#### **2.3.1.1. Templating nanoscale rods with anodized aluminum oxide (AAO) membranes**

Martin and coworkers have found that uniform nanoscale rods can be synthesized by electroplating coinage metals into the pores of anodized aluminum oxide (AAO) membranes.<sup>44</sup> Using these methods, the synthesis of alternating Au/Ag metallic barcodes has also been

demonstrated.<sup>45</sup> Similar nanoscale rods have shown promise in organic light-emitting devices (OLEDs),<sup>46</sup> photovoltaics,<sup>47</sup> and detection schemes.<sup>48</sup>

Recently, Mirkin and coworkers demonstrated that gold-poly(pyrrole) rods could be synthesized from the electrochemical polymerization of poly(pyrrole) into the AAO templates and that these rods self-assemble into interesting structures that have diode-like properties.<sup>49,50</sup> These multicomponent rods are especially interesting as nanoscale electronic devices because the gold endcaps can function as either electric interconnects or sites for further functionalization.

Compared to thin-films of poly(pyrroles), the switching behavior from doped to undoped, is sharper, faster, and more reversible for thin-film of poly(thiophenes),<sup>2</sup> making poly(thiophenes)-containing nanorods an attractive extension to the poly(pyrrole) studies; however, the available literature for similarly synthesized poly(thiophenes) shows rods that are not uniform.<sup>51</sup> While this result is not surprising given the 3-dimensional growth of native poly(thiophenes) (vide supra, Section 2.1.2), smooth layer-to-layer contact is an especially important attribute to nanoscale devices. Based on the results from section 2.2, we speculate that rods containing layers of cross-linked **ROMP-poly1** should be significantly more uniform and make better connection to adjacent layers.

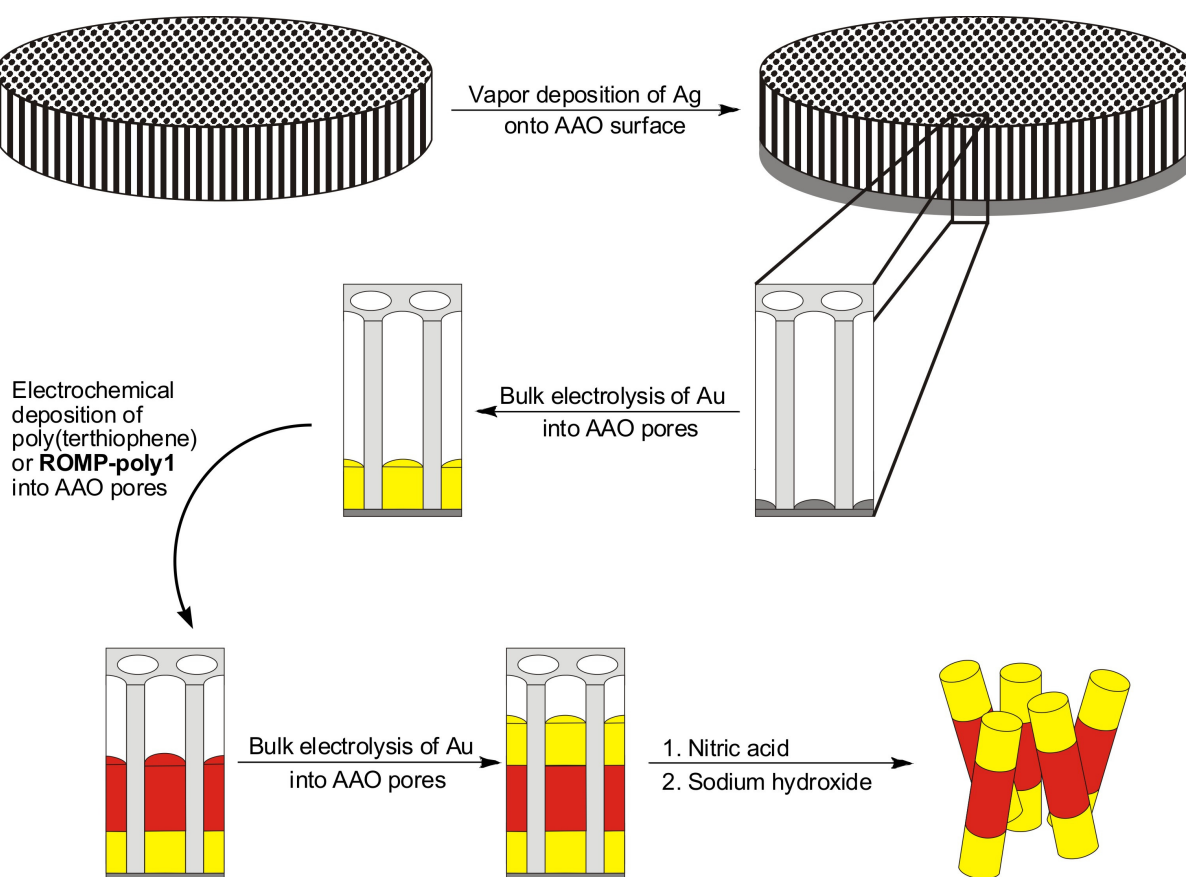
## **2.3.2. Results and discussion**

### **2.3.2.1. Synthesis of Au-polymer-Au rods**

Multicomponent Au-polymer-Au rods of gold and either poly(terthiophene) or cross-linked poly((2-terthiophenyl)norbornene) were synthesized in the pores of a silver-coated (AAO) membranes by alternately electrodepositing gold and oxidatively polymerizing terthiophene groups (Scheme 2.1). The diameter of rods fabricated in this manner is controlled by the pore

size of the AAO disks, nominally 200-nm diameter, while rod length is controlled by the total amount of charge deposited. Upon separation from the AAO membranes, these rods aggregate into bundles and sheets that can be broken up into individual rods with surfactants, allowing for direct visualization.

**Scheme 2.1.** Synthesis of Au-Polymer-Au rods comprising either poly(thiophene) or cross-linked **ROMP-poly1** using an AAO template.



### 2.3.2.2. SEM characterization of Au-polymer-Au rods

After separation from the AAO membrane, rods were characterized by scanning electron microscopy (SEM) to determine morphology and structural integrity. As expected, rods containing poly(terthiophene) are very rough and disconnected (Figure 2.13, A-C). On the other

hand, the rods comprised of cross-linked poly((2-terthiophenyl)norbornene) are smooth and continuous, suggesting a more controlled polymerization process (Figure 2.13, D-F).

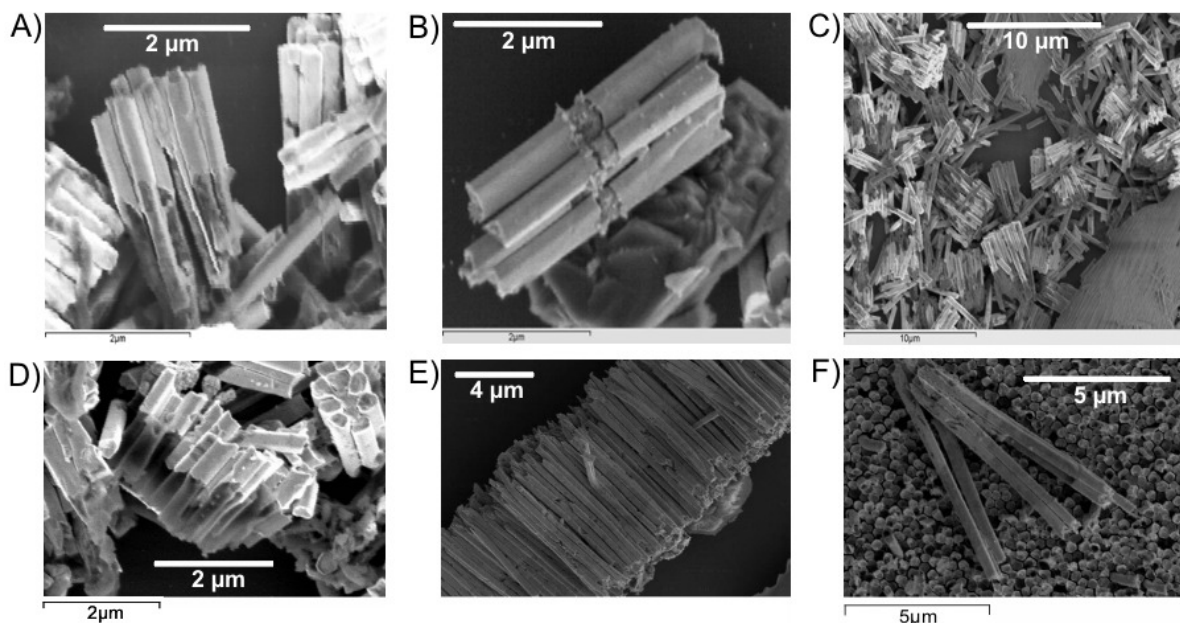


**Figure 2.13.** SEM images of: A-C) Rods containing poly(thiophene) showing disjunct junctions which are not well-attached to the gold. D-F) Rods containing cross-linked **ROMP-poly1** are more continuous and show very little breakage between the polymer and the gold segments.

### 2.3.2.3. Optical and fluorescence microscopy of Au-polymer-Au rods

As mentioned above (Section 2.3.2.1), multicomponent Au-polymer-Au rods typically aggregate into bundles and sheets following AAO template removal. Static fluorescence microscopy studies (Figure 2.14, top right) show that the fluorescence from the side of the rods is intensely red and similar to that of cross-linked polymer films (Section 2.2.2.7). Interestingly, fluorescence from the top of a sheet, inline with the rod axis, is localized and intermittent (Figure 2.14, bottom right). Time-lapse images (Figures 2.15 and 2.16) demonstrate that the “blinking” fluorescence arises from numerous sites on the sheet, and appears to “skip” from one site to the next.

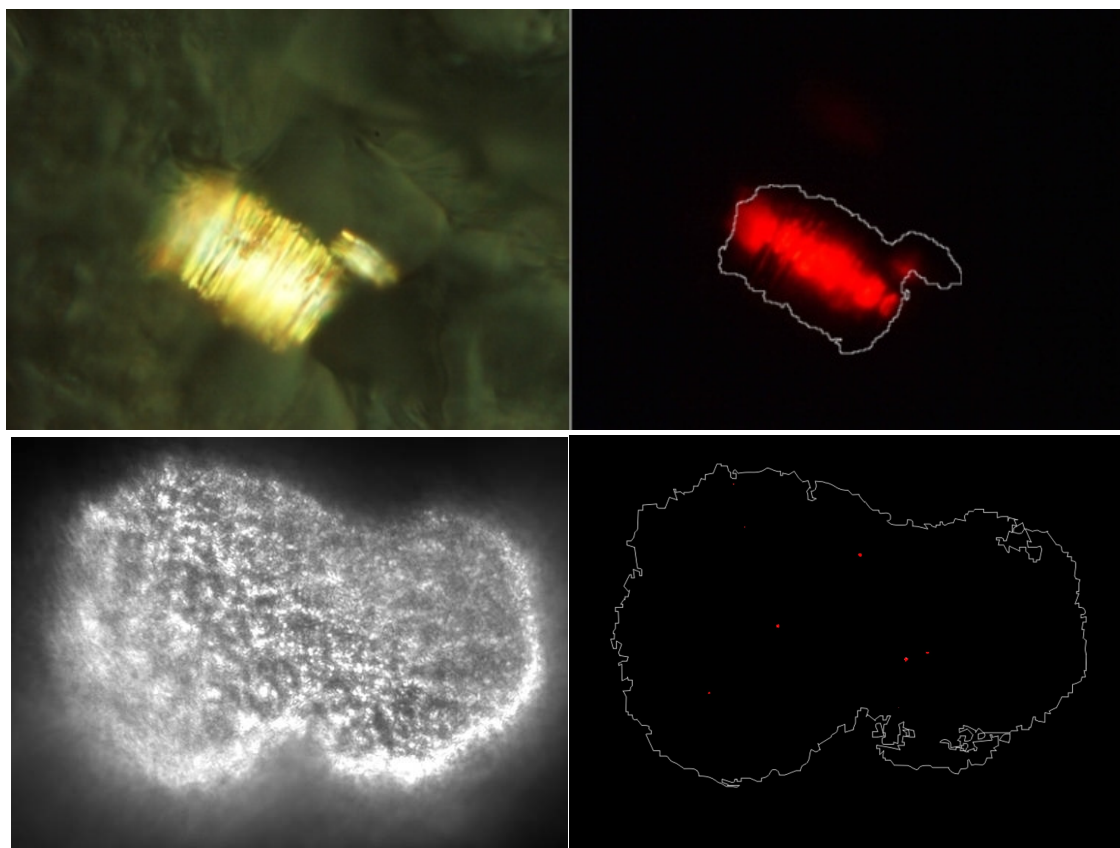


**Figure 2.14.** Optical (left column) and fluorescence (right column) microscopy images taken from the side of a small bundle of rods (top row) and from the top of a large sheet (bottom row). As a visual guide, the bundles of rods are outlined in the fluorescence microscopy images.

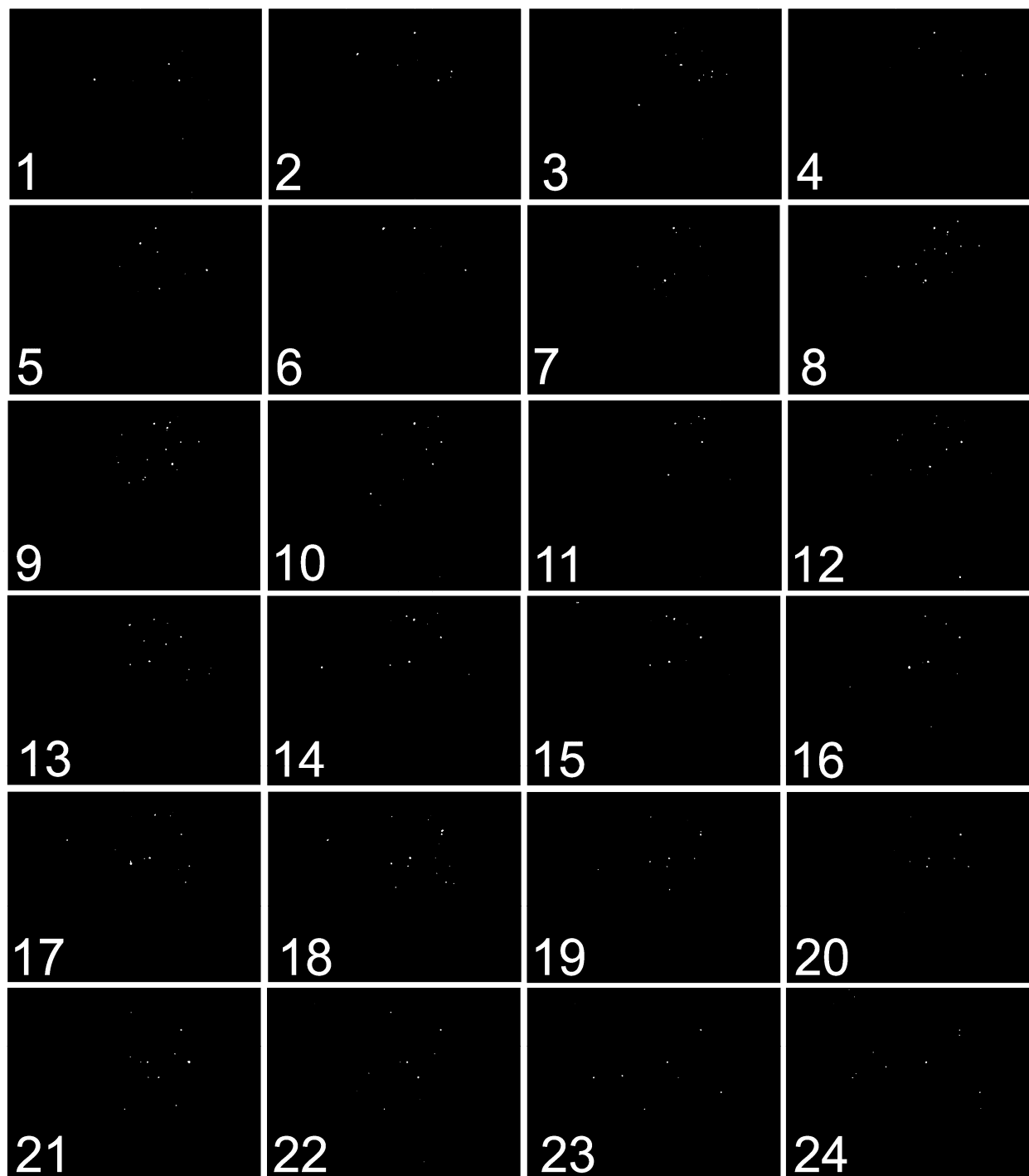


**Figure 2.15.** Black-and-white time-lapse fluorescence microscopy images taken from the top of a large sheet of bundled rods (5 frames per second), demonstrating the observed fluorescence “blinking.”

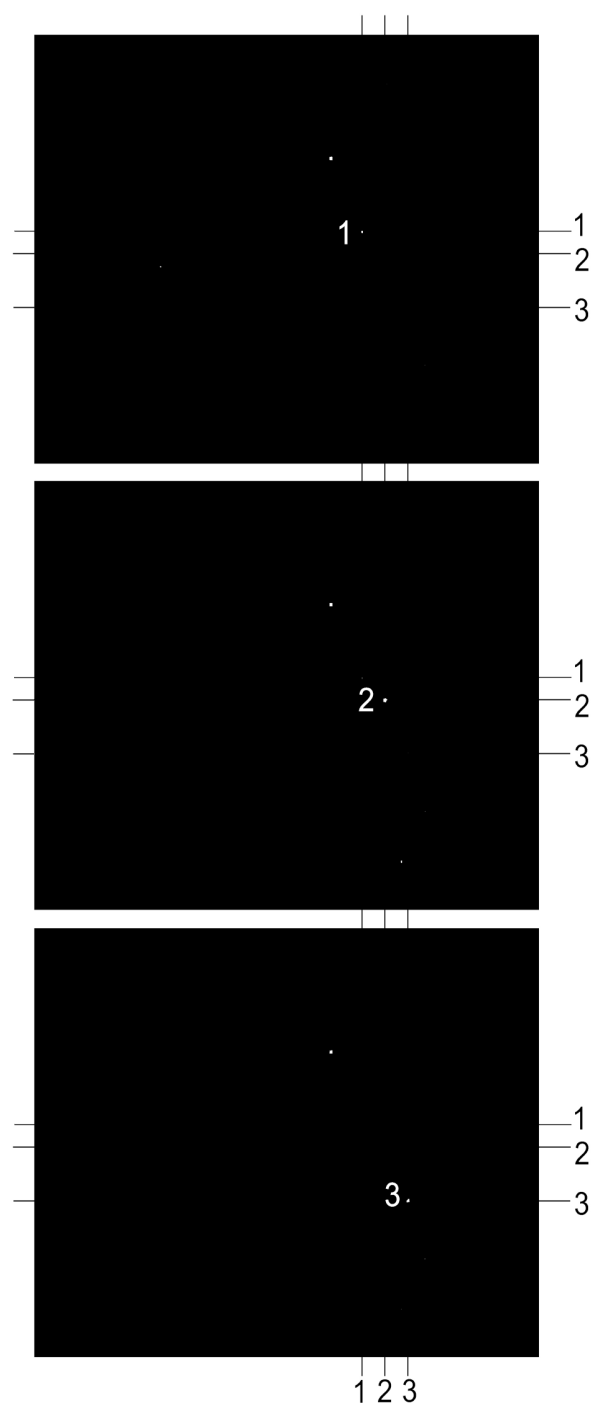


**Figure 2.16.** Three continuous time-lapse fluorescence microscopy images taken from the top of a large sheet of Au-polymer-Au rods (5 frames per second), demonstrating the observed fluorescence “skipping” from site 1 to 2 and from site 2 to 3. Lines at the edge of the images mark each fluorescent site.



Similar blinking behavior is well-known for semiconductor nanocrystals,<sup>52,53</sup> such as cadmium selenide (CdSe<sub>2</sub>) nanoparticles, and has also been observed for single molecules on a gold nanoparticle surface.<sup>54</sup> While more detailed studies, such as single-rod fluorescence and time-resolved emission, are required to thoroughly explain the excitation/emission mechanism in our Au-polymer-Au rods, we suggest an explanation based on previous studies concerning the interaction of fluorophores with bulk gold and gold nanoparticles. Gold is known to quench fluorescence by means of nonradiative energy transfer from the excited molecules to the Fermi level of the gold,<sup>55</sup> and blinking can arise by either dissipative relaxation processes of the gold plasmons or by charge back-transfer.<sup>54</sup> The observed “skipping” in aggregates of our Au-polymer-Au rods can be explained by a nanolens described by Stockman and coworkers,<sup>56</sup> where optically excited nanoparticles transfer surface plasmon resonance over several particles to create a “hottest spot” where the local fields are enhanced by orders of magnitude. When combined with the quenching caused by the gold caps, this nanolens effect could lead to skipping as one site is quenched and a nearby area is populated.

### 2.3.3. Conclusion

As evidenced by SEM imaging, multicomponent rods consisting of gold caps and a cross-linked **ROMP-poly1** core form better junctions than those containing a poly(terthiophene) core, making them robust and more suitable for further manipulation. Fluorescence emission from the middle of the rods is the intensely red, as expected for **ROMP-poly1** (Section 4.2), while “blinking” is observed from the top of rod aggregates. Elucidation and control of this “blinking” mechanism could lead to new nanoscale signaling platforms.

## 2.4. Experimental

### 2.4.1. General considerations and instrumentation

$^1\text{H}$ -NMR spectra were recorded on a Varian Mercury 400 FT-NMR spectrometer ( $^1\text{H}$  400.178 MHz). GC-MS experiments were recorded on a Hewlett-Packard HP 6980 series instrument equipped with an HP-5 column (initial temperature was set at 50 °C for 2 minutes with a ramp of 20 °C/min and a final temperature of 280 °C).

Gel-permeation chromatography (GPC) was performed on a Waters 2487 liquid chromatograph equipped with Breeze software, Shodex KF-803L and Shodex KF-806L GPC columns in series with a Shodex KF-G guard column, a Waters 2487 Dual  $\lambda$  Absorbance Detector, and a Waters 2410 Refractive Index Detector. THF was used as the eluent at a flow rate of 1.0 mL/min, and the instrument was calibrated with 15 polystyrene standards (Aldrich, 760-1.8 x 10<sup>6</sup> Daltons).

Thermal gravimetric analysis (TGA) of **ROMP-poly1**, poly(terthiophene) made from FeCl<sub>3</sub>-induced polymerization, and FeCl<sub>3</sub>-induced cross-linked **ROMP-poly1** was carried out on a TA Instruments SDT 2960 Simultaneous DTA-TGA. A TA Instruments Model 2950 Thermogravimetric Analyzer was used for TGA of films of electrochemically synthesized poly(terthiophene) and cross-linked **ROMP-poly1** on gold electrodes.

Cyclic voltammetry was performed on a CHI900 Scanning Electrochemical Microscope. A conventional three-electrode cell was used for all electrochemical experiments (indium tin-oxide (ITO)-coated glass or 50-nm Au/Si (Au on Si substrate) working electrode, Ag/Ag<sup>+</sup>Cl<sup>-</sup> reference electrode, and Pt wire counter electrode). ITO-coated glass substrates, purchased from Delta Technologies, were cleaned by immersing in a piranha solution (conc. H<sub>2</sub>SO<sub>4</sub> + 30% H<sub>2</sub>O<sub>2</sub>

in approx. 3:1 v/v ratio) for 5 minutes followed by immersion in 1 M HCl (aq) for 5 minutes, and drying under a purified N<sub>2</sub> stream. Silicon substrates were purchased from Montco Silison Technologies, Inc. and coated with Au by chemical vapor deposition (CVD). Interdigitated array (IDA) electrodes (15 μm wide, 4800 μm long, 0.1 μm high, and 15 μm spacing) were purchased from Microsensor Systems Inc. and were used for conductivity studies.

A Zeiss Axiovert-100 optical microscope with fluorescence filter kit and a Pixera 600-CL digital image recorder were employed for fluorescence microscopy. A Jasco V-530 UV-Visible spectrometer was used to find absorbance maxima for polymer films on ITO-Glass. Fluorescence spectroscopy was performed using a Jobi Yvon-Spex Fluorolog-3 instrument. Atomic force microscopy (AFM) experiments were carried out on a Digital Instruments scanning probe microscope in tapping mode.

#### 2.4.2. Materials

All reactions were carried out under inert atmosphere using standard Schlenk techniques or in an inert-atmosphere glovebox, unless otherwise noted. All solvents were purified using the Dow-Grubbs solvent purification system,<sup>57</sup> collected under argon into Strauss flasks, and degassed with nitrogen prior to use. Deuterated solvents were purchased from Cambridge Isotope Laboratories and used without further purification.

3'-(*Exo*-5-norbornene-2-oxymethyl)-2,2':5',2''-terthiophene (**2.1**) was synthesized following a literature procedure.<sup>19</sup> Plating solutions, 1025 RTU (Ag) and Orotemp 24 RTU (Au), were purchased from Technic, Inc. (Anaheim, CA). All other reagents were purchased from Acros, Strem, or Aldrich Chemical Co., and used without further purification.

### 2.4.3. Conditions for ROMP of **2.1**

A solution containing an appropriate amount of  $\text{Cl}_2(\text{PCy}_3)_2\text{Ru}=\text{CHPh}$  (**2**) (1.7 mg, 0.0021 mmol; 3.4 mg, 0.0041 mmol; 6.8 mg, 0.0082 mmol; 11.3 mg, 0.0137 mmol; 13.6 mg, 0.0164 mmol; 16.9 mg, 0.0205 mmol; and 22.5 mg, 0.0273 mmol) for the synthesis of 200-, 100-, 50-, 30-, 25-, 20- and 15-mers, respectively), in  $\text{CH}_2\text{Cl}_2$  (1 mL) was injected into a stirring solution of monomer **2.1** (150 mg, 0.41 mmol) in  $\text{CH}_2\text{Cl}_2$  (5 mL). The mixture was allowed to stir for 20 minutes, and was terminated by the addition of excess ethyl vinyl ether (1 mL). Volatile components were removed under vacuum; the polymer was precipitated twice from stirring hexane (100 mL) and dried under vacuum to yield a light green powder (**ROMP-poly1**, 140 mg, 93%).

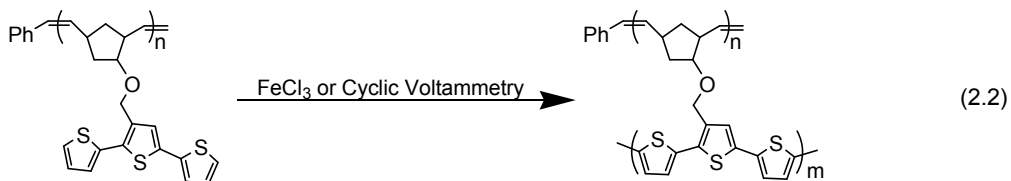
**Table 2.2.** Polymer characterization data for the ROMP of **2.1**.

Monomer/Catalyst	$M_n$	PDI
15	8,429	1.28
20	11,796	1.24
25	11,915	1.22
30	13,161	1.18
50	20,153	1.12
100	31,697	1.10
200	60,323	1.16

### 2.4.4. Oxidative cross-linking of **ROMP-poly1** and polymerization of terthiophene with $\text{FeCl}_3$

$\text{FeCl}_3$  (199 mg, 1.23 mmol) was placed in a 50-mL Schlenk flask containing a magnetic stirring bar, and  $\text{CH}_2\text{Cl}_2$  (10 mL) was added to make a brown-black suspension. A solution of **ROMP-poly1** (50 mg, 0.14 mmol of terthienyl units) in  $\text{CH}_2\text{Cl}_2$  (5 mL) was injected into the flask, and the mixture was refluxed under nitrogen for 24 h (Eq 2.2). The reaction contents were poured into MeOH (50 mL) and filtered to give a brown powder. The crude polymer was further purified via a Soxhlet extraction (reflux MeOH, 24 h), and dried under vacuum (60 mTorr, 12 h)

to yield a dark powder (45 mg, 90%). 2,2':5',2''-terthiophene was polymerized in this same manner (Eq 2.3) to give powder poly(terthiophene).



#### 2.4.5. Electrochemical cross-linking of ROMP-poly1 and polymerization of terthiophene

Dark orange films were formed by the electrochemical cross-linking of **ROMP-poly1** (6 mg, 0.014 mmol) on ITO-coated glass in 0.1 M tetrabutylammonium hexafluorophosphate (TBAPF<sub>6</sub>)/CH<sub>2</sub>Cl<sub>2</sub> (5 mL) by repeated scanning between -0.35 and 1.80 V or -0.35 and 1.27 V at a scan rate of 100 mV/s (Eq 2.2). Films that were immediately removed from the CH<sub>2</sub>Cl<sub>2</sub>/electrolyte solution and placed in the open atmosphere dried too quickly, and were prone to cracking. Hence, evaporation of solvent was controlled by allowing the film to dry for 2 minutes inside the electrochemical cell, just above the liquid surface. 2,2':5',2''-Terthiophene was also electrochemically polymerized in this same manner (Eq 2.3) to give films of poly(terthiophene). For TGA studies, films were similarly prepared from **ROMP-poly1** and terthiophene using a Au/Si working electrode.

#### 2.4.6. *In-situ* conductivity measurements of cross-linked films

Cross-linked films of **ROMP-poly1** and poly(terthiophene) were deposited on IDA electrodes using the electrochemical methods described in the previous section. During polymer deposition, both leads of the IDA were connected and used as the working electrode and thirty layers were deposited for each film. The polymer-coated array was then placed in a monomer-

free electrolyte solution, and scanned from  $-0.35$  to  $1.27$  V for thirty cycles. Although the continuity of the resulting film over the entire IDA electrode can be visually ascertained using an optical microscope, it can also be verified electrochemically in a fresh electrolyte solution. Cycling the two bands together and then individually between  $-0.35$  to  $1.27$  V gave identical I-V curves, indicating good communication between the individual leads of the array.<sup>33</sup> *In-situ* conductivity as a function of doping potential was measured using Wrighton's methods<sup>30,32,33</sup> as adapted by Reynolds.<sup>31</sup> Static potentials ranging from  $0.0$  to  $1.30$  V were used to dope the polymer films. In general, one band of electrodes was held at the desired potential and the other band was cycled  $\pm 0.05$  V from the desired potential ( $0.001$  V/s scan rate). After two complete cycles, no hysteresis was observed, indicating that the film is fully doped. The resistance of the film is measured using the I-V data of the third cycle.

#### **2.4.7. Thermal gravimetric analysis (TGA) of poly(terthiophene) and ROMP-poly1 materials**

Powder samples of **ROMP-poly1**, poly(terthiophene) made from  $\text{FeCl}_3$ -induced polymerization, and  $\text{FeCl}_3$ -induced cross-linked **ROMP-poly1** (4-6 mg) were loaded into to the TGA instrument and heated from  $40$  °C to  $900$  °C at a rate of  $3$  °C per minute under  $\text{N}_2$  atmosphere. Electrochemically prepared films of cross-linked **ROMP-poly1** and poly(terthiophene) on a Au/Si electrode were evaluated by the same method using a bare Au/Si electrode as the reference. Percent weight loss of the samples was recorded over the  $40$  °C to  $900$  °C temperature range.

#### **2.4.8. Electrochemical doping of cross-linked ROMP-poly1 and poly(terthiophene) with $\text{ClO}_4^-$**

Films of electrochemically prepared cross-linked **ROMP-poly1** and poly(terthiophene) on ITO-coated glass were transferred into a three-electrode cell containing an acetonitrile solution of the supporting electrolyte (0.1 M tetrabutylammonium perchlorate (TBAP)). Using the electrochemical set-up described previously, with ITO-coated glass as the working electrode, the polymer films were doped by scanning the potential from either  $-0.35$  to  $1.80$  V or  $-0.35$  to  $1.27$  V.

#### **2.4.9. Fluorescence microscopy imaging of cross-linked ROMP-poly1 and poly(terthiophene)**

Films of electrochemically cross-linked **ROMP-poly1** and poly(terthiophene) on ITO-coated glass were excited by mercury lamp and digital images were recorded. Excitation and emission light were passed through a pair of fluorescence filters before viewing (excitation filter options: 340-380, 460-500, or 533-587 nm; emission filter options: 435-485, 510-560, or 608-682 nm).

#### **2.4.10. Fluorescence spectra of cross-linked ROMP-poly1 and poly(terthiophene)**

Films of electrochemically cross-linked **ROMP-poly1** and poly(terthiophene) on ITO-coated glass were irradiated at absorbance maxima using an xenon lamp, and emission spectra were recorded.

#### **2.4.11. Atomic force microscopy**

High-resolution surface images were obtained by atomic force microscopy (AFM) and were used to determine the root-mean-square (rms) of roughness for films electrochemically deposited on ITO electrodes. Tapping-mode AFM scans were taken of the various cross-linked ROMP polymers and poly(terthiophene) at 0.5 Hz with image sizes from  $100 \mu\text{m}$  to  $1 \mu\text{m}$ .

### 2.4.12. General synthesis of Au-polymer-Au rods

Using metal vapor deposition, a 200-nm AAO membrane was first coated with a 200 nm layer of Ag and used as the working electrode in custom-built three-electrode electrochemical cell (Figure 2.17). At a potential of -0.9 V, a base layer of Ag was deposited (from 1025 RTU solution) into the pores of the AAO working electrode until a charge of 1 C was reached. The Ag base layer was followed by Au deposition (from Orotemp 24 RTU solution) at -0.9 V until 1 C was reached. Thiophene-based monomers/electrolyte solutions were then added to the cell, and oxidatively polymerized. For dual-capped rods, a top metal layer (Au) was added at a potential of -1.0 V until a charge of 1 C was reached. Rods were released by removing the Ag backing with  $\text{HNO}_3$ , and dissolving the template with NaOH.

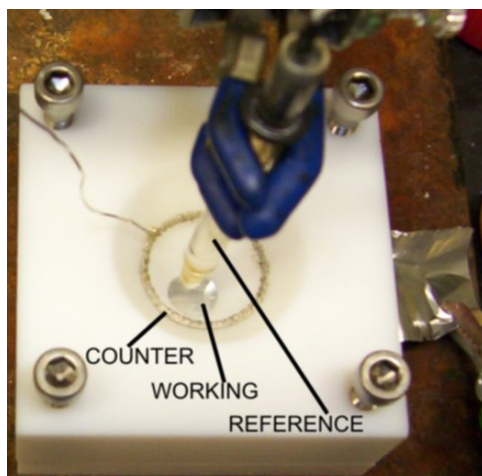


**Figure 2.17.** Electrochemical cell used in the synthesis of Au-Polymer-Au nanorods.



## Chapter 3

### Small Molecule-DNA Hybrids

Portions of this chapter appear in the following manuscript:

Stepp, B. R.; Gibbs-Davis, J. M.; Koh, D. L. F.; Nguyen, S. T. *J. Am. Chem. Soc.* **2008**, *130*, 9628-9629.

### **3.1. Aggregates of DNA hybrid materials**

#### **3.1.1. Background**

Recent research efforts have led to the identification of specific genes which underlie complex and late-onset diseases.<sup>1,2</sup> Early diagnosis and detection of debilitating diseases such as Parkinson's, Alzheimer's, and Huntington's offer patients the option of early treatment, and the potential to live longer and healthier lives. However, a crucial component of such preventive treatment is the reliable detection of disease-causing genes.

Most of the nearly 4,000 known genetic diseases are the result of a deviation from the normal genetic code in one of the trillions of bases that make up the human genome.<sup>3</sup> Accordingly, recognizing these deviations in sequence-specific DNA strands, which often take the form of single-base mutations, or single-nucleotide polymorphisms (SNPs), has been crucial in the development of highly sensitive DNA assays.<sup>4,5</sup> SNP recognition is also important in the testing for infectious diseases where the unique biomarker DNA from a virulent pathogen often differs from a non-virulent one by only one base pair.<sup>3</sup> To probe the presence of specific target DNA strands and discriminate SNPs, current detection systems have employed a wide range of signaling mechanisms that include radioactivity, fluorescence, colorimetry, and electrochemistry.<sup>6-8</sup>

DNA hybrid materials have emerged as a potential vehicle for facile sensing and reporting of DNA SNPs.<sup>9,10,11</sup> These materials function by capturing the desired target DNA strand from a complex solution and forming aggregates that have enhanced melting behaviors, thus providing the means to separate the desired target from other biological compounds/polymers through temperature manipulation. In addition, the formation of such

aggregates can often be detected by electrochemical activity,<sup>12</sup> and/or distinct physical changes such as color,<sup>13</sup> allowing for rapid detection. Despite these advances, the fundamental physics underlying the enhanced melting behaviors of these hybrid DNA materials are not well understood. A more complete understanding will likely lead to improved DNA detection platforms. This thesis chapter attempts to untangle some of the parameters that govern this behavior through several model systems.

### **3.1.2. Melting properties of DNA hybrid aggregates**

While unmodified DNA:DNA duplexes are known to dehybridize when heated, such melting transitions occur over a broad range of temperatures.<sup>3</sup> As shown in Figure 3.1, Panel A, the dehybridization profile of a DNA duplex can be plotted as the percent of remaining double-stranded DNA at any given temperature, which is inversely proportional to the amount of DNA that has denatured into two separate strands at that same temperature. The inflection point of this “melting curve” is defined as the analytical melting point ( $T_m$ ) of the DNA duplex. These melting profiles can be used to compare the hybridizations between a single-stranded DNA and either its perfectly complementary sequence or a strand that contains a single-base mismatch. Because the duplex formed from the latter combination contains fewer hydrogen bonds, it is inherently less stable than the complementary duplex and thus have a lower melting point.

The observed  $T_m$  depression for mismatched DNA duplex is often used to separate mixtures of perfectly complementary and mismatched DNA duplexes through a series of stringency washes at the temperature where the difference in hybridization between the two species is largest.<sup>14</sup> Such stringency washes eliminate the melted SNP-containing strands away from the fully complementary duplexes. A problem arises, however, when the melting profile is

broad, making it difficult to separate a mixture of complementary/mismatched duplexes because they both denature over a similar temperature range (Figure 3.1, Panel A).

In contrast to unmodified DNA:DNA duplexes, hybridized mixtures of materials containing multiple DNA strands, such as DNA-functionalized comb polymers (polymer-DNA)<sup>12</sup> and DNA-functionalized gold nanoparticles (GNP-DNA),<sup>15</sup> have notably sharpened melting curves that easily distinguish SNPs from complementary duplexes (Figure 3.1, Panel B). The enhanced melting properties of these systems have attracted the interest of numerous research groups, leading to several DNA detection strategies<sup>16,17</sup> and multiple theoretical studies.

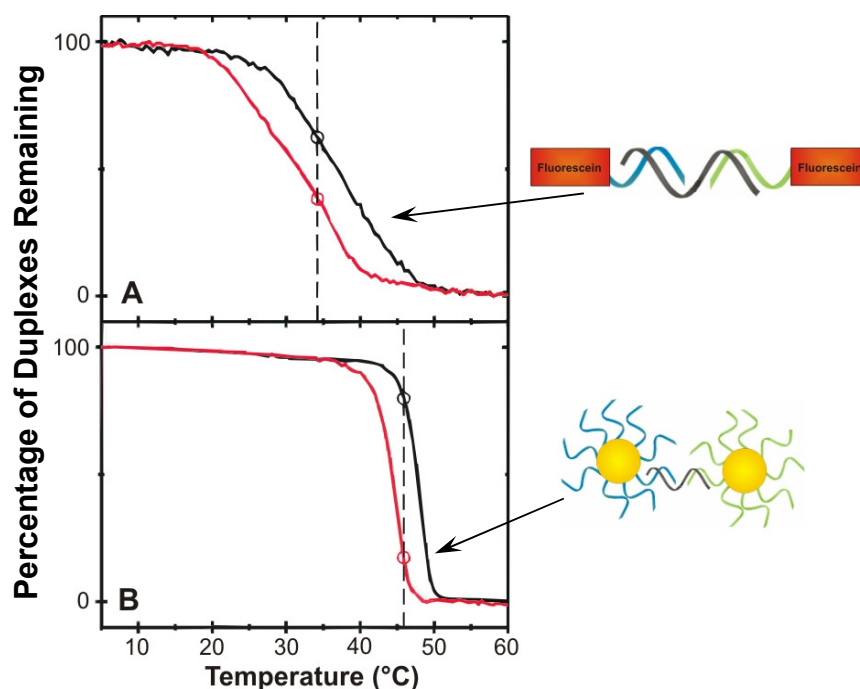


**Figure 3.1** Distinct sharpening of the melting profiles between free DNA (A) and aggregates of GNP-DNA hybrids (B). In each graph the red curve is for an SNP-containing DNA duplex, and the black curve is perfectly complementary (Figure adapted from Taton et al. *Science* **2000**, 289, 1757-1760<sup>15</sup>).

In one such theoretical study, the enhanced melting profiles of polymer-DNA and GNP-DNA hybrids have been attributed to the cooperative melting of neighboring duplexes.<sup>16</sup> This

‘neighboring-duplex’ model proposes that hybridization of complementary multi-DNA materials leads to a network of intra-linked DNA duplexes where the condensed ion cloud around each DNA duplex can appreciably overlap with those of its neighbors. Under these conditions, the coalesced ion cloud stabilizes the duplexes, causing them to melt as a *cooperative* unit in a switch-like fashion.<sup>18</sup> Such cooperative melting is predicted to be observable with as few as 2-3 cooperative duplexes.<sup>19,20</sup>

Alternatively, the macroscopic aggregate models brought forth by Park et al.<sup>21</sup> and Lukatsky et al.<sup>22</sup> both argue that the sharp melting transitions observed for DNA-hybrid materials, such as GNP-DNA hybrids, arise from the dense networks (sol-gels) of nanoparticles that form when complementary GNPs containing numerous DNA strands are linked to several nearest-neighbor GNPs through multiple DNA duplexes. In these models, the observed sharp melting is attributed a macroscopic phase-transition when a network of >1,000 nanoparticles dehybridizes from the gel to the dilute (liquid) phase.

Comparing the aforementioned theories, the neighboring-duplex model describes a molecular-scale phenomenon where cooperative interactions between two or more neighboring duplexes lead to sharper melting<sup>16</sup> than what is predicted by the phase-transition models alone and has been shown to be more descriptive of the melting transitions seen for polymer-DNA and GNP-DNA systems.<sup>20</sup>

### **3.1.3. Use of SMDHs to elucidate factors affecting enhanced melting**

As described above, the enhanced melting profiles of DNA hybrid materials can be used to take advantage of the disparity between ‘normal’ and SNP-containing DNA duplexes. While aggregated DNA hybrid materials have been widely studied<sup>15</sup> and even implemented in

commercial separation devices, a complete description of the parameters affecting their aggregation and melting has yet to be achieved. To successfully create a rapid, finely tuned recognition assay for SNPs in DNA, the factors that govern the interaction between the detecting and target DNA sequences must be fully understood.

It has been proposed that the enhanced melting properties of DNA-hybrid materials are due to the presence of multiple DNA linkages in close proximity;<sup>23</sup> however, the parameters which govern the enhanced melting behavior such as the number of DNA strands per unit-structure, the distance between adjacent DNA strands, and the geometrical placement between strands remain unknown quantities. Because the syntheses of polymer-DNA and GNP-DNA hybrids do not allow for precise control of the number or the spacing of the DNA strands, small molecule-DNA hybrids (SMDH)s were chosen as a model for evaluating these factors.

By design, the positions and geometry of an SMDH's component DNA strands can be precisely modified and controlled (*vide infra*), allowing for a detailed analysis of structure-property relationships in SMDH:SMDH aggregates and a more detailed understanding of parameters that affect the melting transitions in DNA hybrid materials.<sup>16</sup> A better understanding these parameters will allow us to develop a model that can be applied to optimize the design of small molecular probes involved in the specific targeting of DNA and proteins.

## 3.2. Benzyl phosphate-linked rigid small molecule-DNA hybrids

### 3.2.1. Introduction

To further our understanding of the relationship between the structure of DNA-hybrid materials and their observed melting properties, we first designed a series of rigid small-molecule DNA hybrids (rSMDHs). These rSMDHs are structurally similar to the diphenylacetylene linkers previously developed for our polymer-DNA hybrids (Figure 3.2).<sup>24</sup>

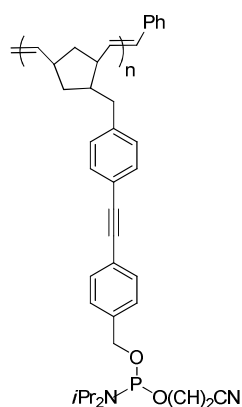


**Figure 3.2.** Structure of our polymer precursor to the polymer-DNA hybrid prior to DNA coupling to the pendant phosphoramidites. The side chain contains the rigid diphenylacetylene linker found in the rigid small molecule-DNA hybrids (Figure 3.3).

Phenylacetylene was specifically chosen as the molecular scaffold to provide a rigid spacer between the DNA strands and the molecular core in our rSMHDs, while a benzyl phosphate linkage from the core to the DNA would permit attachment through standard phosphoramidite-DNA coupling chemistry. This design allows for precise control over the geometrical placement and chain density of the coupled DNA strands in each rSMDH (Figure 3.3).

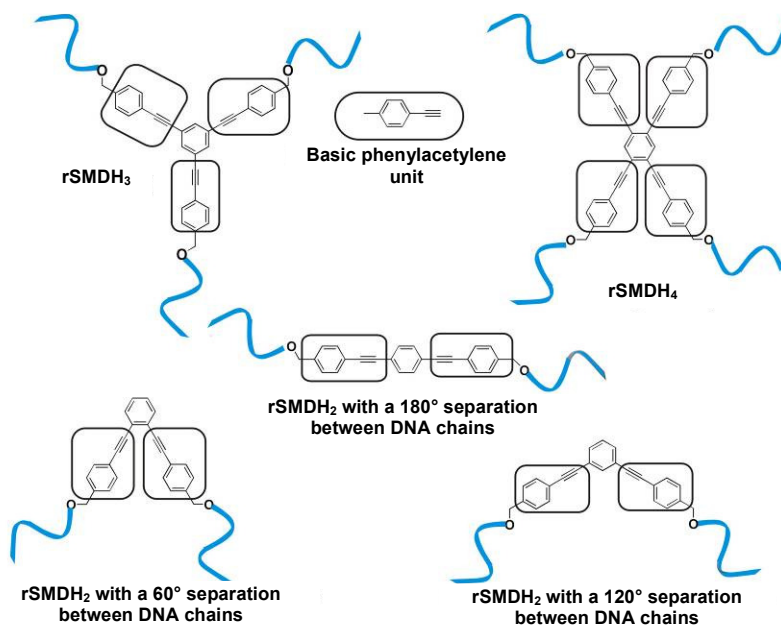


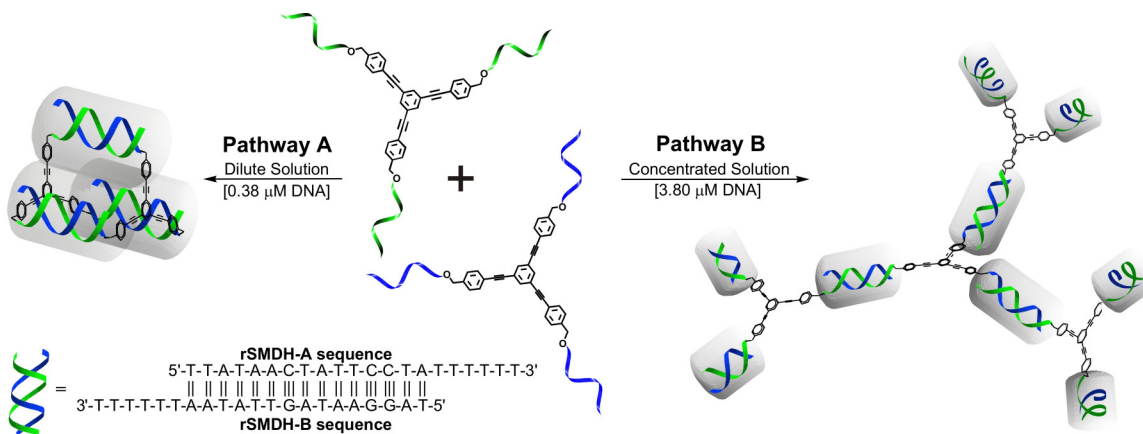
**Figure 3.3.** Examples of rigid small-molecule-DNA hybrids (rSMDHs).

### 3.2.1.1. Aggregates of rSMDH<sub>3</sub>—enhanced melting by design

Previous theoretical<sup>25</sup> and experimental<sup>26</sup> studies on the aggregation behavior of complementary (A and B) structures with three or more ‘arms’ surrounding a central hub found that A:B dimers tend to form when the corresponding partners are combined in dilute solutions. Accordingly, a dilute 1:1 mixture of rSMDH<sub>3</sub> molecules possessing three complementary DNA strands, attached through the 5’ terminus, should result in ‘caged’ dimers (Scheme 3.1, pathway A). Proper spacing between the rigid small-molecule core by a short spacer sequences consisting thymidine units will allow these dimers to have all three duplexes parallel to each other at approximately 20-40 Å duplex center-duplex center distances, within the theoretical distance necessary for ion-cloud overlap.<sup>19</sup> In contrast, concentrated samples are not expected to melt cooperatively as they should form large aggregates (Scheme 3.1, pathway B) with the ion clouds not in parallel alignment.



**Scheme 3.1.** Two aggregate pathways for mixture of complementary rSMDH<sub>3</sub> molecules: rSMDH-A and rSMDH-B.

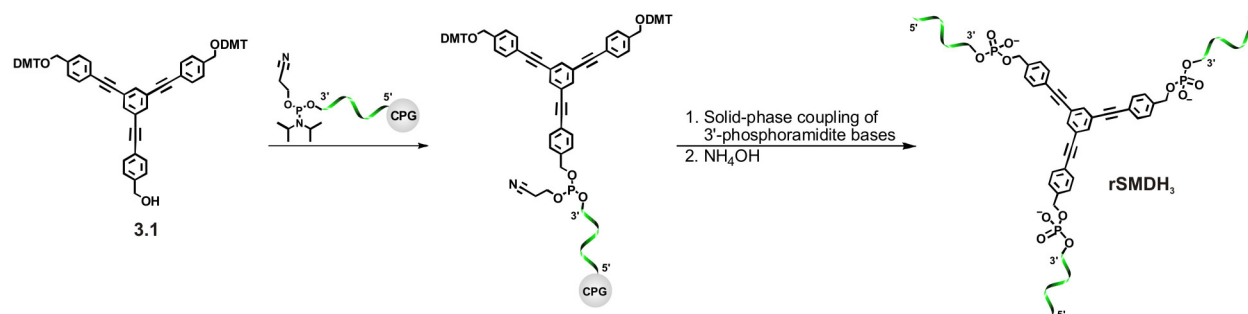


To date, switch-like melting transitions have only been observed for large polymer-DNA<sup>12</sup> and GNP-DNA aggregates<sup>15</sup> linked through numerous DNA duplexes. This section describes the first observation of cooperative melting in discrete DNA-hybrid structures where cage dimers are formed from small molecule-DNA hybrids (SMDHs) possessing *only* three DNA strands around a rigid (r) small-molecule core (Scheme 3.1, pathway A).

### 3.2.2. Results and discussion

#### 3.2.2.1. Synthesis of rSMDH<sub>3</sub> hybrids

Symmetric rSMDH<sub>3</sub> molecules were synthesized with a rigid tris(phenylacetylene) core that allows for the placement of exactly three DNA strands at 120° intervals with a fixed distance from the central benzene. In a method similar that described by Shchepinov et al.,<sup>26</sup> rSMDH<sub>3</sub> materials were prepared by synthesizing the initial DNA strand from the surface of a controlled porosity glass bead (CPG), followed by addition of the small-molecule core **3.1** and coupling of the two remaining DNA arms (Scheme 3.2). Following removal from the solid support, the crude rSMDH<sub>3</sub> products were purified by size-selective dialysis to give the desired triply functionalized rSMDH<sub>3</sub>.

**Scheme 3.2.** Synthesis of rSMDH<sub>3</sub>.

### 3.2.2.2. Hybridization and melting of rSMDH<sub>3</sub> aggregates

Aggregate samples of rSMDH<sub>3</sub> were formed by combining equimolar amounts of two complementarily functionalized rSMDH<sub>3</sub> molecules in phosphate buffer at 50 °C, annealing the mixture at 50 °C for 5 minutes, and allowing the mixture to cool to room temperature over 8 h. The melting profile of the hybridized mixture was ascertained by heating the samples from 15 °C to 70 °C at a rate of 1 °C per minute while monitoring the increase in UV absorbance at 260 nm at 0.1-°C intervals. As predicted by the neighboring-duplex model,<sup>16</sup> the  $T_m$  and the overall melting range of rSMDH<sub>3</sub> mixtures differ significantly depending on the concentration (Figure 3.4). Most notably, the dilute sample (0.38  $\mu\text{M}$  [DNA]) has a  $T_m$  of 52 °C and a FWHM (full width at half max of the derivative curve) of 2.5 °C, 12 °C higher and considerably sharper than a DNA:DNA duplex of the same sequence (Table 3.1, entries 1 and 2). Conversely, the concentrated sample (3.80  $\mu\text{M}$  [DNA]) has a  $T_m$  of 41.5°C and a FWHM of 17.5 °C—nearly identical to that of unmodified DNA duplexes.

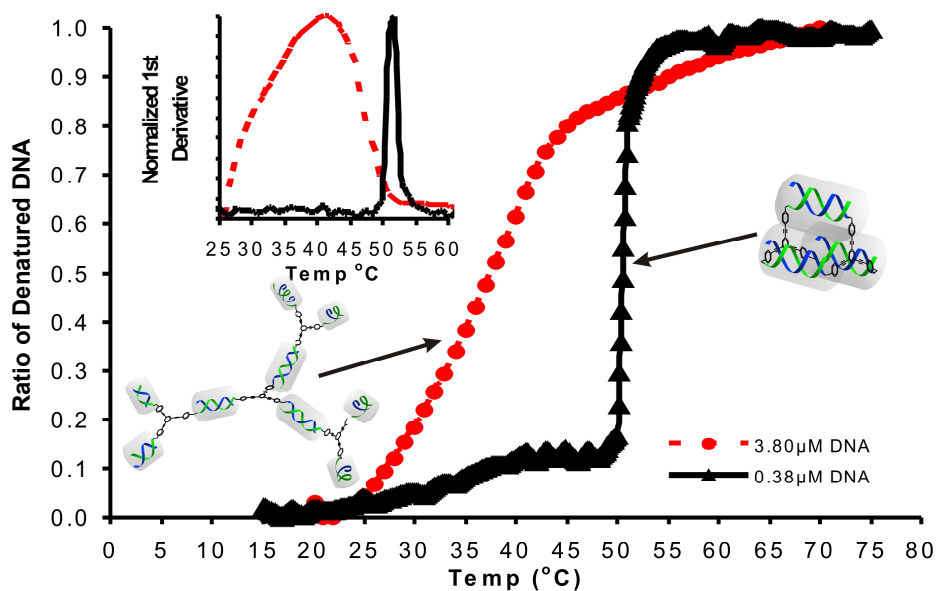


**Figure 3.4.** Melting curves for rSMDH<sub>3</sub>:rSMDH<sub>3</sub> hybridization mixtures at high (3.80 μM) and low (0.38 μM) concentrations in saline buffer (10 mM PBS, pH = 7.0, 150 mM NaCl). Inset: First derivatives of the melting curves.

**Table 3.1.** Melting data for unmodified DNA (DNA:DNA) and rSMDH<sub>3</sub> (rSMDH<sub>3</sub>:rSMDH<sub>3</sub>) aggregates.

Entry	Hybridization mixture	[DNA] (μM)	[NaCl] (mM) <sup>a</sup>	T <sub>m</sub> (°C)	FWHM (°C)
1	DNA:DNA	0.38	150	39.2	20.0
2	DNA:DNA	3.80	150	44.1	23.0
3	rSMDH <sub>3</sub> :rSMDH <sub>3</sub>	3.80	75	37.5	20.0
4	rSMDH <sub>3</sub> :rSMDH <sub>3</sub>	3.80	150	41.5	17.5
5	rSMDH <sub>3</sub> :rSMDH <sub>3</sub>	3.80	300	49.0	22.0
6	rSMDH <sub>3</sub> :rSMDH <sub>3</sub>	0.38	75	43.2	3.2
7	rSMDH <sub>3</sub> :rSMDH <sub>3</sub>	0.38	150	51.5	2.0
8	rSMDH <sub>3</sub> :rSMDH <sub>3</sub>	0.38	300	56.0	3.7

<sup>a</sup> NaCl concentration in a 10-mM PBS buffer solution at pH 7.0.

### 3.2.2.3. The number of cooperative duplexes in rSMDH aggregates

Using the neighboring-duplex theory,<sup>16,18</sup> the number of duplexes interacting cooperatively can be determined from the salt-concentration dependence of the melting temperature for the rSMDH<sub>3</sub> hybridization mixtures (Table 3.1, entries 3-8). The average number of cooperative duplexes is calculated to be 2.97 for the caged dimers in the dilute samples and 0.91 for the concentrated samples where larger aggregates are favored (See section 3.5.5 for details). This ‘speciation’ is further confirmed by the non-denaturing PAGE gel shown in Figure 3.5: the dilute sample (lane 1) eluted quickly as a well-defined spot, signifying a single entity with low charge/volume ratio that is, consistent with the compactness of the caged dimer. In contrast, the concentrated sample (lane 4) eluted slowly as a long band with many species. The species in both lanes 1 and 4 eluted slower than the free rSMDH<sub>3</sub>-A (lane 3), consistent with their hybridized states.

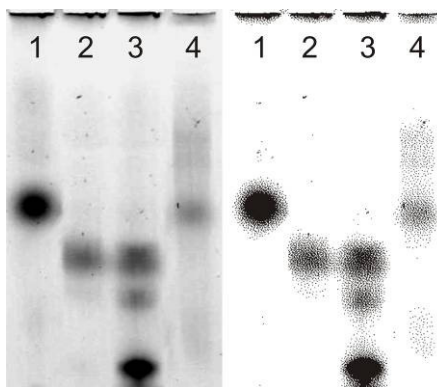


**Figure 3.5.** Digital images of the non-denaturing PAGE gel of rSMDH<sub>3</sub> hybridization mixtures. Right: Grayscale image; Left: Black-and-white image with background subtraction. Lane 1: A:B rSMDH<sub>3</sub> cage dimers formed in dilute solution. Lane 2: Purified non-hybridized rSMDH<sub>3</sub>-A. Lane 3: Crude sample of non-hybridized rSMHD<sub>3</sub>-A before purification. Lane 4: A:B rSMDH<sub>3</sub> aggregates formed in concentrated solution.

Shchepinov et al. reported that DNA hybrids with a flexible dendrimer core can form 1:1 dimer structures upon annealing.<sup>26</sup> While these flexible dimers also exhibited increased melting temperatures, their dehybridization profiles are broad like that of unmodified DNA duplexes. Together with our data, this observation suggests that while multivalent interactions are responsible for enhanced melting temperature, the rigid core of our rSMDH<sub>3</sub> system is critical in forcing the connected DNA duplexes to remain in the parallel geometry that is necessary for cooperative interactions via shared ion clouds.<sup>19</sup> It is noteworthy that hybridized mixtures containing a high concentration of rSMDH<sub>3</sub> did not exhibit enhanced melting temperature (Table 3.1), presumably due to the lack of multivalent interactions between neighboring rSMDH<sub>3</sub> molecules: on average each rSMDH<sub>3</sub> is only linked to another rSMDH<sub>3</sub> through a single DNA duplex.

### **3.2.3. Conclusions**

In conclusion, well-defined rSMDHs possessing three DNA strands have been synthesized and used to form caged dimers in dilute solutions. These caged dimers comprise the first discrete small molecule-DNA hybrids that exhibit both switch-like dehybridization properties and enhanced melting temperatures similar to GNP-DNA<sup>15</sup> and polymer-DNA hybrids.<sup>12</sup> These results provide strong evidence to support the neighboring-duplex model as a critical tool for understanding hybridization/dehybridization processes in DNA-linked aggregates at the discrete molecular/supramolecular level where phase-transition theories relying on gel formation cannot be applied. It may also allow researchers to push the limits in the design of the next generation of DNA-based materials to maximize DNA's natural recognition ability via precisely spaced and finely tuned duplex interactions.

### 3.3. Synthesis and melting properties of flexible SMDHs

#### 3.3.1. Introduction

In section 3.2, rSMDH<sub>3</sub> molecules were synthesized and the enhanced melting properties of their resulting rSMDH<sub>3</sub>:rSMDH<sub>3</sub> dimers and aggregates were discussed. Thus far, the three cooperative duplexes demonstrated for the rSMDH<sub>3</sub> system represents the fewest number of cooperative duplexes in a discrete structure; however, theory predicts that systems with as few as two cooperative duplexes should also demonstrate enhanced melting properties.<sup>19</sup> To examine this lower limit, we designed a double-clip aggregate (Figure 3.6) consisting of two low-melting DNA duplexes (40 °C) held in close proximity by two high-melting (70 °C) ones at the end of the clip. The center duplexes and the end duplexes are held linked together through a flexible small molecule linker. If the melting temperatures of the high-melting and low-melting duplexes are adequately separated, then two separate  $T_m$ 's should be observed for the linked aggregate.<sup>18</sup> Additionally, if the two low-melting duplexes experience sufficient cooperativity, then the lower portion of the aggregate melting profile should be sharpened, with the first  $T_m$  raised in comparison to the free DNA duplexes (Figure 3.6, Inset graph).

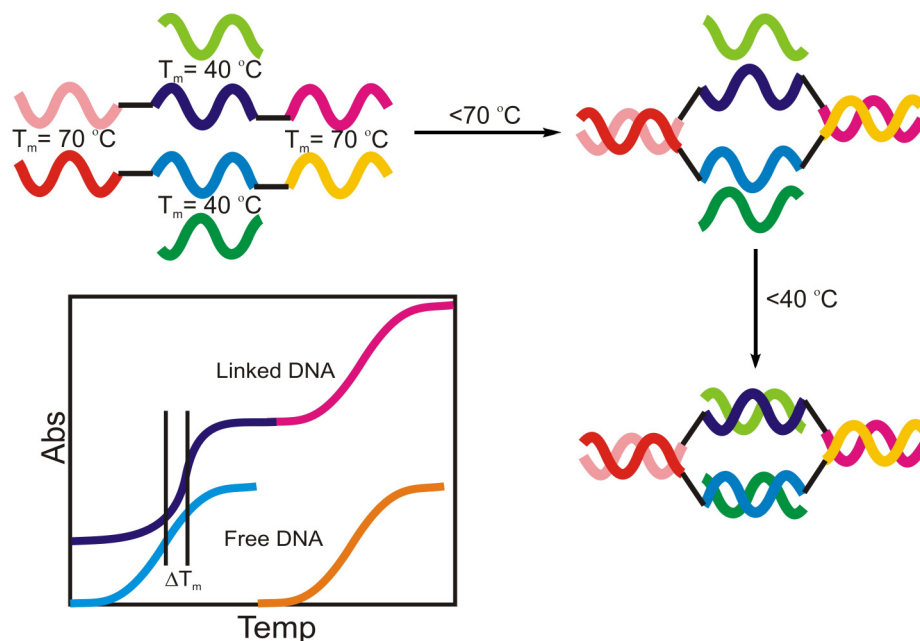


**Figure 3.6.** Schematic drawing for a system containing four DNA duplexes (colored waves) held together by flexible linkers (black lines). Inset shows the proposed melting curves of the free DNA duplexes and the four-duplex aggregate.

### 3.3.1.1. Flexible SMDHs

Flexible SMDHs (fSMDHs) are synthesized with two poly(ethylene glycol) (PEG) spacers between three DNA strands, and the melting properties of their hybridized structures are evaluated. The flexible PEG spacers have several advantages over the previously described rSMDHs described in section 3.2: general synthesis of fSMDHs is facilitated by commercial availability, differentiation is simplified through variation in length of PEG spacer (Figure 3.7), and stability of the alkyl phosphate linkages has been previously demonstrated.<sup>27,28</sup>

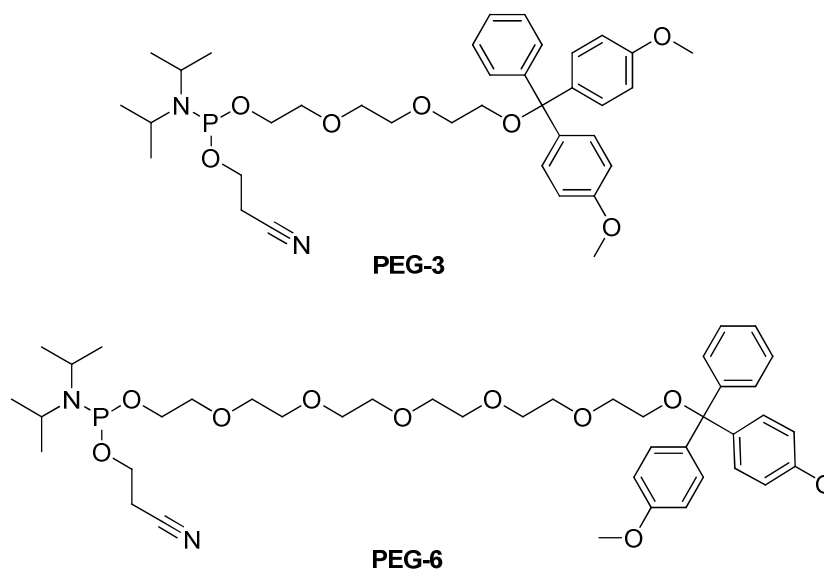


**Figure 3.7.** Two length variants of commercially available PEG-phosphoramidites for use in solid-phase synthesis of spacer-interrupted DNA strands.

### 3.3.2. Results and discussion

#### 3.3.2.1. Synthesis of fSMDHs

As shown in Figure 3.6, four strands of DNA are required to assemble the full fSMDH aggregate: two low-melting single strands (**3.9** and **3.10**) and two longer strands comprised of an inner low-melting sequence separated from two outer high-melting sequences by PEG spacers. Variation of the distance between the middle duplexes was accomplished by synthesizing the longer strands with both PEG<sub>3</sub> and PEG<sub>6</sub> as the spacers (**3.11** and **3.12**; **3.13** and **3.14**). Additionally, the corresponding unlinked DNA strands were synthesized for comparison of the “free” duplexes to the four-duplex aggregate (**3.15**, **3.16**, **3.17**, **3.18**, **3.19**, **3.20**). The sequences for each of the four duplexes were designed based on their predicted  $T_m$ 's and the absence of any high-melting hairpin forming or self-annealing sections (Figure 3.8).<sup>29</sup>



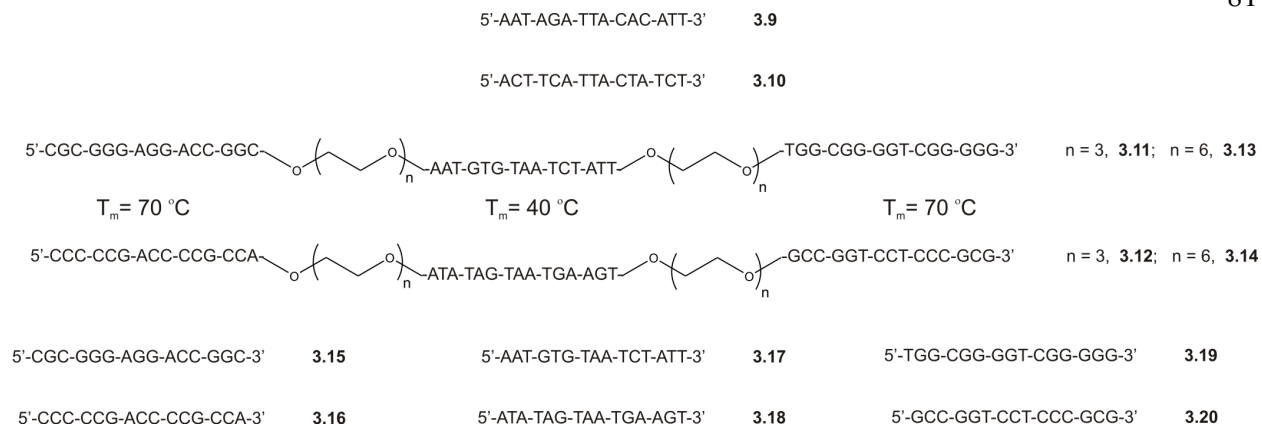


**Figure 3.8.** Twelve DNA sequences synthesized for use in the fSMDH studies.

### 3.3.2.2. Melting experiments

Our design of the four-duplex fSMDH aggregate requires adequate separation of the high-melting and low-melting portions such that the two melting transitions do not overlap. As expected, the low-melting duplexes (**3.9** with **3.17** and **3.10** with **3.18**) melted at 39.5 and 39.2 °C, respectively, and the high-melting duplexes (**3.15** with **3.20** and **3.16** with **3.19**) melted at 67.7 and 68.4 °C, respectively. These values provide an ample 28.7 °C separation between the high and low portions (Table 3.2, entries 1-4).

As a control, the long strand **3.11** was combined with the complementary short strands, **3.16**, **3.9**, and **3.20**, and the ensuing aggregate was subsequently dehybridized. The result was a composite of the melting curves observed for the free duplexes, with two transitions occurring at 39.3 °C and 68.8 °C and no change in the peak widths (Table 3.2, entry 5).

Finally, the four-duplex fSMDH aggregate was assembled using **3.9**, **3.10**, **3.11**, and **3.12**. Surprisingly, the lower melting transition for the PEG<sub>3</sub> aggregate was marginally lower (~1 °C) than the free duplexes (Table 3.2, entry 6). This slight  $T_m$  suppression was likely due to the short PEG<sub>3</sub> spacer, which results in sterically hindered and thus destabilized duplexes. Consequently,

a mixed PEG<sub>3</sub>/PEG<sub>6</sub> aggregate was prepared using **3.9**, **3.10**, **3.11**, and **3.14**. To our satisfaction, the  $T_m$  of the lower transition was now higher than the free duplexes by 5 °C (Table 3.2, entry 7). To further increase the spacing, a PEG<sub>6</sub> aggregate using **3.9**, **3.10**, **3.13**, and **3.14**, was prepared; however, the lower  $T_m$  was now equal to the greater of the two free duplexes (Table 3.2, entry 8).

Based on molecular models of the PEG linkers, the PEG<sub>3</sub> is approximately 12 Å in length and the PEG<sub>6</sub> is 24 Å in length. Although complex models allowing for DNA attachment were not considered, these basic calculations put the center-to-center spacings of the middle duplexes at 24 Å, 36 Å, and 48 Å for the PEG<sub>3</sub>, PEG<sub>3</sub>/ PEG<sub>6</sub>, and PEG<sub>6</sub> aggregates, respectively. While the PEG<sub>3</sub> distance of 24 Å would ideally be sufficient, the slightly depressed  $T_m$  suggests inadequate separation of the middle duplexes. Similarly, the spacing of PEG<sub>6</sub> aggregate is likely too large for suitable ion-cloud overlap. Excitingly, the mixed PEG<sub>3</sub>/ PEG<sub>6</sub> aggregate with the intermediate spacing of 36 Å and a 5 °C rise in  $T_m$ , demonstrates melting enhancement between only 2 cooperative duplexes (Figure 3.9).

**Table 3.2.** Summary of melting data for free duplexes and the four-duplex aggregates.

Entry	DNA Components <sup>a</sup>	Linker	Low T <sub>m</sub> (°C)	FWHM Low T <sub>m</sub> (°C)	High T <sub>m</sub> (°C)	FWHM High T <sub>m</sub> (°C)
1	<b>3.9</b> and <b>3.17</b>	-	41.2	11.8	-	-
2	<b>3.10</b> and <b>3.18</b>	-	39.2	11.2	-	-
3	<b>3.15</b> and <b>3.16</b>	-	-	-	67.7	8.2
4	<b>3.19</b> and <b>3.20</b>	-	-	-	68.4	8.7
5	<b>3.11</b> , <b>3.16</b> , <b>3.9</b> , and <b>3.20</b>	PEG <sub>3</sub>	40.9	12.2	68.8	7.8
6	<b>3.9</b> , <b>3.10</b> , <b>3.11</b> , and <b>3.12</b>	PEG <sub>3</sub>	38.4	12.8	76.1	7.4
7	<b>3.9</b> , <b>3.10</b> , <b>3.11</b> , and <b>3.14</b>	PEG <sub>3</sub> /PEG <sub>6</sub>	46.1	12.4	78.2	7.3
8	<b>3.9</b> , <b>3.10</b> , <b>3.13</b> , and <b>3.14</b>	PEG <sub>6</sub>	41.2	13.3	77.8	8.9

<sup>a</sup> Total DNA concentration is 3.6 μM

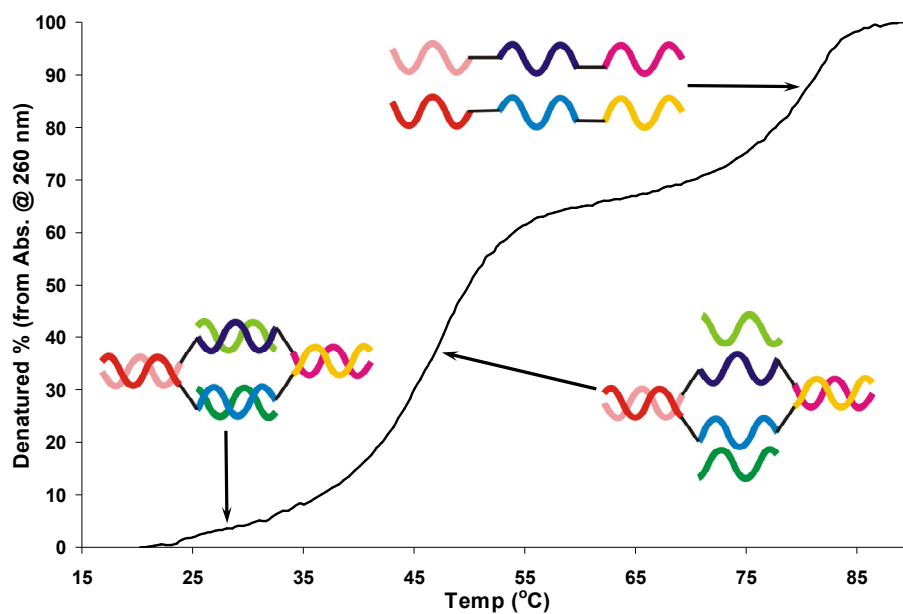


**Figure 3.9.** Melting profile of four-duplex aggregate comprised of **3.9**, **3.10**, **3.11**, and **3.14** at total DNA concentration of 3.6 μM.

### 3.3.3. Conclusions

Four-duplex double-clip DNA aggregates were assembled with varying distances between the middle two duplexes, with the goal of observing enhanced melting between two cooperative duplexes. Based on the lengths of the PEG linkers used, we found 36 Å to be the ideal spacing while 24 Å and 48 Å were either too small or too large. An observed  $T_m$  increase of 5 °C and broad melting transition correlates well with the observations of Shchepinov et al., who previously reported DNA hybrids with flexible dendrimer cores that form 1:1 dimer structures comprised of three neighboring duplexes.<sup>26</sup> These flexible dimers exhibited a  $T_m$  increase of 12 °C, but with dehybridization profiles broad like those of unmodified DNA duplexes. Interestingly, the 5 °C  $T_m$  enhancement observed for the two neighboring duplexes in this double-clip experiment is about half of that for the three duplexes in the Shchepinov's dendrimer. These observations with cooperative yet flexible duplexes suggests that while multivalent interactions are responsible for enhanced melting temperature, the rigidity of our rSMDH system is imperative in forcing the connected DNA duplexes to remain in the parallel geometry and optimizing cooperative interactions via shared ion clouds.<sup>19</sup>

### 3.4. Triazole-linked rigid small molecule-DNA hybrids

#### 3.4.1. Introduction

In section 3.2, rigid small molecule-DNA hybrids (rSMDHs) were synthesized following a rather long and linear route to produce rSMDH<sub>3</sub>'s containing a tris(phenylacetylene) core with benzyl phosphate linkages to three DNA arms. The enhanced melting profiles observed for rSMDH<sub>3</sub>:rSMDH<sub>3</sub> dimers piqued our interest to investigate how the geometry, number, and spacing of DNA substituents around a central core can lead to sharp melting profiles. For such a purpose, a library of cores representing different combinations of these substituent variables is needed.

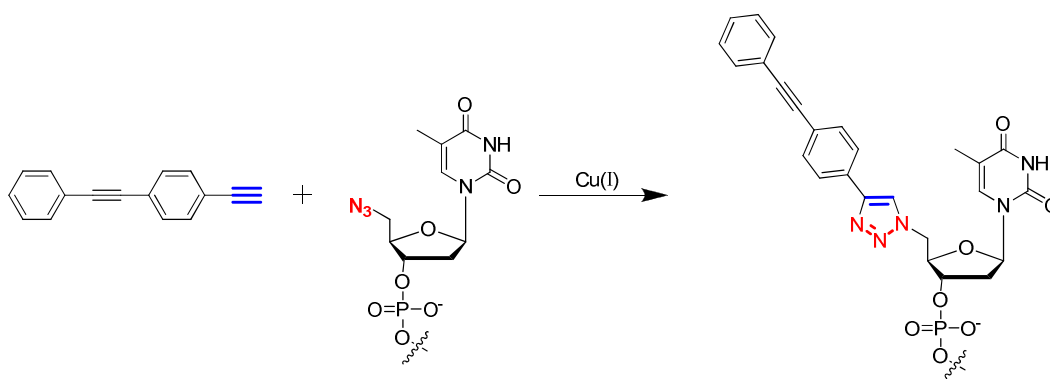
Unfortunately, the benzyl phosphate-linked design of the original rSMDHs was found to have several weaknesses that hindered its expansion into a library. Potential lability of the DNA substituents meant that these rSMDH may be unstable and unsuitable for in-depth studies. Additionally, the rSMDH core-synthesis was a multi-step process that complicated attempts at diversifying the core structure—any variation away from the original core would necessitate a complete reworking of the synthetic route. Thus, we focused on building a series of more stable rSMDH that can be made via a modular synthetic strategy using readily accessible synthons.

##### 3.4.1.1. Triazole-linked rSMDHs

To fulfill the aforementioned criteria, the synthesis described in this section replaces the presumably labile benzyl phosphate with a more stable triazole linkage formed through the addition of readily accessible azide-terminated DNAs to acetylene-terminated cores using “click” chemistry (Scheme 3.3).<sup>23</sup> The ease of manipulating the placement and number of terminal acetylene groups around a central phenyl core allows for a more flexible approach to the rSMDH synthesis. Such an approach will allow for the facile elaboration and management of the desired

core library and greatly streamline the process of elucidating the factors that affect the melting profiles of DNA aggregates.

**Scheme 3.3** Proposed triazole “click” chemistry linkage.



## 3.4.2. Results and discussion

### 3.4.2.1. Synthesis of core molecules

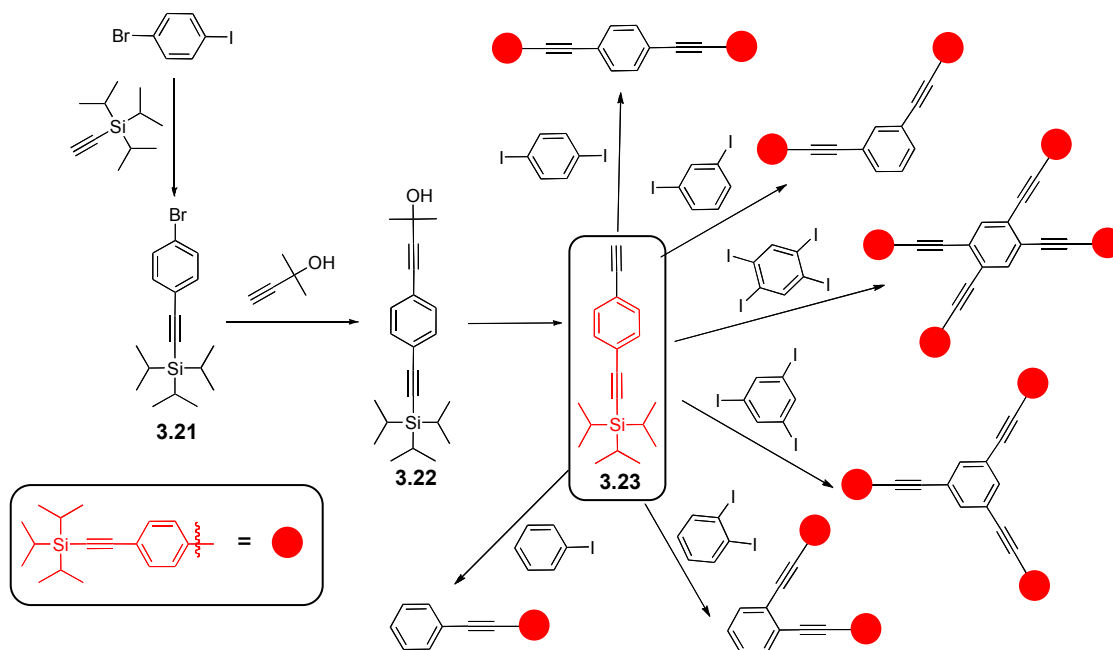
#### 3.4.2.1.1. Synthesis of acetylene arm 3.23

The first step of the modular “click” approach was to create an acetylene “arm” component, which could then be attached to various aryl halide cores to form a library of small molecules with precise control over the density and positioning of the DNA attachment sites (Scheme 3.4). The arm molecule **3.23** was synthesized in good yield from *p*-bromiodobenzene in a three-step reaction comprising two Sonogashira couplings (66% and 82% yield, respectively) and one selective deprotection step (96% yield). The lower yield in the first coupling results from a proclivity of the reactants towards bis-coupling despite the higher activity of iodine compared to bromine and controlled stoichiometries.

Compound **3.23** has good stability and a rigid phenylacetylene structure that will ensure the precise desirable geometry of the final DNA-attached product.<sup>30,31</sup> In addition, the triisopropylsilyl (TIPs) protecting group is easily removed after arm-attachment to various aryl-

halide cores (Scheme 3.4), thus opening the terminal acetylenes for the subsequent DNA attachment via “click” chemistry (*vide infra*).<sup>32,33,34</sup>

**Scheme 3.4** Proposed synthesis route of the desired core molecule library.



#### 3.4.2.1.2. Coupling to acetylene arm 3.23

Iodo-substituted benzenes were chosen as the core molecules for coupling to **3.23** since several attempts to couple to bromobenzene derivatives showed little to no reactivity. While the number of possible cores for this library can be chosen from a wide range of aromatic iodides, a partial list of which is shown in Scheme 3.4, we have currently synthesized the mono-, di-, and tri-substituted benzene derivatives shown in Figure 3.10 for initial studies. As expected, the coupling yield for the mono-substituted derivative **3.24** is the highest (65%), followed by *p*- (33%) and *m*-disubstituted (18%) derivatives **3.25** and **3.26**, and trisubstituted compound **3.27** (~10%). We note that the reported isolated yields for all of these derivatives are lower than commonly encountered in Sonogashira couplings, possibly due to the multiple-column

chromatographic purifications required to make them pure enough for the subsequent DNA coupling.

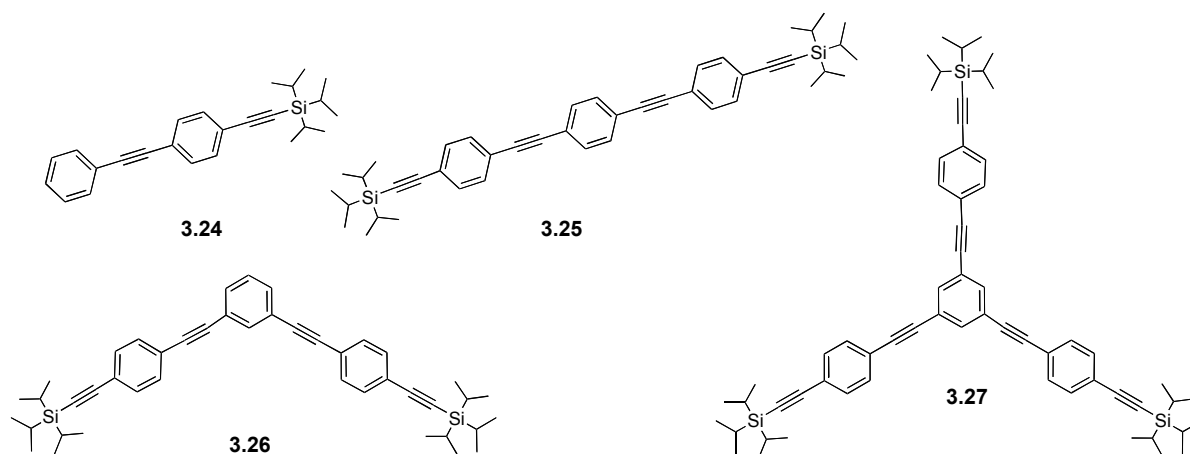


**Figure 3.10** Library of synthesized “click”-capable rSMDH core molecules possessing a range of substitution densities and spacing.

#### 3.4.2.2. DNA attachment

With derivatives **3.24-3.27** in hand, the next step is to synthesize DNA strands using solid-phase synthesis and convert the 5'-OH groups to 5'-N<sub>3</sub> groups directly on the solid support.<sup>35,36</sup> Under “click” conditions, treatment of the azide-converted DNA strands with the cores **3.24-3.27**, should result in attachment of the DNA strands to the acetylene ‘arms’ of the cores via triazole formation. This work is currently being continued in the Nguyen group.

#### 3.4.3. Conclusion and future work

To date, we have synthesized several complete “click”-capable core molecules. The next steps will be to synthesize short azide-substituted DNA strands on solid supports and attach them to the desired cores via a triazole linkages. The completed rSMDHs will then be used in a series of melting point assays to complement and extend our previous rSMDH work.



### 3.5. Experimental

#### 3.5.1. General procedures, materials, and instrumentation

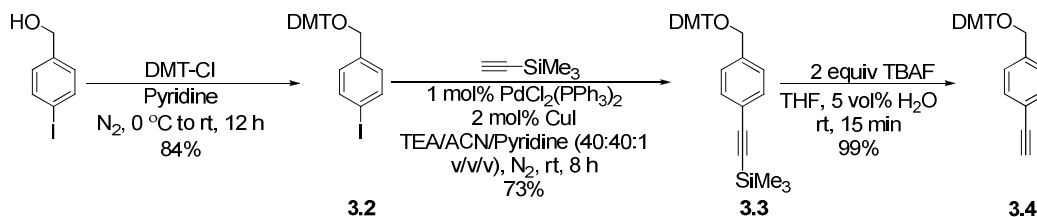
All air- and/or water-sensitive reactions were carried out under a dry nitrogen atmosphere using either standard Schlenk techniques or an inert-atmosphere glovebox, unless otherwise noted. All reagents and reagent-grade solvents were purchased from Acros Organics, Strem Chemicals, Inc., Aldrich Chemical Company, or Glen Research (Sterling, VA) and used as received. Deuterated solvents were purchased from Cambridge Isotope Laboratories and used without further purification. Dry solvents, with the exception of pyridine and triethylamine (TEA), were prepared by drying HPLC-grade solvents via a Dow-Grubbs solvent system.<sup>37</sup> Pyridine and triethylamine were dried over  $\text{CaH}_2$  and vacuum-transferred into a Strauss flask. All dry solvents were collected under inert gases, degassed under vacuum, and stored under nitrogen in a Strauss flask prior to use. Nanopure water (18.2  $\text{M}\Omega\text{-cm}$  resistivity) was obtained from a Milipore system (Milli-Q Biocel). Dialysis tubes (Spectra/Por Float-a-lyzer RC, 3-mL, MWCO = 8,000, 15,000, and 25,000) were purchased from Spectrum Laboratories (Rancho Dominguez, CA). All flash chromatography was carried out using a 56-mm inner diameter column containing 200-mm of silica gel under a positive pressure of lab air. Electrospray-ionization mass spectrometric (ESI-MS) data were obtained on an LCQ Advantage instrument equipped with an ion trap detector, using MeOH as the solvent with a flow rate of 0.2 mL/min.

$^1\text{H}$  and  $^{13}\text{C}$  NMR spectra were recorded on either a Varian Inova 500 FT-NMR spectrometer (499.8 MHz for  $^1\text{H}$ , 125.7 MHz for  $^{13}\text{C}$ ) or a Varian Mercury 400-FT-NMR (400 MHz for  $^1\text{H}$ , 100 MHz for  $^{13}\text{C}$ ) spectrophotometer.  $^1\text{H}$  NMR data are reported as follows: chemical shift (multiplicity (b = broad singlet, s = singlet, d = doublet, dd = doublet of doublets, t

= triplet, q = quartet, and m = multiplet), integration, and peak assignments).  $^1\text{H}$  and  $^{13}\text{C}$  chemical shifts are reported in ppm from TMS with the residual solvent resonances as internal standards.

Syntheses of DNA sequences were performed on an Expedite 8909 Nucleic Acid system. Unmodified DNA was purified on an Agilent 1100 HPLC equipped with a Varian Dynamax column (250 mm x 10.0 mm (L x ID), Microsorb 300-10 C18) using a gradient method beginning with 100 vol% 0.03M TEAA (TEAA = triethylammonium acetate) in nanopure water, and increasing to 48 vol% acetonitrile over 50 minutes, with a flow rate of 3 mL/min. Absorption spectra and melting analyses of DNA materials were recorded on a Varian Cary 300 Bio UV-Vis spectrophotometer using a Starna quartz cell (path length = 10 mm). Gel electrophoresis experiments were carried out on polyacrylamide gels using an Amersham Pharmacia EPS-601 power supply. Matrix-assisted laser desorption/ionization time-of-flight (MALDI-TOF) data was collected by the Mass Spectrometry Laboratory at the University of Illinois Urbana-Champaign using an Applied Biosystems Voyager-DE STR mass spectrometer. Estimations of duplex properties were performed using Oligo Calc: Oligonucleotide Properties Calculator.<sup>29</sup>

### 3.5.2. Synthesis



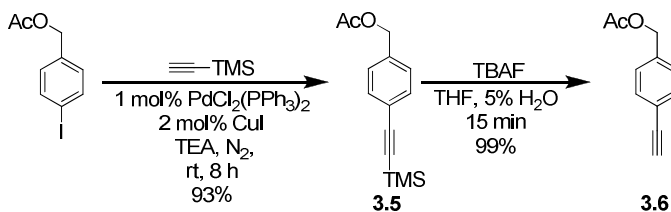
#### Synthesis of 1-(4',4''-dimethoxytrityloxymethyl)-4-iodobenzene (3.2). 4,4'

dimethoxytrityl chloride (DMT-Cl) (2.00 g, 5.90 mmol) was added to a solution of 4-iodobenzyl alcohol (1.38 g, 5.90 mmol) in anhydrous pyridine (50 mL) at 0°C. After allowing the reaction mixture to slowly rise to room temperature and stirring for 12 h, the reaction mixture was poured into saturated aqueous NaHCO<sub>3</sub> (100 mL) and the mixture was extracted with CH<sub>2</sub>Cl<sub>2</sub> (2 x 100 mL). After solvent removal under reduced pressure, the product was purified by silica-gel column chromatography using hexanes/ethyl acetate/triethylamine (70:29:1 v/v/v) as an eluent to yield the product as a light yellow gel (2.66 g, 84%). <sup>1</sup>H NMR (500 MHz, CD<sub>2</sub>Cl<sub>2</sub>): δ 3.78 (s, 6H, Ar-OCH<sub>3</sub>), 4.11 (s, 2H, CH<sub>2</sub>), 6.85 (d, 4H, Ar-H), 7.14 (d, 2H, Ar-H), 7.31 (m, 3H, Ar-H), 7.37 (d, 4H, Ar-H), 7.43 (d, 2H, Ar-H), 7.68 (d, 2H, Ar-H). <sup>13</sup>C NMR (500 MHz, CD<sub>2</sub>Cl<sub>2</sub>): δ 55.7 (OCH<sub>3</sub>), 66.4 (CH<sub>2</sub>), 87.1 (quaternary C), 92.7 (ArC-I), 113.5 (ArOCH<sub>3</sub>-C<sub>o</sub>), 127.3 (ArC), 128.4 (ArC), 128.5 (ArC), 129.5 (ArI-C<sub>m</sub>), 130.6 (ArC), 136.5 (ArC), 137.8 (ArI-C<sub>o</sub>), 139.6 (ArI-C<sub>p</sub>), 145.6 (ArC), 159.2 (ArC-OCH<sub>3</sub>).

**Synthesis of 1-(4',4''-dimethoxytrityloxymethyl)-4-(trimethylsilylethynyl)benzene (3.3).** In an inert-atmosphere glovebox, (trimethylsilyl)acetylene (0.18 g, 1.86 mmol) was added to a stirring suspension of **3.2** (0.50 g, 0.93 mmol), (PPh<sub>3</sub>)<sub>2</sub>PdCl<sub>2</sub> (6.5 mg, 9.0 μmol), and copper(I) iodide (3.5 mg, 18.0 μmol), in TEA/acetonitrile(ACN)/pyridine (10 mL:10 mL:0.25 mL). The resulting suspension was removed from the glovebox and stirred for 8 h at room

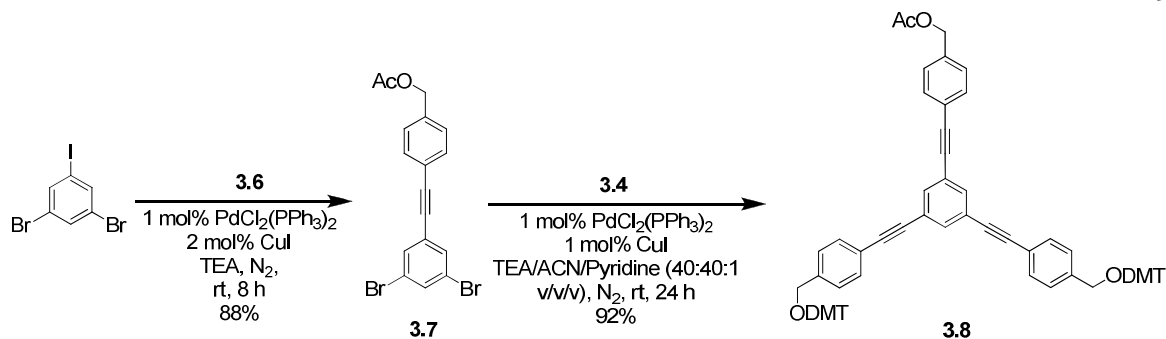
temperature before removal of the volatiles in vacuo. The product was purified by silica-gel column chromatography, using hexanes/triethylamine (80:20 v/v) as an eluent to yield the product as a yellow gel (0.345 g, 73%).  $^1\text{H}$  NMR (500 MHz,  $\text{CD}_2\text{Cl}_2$ ):  $\delta$  0.25 (s, 9H,  $\text{Si}(\text{CH}_3)_3$ ), 3.78 (s, 6H,  $\text{Ar-OCH}_3$ ), 4.16 (s, 2H,  $\text{CH}_2$ ), 6.84 (d, 4H,  $\text{Ar-H}$ ), 7.20 (d, 2H,  $\text{Ar-H}$ ), 7.31 (m, 3H,  $\text{Ar-H}$ ), 7.38 (d, 4H,  $\text{Ar-H}$ ), 7.42 (d, 2H,  $\text{Ar-H}$ ), 7.49 (d, 2H,  $\text{Ar-H}$ ).  $^{13}\text{C}$  NMR (500 MHz,  $\text{CD}_2\text{Cl}_2$ ):  $\delta$  0.2 ( $\text{Si}(\text{CH}_3)_3$ ), 55.8 ( $\text{OCH}_3$ ), 66.4, ( $\text{CH}_2$ ), 87.1 (quaternary C), 94.4 ( $\text{Si-alkyne C}$ ), 105.5 ( $\text{Ar-alkyne C}$ ), 113.5 ( $\text{ArOCH}_3\text{-C}_o$ ), 122.2 ( $\text{ArC-alkyne}$ ), 127.3 ( $\text{ArC}$ ), 128.2 ( $\text{alkyne-ArC}_m$ ), 128.4 ( $\text{ArC}$ ), 128.6 ( $\text{ArC}$ ), 130.6 ( $\text{ArC}$ ), 132.2 ( $\text{alkyne-ArC}_o$ ), 136.7 ( $\text{ArC}$ ), 140.5 ( $\text{alkyne-ArC}_p$ ), 145.7 ( $\text{ArC}$ ), 159.2 ( $\text{ArC-OCH}_3$ ).

**Deprotection of 3.3 to yield 1-(4',4''-dimethoxytrityloxymethyl)-4-ethynylbenzene (3.4).** Tetrabutylammonium fluoride (1.0 mL of a 1-M solution in tetrahydrofuran (THF), 1.0 mmol) was added to an open-air solution of **3.3** (0.20 g, 0.40 mmol) in stirring THF (5 mL). The solution was stirred at room temperature for 15 minutes, and the solvent was removed in vacuo to yield the product as a brown solid (0.169 g, 99%) which was used immediately in the synthesis of **3.8**.



**Synthesis of 4-(trimethylsilylethynyl)benzyl acetate (3.5).** In an inert-atmosphere glovebox, (trimethylsilyl)acetylene (0.267 g, 2.72 mmol) was added to a stirring suspension of 4-iodobenzyl acetate<sup>24</sup> (0.50 g, 1.81 mmol),  $(\text{PPh}_3)_2\text{PdCl}_2$  (12.7 mg, 0.02 mmol), and CuI (6.9 mg, 0.04 mmol) in dry triethylamine (30 mL). The resulting suspension was allowed to stir under nitrogen for 3 h at room temperature, and the volatiles were subsequently removed in vacuo. The remaining solid was dissolved in ethyl ether (30 mL); the resulting solution was gravity filtered and evaporated to dryness in vacuo. The crude product was purified by silica-gel column chromatography, using hexanes/ethyl acetate (70:30 v/v) as an eluent to yield the product as an orange solid (0.415 g, 93%).  $^1\text{H}$  NMR (500 MHz,  $\text{CD}_2\text{Cl}_2$ ):  $\delta$  0.25 (s, 9H,  $\text{Si}(\text{CH}_3)_3$ ), 2.08 (s, 3H,  $\text{ArCH}_2\text{OCOCH}_3$ ), 5.07 (s, 2H,  $\text{ArCH}_2\text{OCOCH}_3$ ), 7.30 (d, 2H, Ar-H), 7.44 (d, 2H, Ar-H).  $^{13}\text{C}$  NMR (500 MHz,  $\text{CD}_2\text{Cl}_2$ ):  $\delta$  0.1 ( $\text{Si}(\text{CH}_3)_3$ ), 21.3 ( $\text{ArCH}_2\text{OCOCH}_3$ ), 66.1 ( $\text{ArCH}_2\text{OCOCH}_3$ ), 95.1 (Si-alkyne C), 105.0 (Ar-alkyne C), 123.4 (alkyne-ArC), 128.4 (alkyne-ArC<sub>m</sub>), 132.5 (alkyne-ArC<sub>o</sub>), 137.3 (alkyne-ArC<sub>p</sub>), 171.1 ( $\text{ArCH}_2\text{OCOCH}_3$ ).

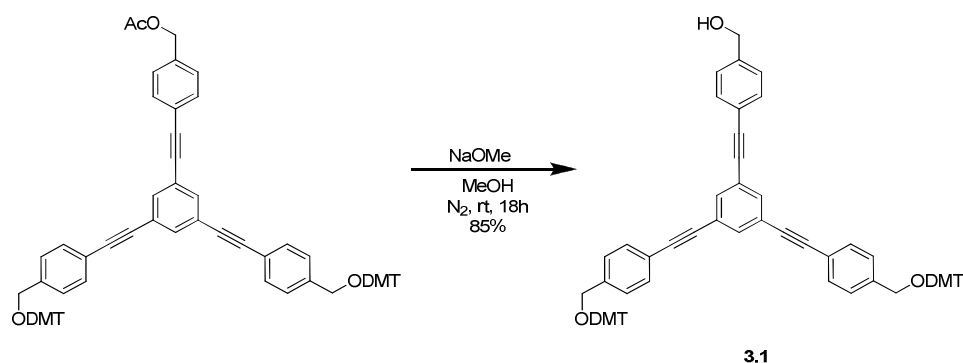
**Deprotection of 3.5 to yield 4-ethynylbenzyl acetate (3.6).** Tetrabutylammonium fluoride (TBAF) (2.0 mL of a 1-M solution in THF, 2.0 mmol) was added to an open-air solution of **3.5** (0.25 g, 1.01 mmol) in stirring THF (5 mL). The solution was stirred at room temperature for 15 minutes, and the solvent was removed by evaporation to yield the product as a brown solid (0.175 g, 99%) which was used immediately in the synthesis of **3.7**.



**Synthesis of 4-(3',5'-dibromo-phenylethynyl)-benzyl acetate (3.7).** In an inert-atmosphere glovebox, 1-iodo-3,5-dibromobenzene (0.235 g, 1.00 mmol) was added to a stirring suspension of **3.6** (0.175 g, 1.00 mmol), (PPh<sub>3</sub>)<sub>2</sub>PdCl<sub>2</sub> (7.0 mg, 0.01 mmol), and copper(I) iodide (3.8 mg, 0.02 mmol) in dry triethylamine (15 mL). The resulting suspension was allowed to stir under nitrogen for 8 h at room temperature, and the solvent was subsequently removed in vacuo. The remaining solid was dissolved in ethyl ether (30 mL); the resulting solution was gravity filtered and evaporated to dryness in vacuo. The product was purified by silica-gel column chromatography, using hexanes/ethyl acetate (70:30 v/v) as an eluent to yield the product as a white solid (0.361 g, 88%). <sup>1</sup>H NMR (500 MHz, CD<sub>2</sub>Cl<sub>2</sub>): δ 2.10 (s, 3H, ArCH<sub>2</sub>OCOCH<sub>3</sub>), 5.10 (s, 2H, ArCH<sub>2</sub>OCOCH<sub>3</sub>), 7.37 (d, 2H, Ar-H), 7.53 (d, 2H, Ar-H), 7.64 (s, 2H, Ar-H), 7.67 (s, 1H, Ar-H). <sup>13</sup>C NMR (500 MHz, CD<sub>2</sub>Cl<sub>2</sub>): δ 21.3 (ArCH<sub>2</sub>OCOCH<sub>3</sub>), 66.1 (ArCH<sub>2</sub>OCOCH<sub>3</sub>), 87.1 (Br<sub>2</sub>Ar-alkyne C), 91.9 (AcOAr-alkyne C), 122.4 (Br-ArC), 123.1 (AcOAr-C≡C), 127.1 (Br<sub>2</sub>ArC≡C), 128.6 (AcOArC<sub>m</sub>-alkyne), 132.4 (AcOArC<sub>o</sub>-alkyne), 133.5 (Br<sub>2</sub>ArC<sub>o</sub>-alkyne), 134.5 (Br<sub>2</sub>ArC<sub>o</sub>-alkyne), 137.8 (ArC<sub>p</sub>-alkyne), 171.1 (ArCH<sub>2</sub>OCOCH<sub>3</sub>).

**Synthesis of 1-[(4-acetoxymethyl)phenylethynyl]-3,5-bis-[4-(4',4''-dimethoxytrityloxy methyl)phenylethynyl]benzene (3.8).** In an inert-atmosphere glovebox, **3.7** (0.169 g, 0.39 mmol) was added to a stirring suspension of **3.4** (64 mg, 0.16 mmol),

(PPh<sub>3</sub>)<sub>2</sub>PdCl<sub>2</sub> (2.2 mg, 3.1 μmol), and copper(I) iodide (0.6 mg, 3.1 μmol), in TEA/ACN/pyridine (10 mL:10 mL:0.25 mL). The resulting suspension was stirred for 15 h at 50 °C and concentrated to dryness by evaporation under reduced pressure. The product was purified by silica-gel column chromatography, using hexanes/ethyl acetate/triethylamine (70:29:1 v/v/v) as an eluent to yield the product as a yellow solid (0.160 g, 92%). <sup>1</sup>H NMR (500 MHz, CD<sub>2</sub>Cl<sub>2</sub>): δ 2.11 (s, 3H, ArCH<sub>2</sub>OCOCH<sub>3</sub>), 3.79 (s, 12H, Ar-OCH<sub>3</sub>), 4.20 (s, 4H, CH<sub>2</sub>), 5.12 (s, 2H, ArCH<sub>2</sub>OCOCH<sub>3</sub>), 6.84 (d, 8H, Ar-H), 7.25 (d, 4H, Ar-H), 7.33 (m, 6H, Ar-H), 7.40 (m, 12H, Ar-H), 7.53 (m, 8H, Ar-H), 7.67 (s, 3H, Ar-H). <sup>13</sup>C NMR (500 MHz, CD<sub>2</sub>Cl<sub>2</sub>): δ 21.3 (ArCH<sub>2</sub>OCOCH<sub>3</sub>), 55.7 (OCH<sub>3</sub>), 66.1 (ArCH<sub>2</sub>OCOCH<sub>3</sub>), 66.4 (CH<sub>2</sub>), 87.1 (quaternary C), 88.0 (alkyne C), 88.6 (alkyne C), 90.6 (alkyne C), 91.1 (alkyne C), 113.7 (ArOCH<sub>3</sub>-Co), 118.1 (ArC), 121.7 (ArC), 123.0 (ArC), 124.7 (ArC) 127.5 (ArC), 128.4 (ArC), 128.6 (ArC), 130.5 (ArC), 132.1 (ArC), 132.3 (ArC), 133.8 (ArC), 134.5 (ArC), 136.7 (ArC), 137.5 (ArC), 140.5 (ArC), 145.7 (ArC), 159.2 (ArC-OCH<sub>3</sub>), 171.1 (ArCH<sub>2</sub>OCOCH<sub>3</sub>).



**Synthesis of 1-[(4-hydroxymethyl)phenylethynyl]-3,5-bis-[4-(4',4''-dimethoxytrityloxy methyl)phenylethynyl]benzene.** In an inert-atmosphere glovebox, sodium metal (5.2 mg, 0.22 mmol) was dissolved in dry methanol (MeOH, 5 mL) and the ensuing NaOMe mixture was quickly added to a stirring solution of **3.8** (0.125 g, 0.11 mmol) in MeOH

(5 mL). The resulting mixture was quickly capped to prevent evaporation and allowed to stir under nitrogen overnight. Upon completion of the reaction, the reaction mixture was removed from the glove box, the methanol was removed using a rotary evaporator, and the resulting residue was dissolved in 1-butanol (20 mL) before being washed with deionized water (3 x 30 mL). The collected organic layer was dried over anhydrous sodium sulfate and evaporated in vacuo. The resulting crude solid was purified by column chromatography using hexanes/ethyl acetate/triethylamine (50:40:10 v/v/v) as the eluent, yielding the product as a light-yellow solid (0.102 g, 85%).  $^1\text{H}$  NMR (500 MHz,  $\text{CD}_2\text{Cl}_2$ ):  $\delta$  3.80 (s, 12H, Ar-OCH<sub>3</sub>), 4.21 (s, 4H, CH<sub>2</sub>), 4.71 (s, 2H, ArCH<sub>2</sub>OCOCH<sub>3</sub>), 6.87 (d, 8H, Ar-H), 7.25 (d, 4H, Ar-H), 7.33 (m, 6H, Ar-H), 7.41 (m, 12H, Ar-H), 7.55 (m, 8H, Ar-H), 7.62 (s, 3H, Ar-H).  $^{13}\text{C}$  NMR (500 MHz,  $\text{CD}_2\text{Cl}_2$ ):  $\delta$  55.7 (OCH<sub>3</sub>), 64.7 (ArCH<sub>2</sub>OCOCH<sub>3</sub>), 65.7 (CH<sub>2</sub>), 87.1 (quaternary C), 88.1 (alkyne C), 91.1 (alkyne C), 91.2 (alkyne C), 113.7 (ArOCH<sub>3</sub>-C<sub>O</sub>), 121.8 (ArC), 122.0(ArC), 124.7 (ArC), 127.3 (ArC), 127.4 (ArC), 127.5 (ArC), 128.5 (ArC), 128.6 (ArC), 130.6 (ArC), 132.2 (ArC), 132.3 (ArC), 134.4 (ArC), 136.6 (ArC), 140.8 (ArC), 143.1 (Ar C), 145.7 (ArC), 159.2 (ArC-OCH<sub>3</sub>).

**Synthesis of unmodified DNA sequences A and B.** Using standard procedures and reagents, sequences **A** and **B** (5'-TTATAACTATTCCTA-3' and 3'-AATATTGATAAGGAT-5') were synthesized, purified, and subsequently used in melting studies

**Synthesis of rSMDH<sub>3</sub>-A.** Controlled porosity glass (CPG) beads possessing 1  $\mu\text{mole}$  of thymidine attached to the surface via the 5' terminus (Glen Research, dT-5'-CPG, catalog #20-0302-01) were placed in a 1- $\mu\text{mole}$  synthesis column. 5'-phosphoramidites (Glen Research, dA-5'-CE phosphoramidite, catalog #10-0001-02, dC-5'-CE phosphoramidite, catalog #10-0101-02, dG-5'-CE phosphoramidite, catalog #10-0201-02, dT-5'-CE phosphoramidite, catalog #10-0301-



02) were then added using the standard protocol on an Expedite 8909 synthesizer to prepare the CPG-5'-TTATAACTATTCCTATTTTTT-3' sequence (sequence **A** with a T<sub>6</sub> spacer). Following deprotection of the final DMT group, the synthesis column was brought into an inert-atmosphere glovebox and treated with a solution containing CH<sub>2</sub>Cl<sub>2</sub> (0.5 mL), *N,N*-diisopropylethylamine (0.1 mL), and 2-cyanoethyl-*N,N*-diisopropylchlorophosphoramidite (0.025 g) for 30 minutes, resulting in a phosphoramidite-terminated CPG-supported strand. The column was then rinsed with CH<sub>2</sub>Cl<sub>2</sub> (3 × 1 mL) and treated with a solution containing CH<sub>2</sub>Cl<sub>2</sub> (0.5 mL), **3.1** (10 mg), and tetrazole (0.5 mL of a 1-M solution in acetonitrile) for 15 minutes, resulting in a CPG-supported strand modified with **1**. After rinsing with CH<sub>2</sub>Cl<sub>2</sub> (3 × 1 mL) and acetonitrile (3 × 1 mL), the column was returned to the Expedite 8909 synthesizer, oxidized, and capped. Step-wise, the sequence: 3'-TTTTTTATCCTTATCAATATT-5' (sequence **A** with a T<sub>6</sub> spacer) was then added to the existing CPG-supported sequence using standard 3'-phosphoramidite chemistry to yield the target rSMDH<sub>3</sub> with three strands of sequence **A** attached.

**Synthesis of rSMDH<sub>3</sub>-B.** Using the method shown above for rSMDH<sub>3</sub>-**A**, 3'-TTTTTTAATATTGATAAGGAT-5' (sequence **B** with a T<sub>6</sub> spacer) was triply added to **3.1**.

**Purification of rSMDH<sub>3</sub>-A and rSMDH<sub>3</sub>-B.** CPG beads containing the rSMDH<sub>3</sub> materials were placed in concentrated ammonium hydroxide at room temperature for 8 h to cleave the rSMDHs from the solid supports. Afterwards, ammonium hydroxide was removed by passing a stream of N<sub>2</sub> over the beads. The remaining rSMDH<sub>3</sub>'s were extracted into nanopure H<sub>2</sub>O (1 mL), filtered, and brought up to 3 mL with PBS buffer (pH 7.0, 0.15 M NaCl), added to an 8-K MWCO dialysis tube, and dialyzed against PBS buffer (500 mL) for 14 h with the buffer exchanged every 2 h and then 10 h for the last dialysis. The rSMDH<sub>3</sub> solution was analyzed by

denaturing PAGE (20% acrylamide) to determine approximate purity. The dialysis procedure was followed for the 15-K and 25-K MWCO tubes until the rSMDH<sub>3</sub> solutions were at least 90% pure by PAGE analysis (Figure 3.11). MALDI-TOF:  $m/z = 19,617.2$  for rSMDH<sub>3</sub>-A (Calcd 19,804.6) (Figure 3.12);  $m/z = 20,211.4$  for rSMDH<sub>3</sub>-B (Calcd 20,218.9).

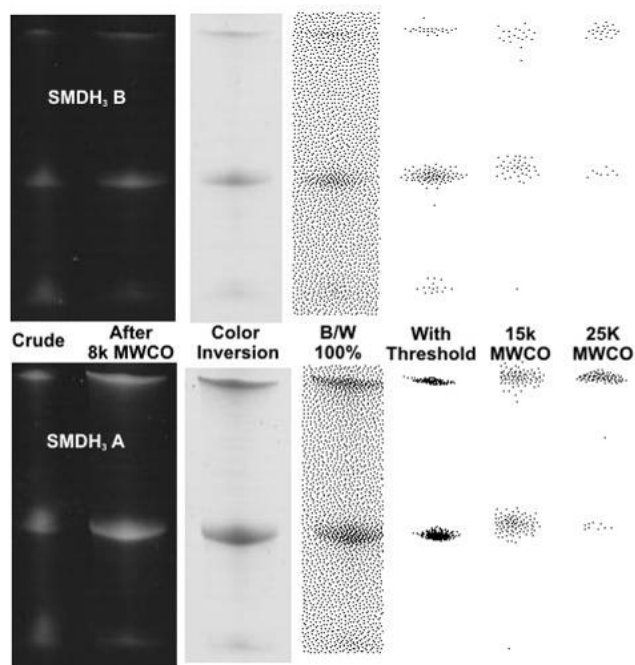


**Figure 3.11.** Digital images of denaturing PAGE gels following the purification of rSMDH<sub>3</sub> materials after successive dialysis runs. Top row: rSMDH<sub>3</sub>-B; Bottom row: rSMDH<sub>3</sub>-A. Column 1: Unmodified image of crude rSMDH<sub>3</sub> products. Column 2: Unmodified image of rSMDH<sub>3</sub>'s after dialyzing through 8-K MWCO tubes. Column 3: Grayscale-inversion image of rSMDH<sub>3</sub> after dialyzing through 8-K MWCO tubes. Column 4: Black-and-white conversion image of rSMDH<sub>3</sub> after dialyzing through 8-K MWCO tubes. Column 5: Modified image (with background subtracted from black-and-white conversion image) of rSMDH<sub>3</sub> after dialyzing through 8-K MWCO tubes. Column 6: Modified image after dialyzing through 15-K MWCO tubes. Column 7: Modified image after dialyzing through 25-K MWCO tubes.

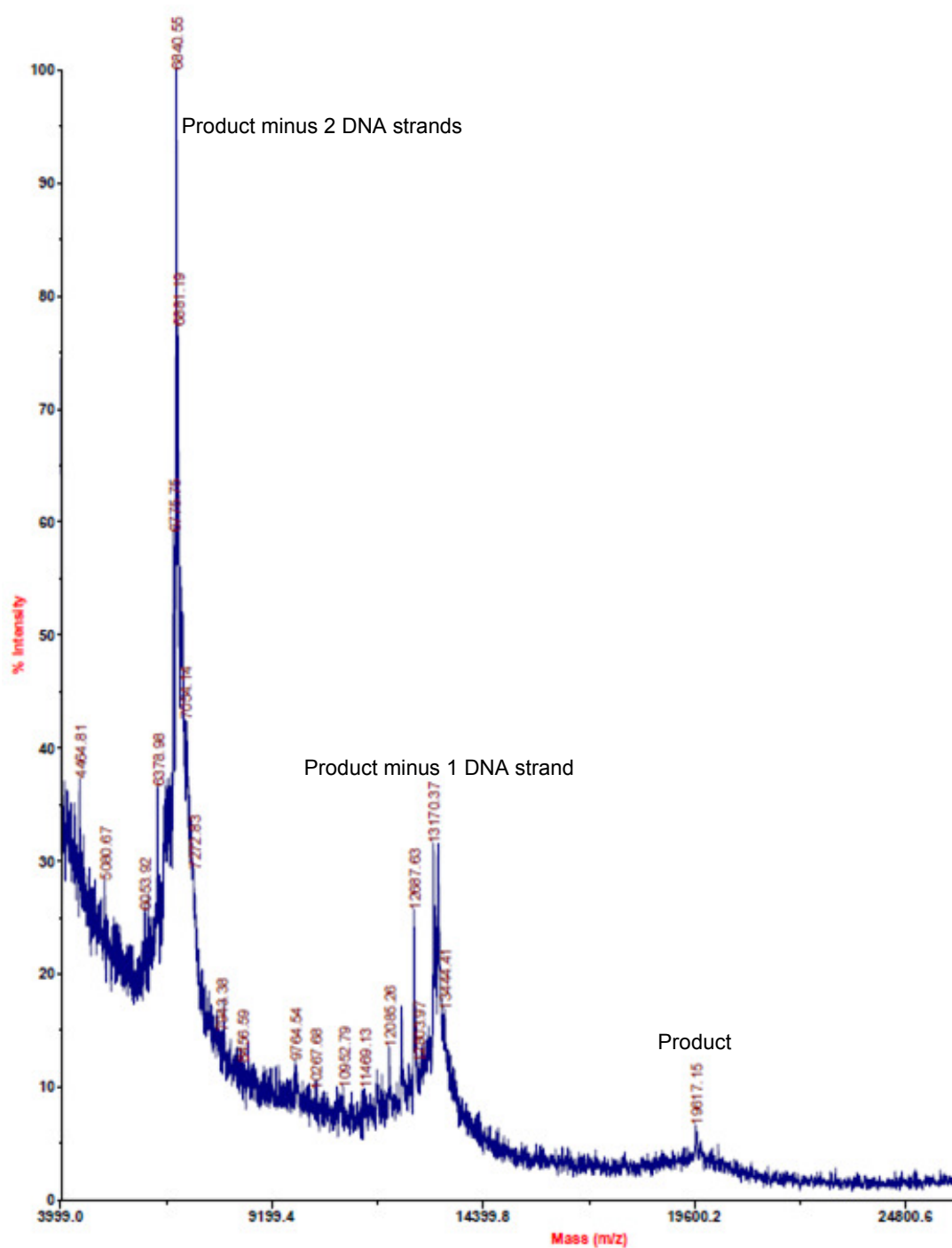


**Figure 3.12.** MALDI-TOF mass spectrum of purified rSMHD<sub>3</sub>-A, showing product peak and two major fragmentations peaks due to loss of 1 or 2 DNA strands.

**Synthesis of DNA sequences 3.9 through 3.20.** With the exception of those requiring the PEG-functionalized phosphoramidites (PEG<sub>3</sub> and PEG<sub>6</sub>) all sequences were synthesized on an Expedite 8909 synthesizer using unmodified procedures and reagents, and subsequently purified by HPLC. For sequences containing either (PEG<sub>3</sub> and PEG<sub>6</sub>), a solution of the appropriate PEG-functionalized phosphoramidite was placed in a spare reagent position on the Expedite 8909, and the sequences were synthesized and purified as normal.

**Synthesis of 1-bromo-4-[(triisopropylsilyl)ethynyl]benzene (3.21).** Under a nitrogen atmosphere, triisopropylsilylacetylene (2.24 g, 12.7 mmol) was added to a 50-mL Schlenk flask containing 1-bromo-4-iodobenzene (3.00 g, 10.6 mmol), (PPh<sub>3</sub>)<sub>2</sub>PdCl<sub>2</sub> (0.149 g, 0.212 mmol), CuI (0.019 g, 0.212 mmol), and triethylamine (TEA, 20 mL). The reaction mixture was allowed to stir under nitrogen overnight before being evaporated to dryness. The resulting precipitate was extracted with hexanes and the combined organics were evaporated to dryness. After solvent removal, the isolated product appeared as a reddish-brown oil (2.36 g, 6.98 mmol, 66%). <sup>1</sup>H NMR (400 MHz, CDCl<sub>3</sub>): δ 7.40 (d, 2H), 7.20 (d, 2H), 1.05 (s, 21H); the □ethane protons of the TiPS group were not observed, consistent with literature observations.<sup>32</sup>

**Synthesis of 2-methyl-4-*p*-[(triisopropylsilyl)ethynyl]phenylbut-3-yn-2-ol (3.22).** Under a nitrogen atmosphere, 3-hydroxy-3-methylbutyne (1.31 g, 15.6 mmol) was added to a 50-mL Schlenk flask containing **3.21** (1.76 g, 5.20 mmol), (PPh<sub>3</sub>)<sub>2</sub>PdCl<sub>2</sub> (0.073 g, 0.104 mmol), CuI (0.019 g, 0.210 mmol), and TEA (20 mL). The reaction mixture was refluxed under nitrogen overnight. Upon cooling to room temperature, a dark brown precipitate appeared in the reaction mixture. The reaction mixture was evaporated to dryness using a rotary evaporator, leaving behind a dark brown oil. Enough diethyl ether was then added to dissolve the oil, the reaction

was gravity filtered, and the filtrate was evaporated to dryness using a rotary evaporator. The remaining residue was dissolved in a mixture of pentane:ethyl acetate (9/1 v/v) and purified using silica gel chromatography (8 mm diameter x 10 cm length) and a mixture of pentane:ethyl acetate (9/1 v/v) as the eluent. After solvent removal, the isolated product appeared as a yellow oil (1.46 g, 4.29 mmol, 82%).  $^1\text{H}$  NMR (400 MHz,  $\text{CDCl}_3$ ):  $\delta$  7.42 (d, 2H), 7.39 (d, 2H), 1.63 (s, 6H), 2.05 (s, 1H), 1.13 (s, 21H); the methine protons of the TiPS group were not observed, consistent with literature observations.<sup>32</sup>

**Synthesis of 1-ethynyl-4-[(triisopropylsilyl)ethynyl]benzene (3.23).** Under nitrogen, solid NaOH (2.70 mg, 0.059 mmol), was added to a solution of **3.22** (0.100 g, 0.294 mmol) in dry toluene (15 mL). The resulting mixture was then refluxed under nitrogen overnight before being cooled to room temperature and evaporated to dryness *in vacuo*. The remaining crude product was then dissolved in diethyl ether and washed with 0.01 M HCl; the organic layer was removed, dried over  $\text{MgSO}_4$ , and evaporated to dryness *in vacuo*. The resulting dark brown oil was dissolved in a minimum amount of hexanes:ethyl acetate (4/1 v/v) and purified by silica gel chromatography (8 mm diameter x 4 cm length) using hexanes:ethyl acetate (4/1 v/v) as the eluent. After solvent removal, the isolated product appeared as a yellow oil (0.081 g, 0.287 mmol, 96%).  $^1\text{H}$  NMR (400 MHz,  $\text{CDCl}_3$ ):  $\delta$  7.43 (s, 1H), 7.41 (d, 2H), 7.39 (d, 2H), 1.13 (s, 21H); the methine protons of the TiPS group were not observed, consistent with literature observations.<sup>32</sup>

**Synthesis of 1-(triisopropylsilyl)ethynyl-4-(phenylethynyl)benzene 3.24.** In an inert atmosphere glovebox, precursor **3.23** (0.080 g, 0.284 mmol) was added to a 50-mL Schlenk flask containing iodobenzene (0.089 g, 0.567 mmol), CuI (0.020 g, 0.028 mmol),  $(\text{PPh}_3)_2\text{PdCl}_2$  (2.60

mg, 0.028 mmol), and TEA (15 mL). Immediately upon addition of precursor **3.23**, a white precipitate formed in the solution. After stirring under nitrogen overnight, the reaction mixture was diluted with excess ethyl ether (20 mL), washed with aqueous HCl (1 N, 20 mL), dried over MgSO<sub>4</sub>, and gravity filtered. The collected organic solvent was then evaporated to dryness, the residue redissolved in toluene, and evaporated to dryness on a rotary evaporator under heating to ensure the removal of all volatiles. The crude product was then redissolved in a minimum amount of methylene chloride and passed through a silica gel column (8 mm diameter x 5 cm length) using methylene chloride as the eluent. After solvent removal, the isolated product appeared as a brown solid (0.101 g, 0.282 mmol, 65%). <sup>1</sup>H NMR (500 MHz, CDCl<sub>3</sub>): δ 7.55 (t, 2H), 7.45 (t, 4H), 7.36 (d, 2H), 7.27 (s, 1H), 1.13 (s, 21H) the methine protons of the TiPS group were not observed, consistent with literature observations.<sup>32</sup>

**Synthesis of 1,4-bis({4'-[(triisopropylsilyl)ethynyl]phenyl}ethynyl)benzene 3.25.** In an inert atmosphere glovebox, precursor **3.23** (0.280 g, 0.992 mmol) was added to a 50-mL Schlenk flask containing 1,3-diiodobenzene (0.148 g, 0.451 mmol), CuI (0.016 g, 22.5 μmol), (PPh<sub>3</sub>)<sub>2</sub>PdCl<sub>2</sub> (0.002 g, 22.5 μmol), and TEA (20 mL). The resulting reaction mixture was then left stirring under nitrogen overnight. Analysis of the reaction mixture by TLC (hexanes:ethyl acetate 95/5 v/v) suggested that the reaction had run to completion. The reaction mixture was diluted with excess ethyl ether (20 mL), washed with aqueous HCl (1 N, 20 mL), dried over MgSO<sub>4</sub>, and gravity filtered. The resulting crude product was heated to 50 °C and left under vacuum overnight to ensure solvent removal. The mixture was then redissolved in a minimum amount of hexanes, and passed through a silica gel column (8 mm diameter x 10 cm length) using hexanes as an eluent. After solvent removal, the isolated product was repurified under the

same chromatographic conditions to afford the pure product as a white gel (0.051 g, 0.079 mmol, 18%).  $^1\text{H}$  NMR (500 MHz,  $\text{CDCl}_3$ ):  $\delta$  7.53 (t, 1H), 7.48 (d, 4H), 7.45 (s, 4H), 7.39 (d, 2H), 7.26 (s, 1H), 0.26 (s, 42H); the methine protons of the TiPS group were not observed, consistent with literature observations.<sup>32</sup>

**Synthesis of 1,3-bis({4'-[(triisopropylsilyl)ethynyl]phenyl}ethynyl)benzene 3.26.** In an inert atmosphere glovebox, **3.23** (0.44 g, 1.56 mmol) was added to a 5-mL vial containing 1,4-diiodobenzene (0.230 g, 0.700 mmol),  $(\text{PPh}_3)_2\text{PdCl}_2$  (0.060 g, 0.080 mmol), CuI (0.008 g, 0.080 mmol),  $\text{PPh}_3$  (0.023 g, 0.080 mmol), and TEA (5 mL). The reaction mixture was then microwave-irradiated (Biotage Initiator, regular solvent absorption setting) for 4 h at 100 °C. After cooling to room temperature, the reaction mixture was diluted with excess ethyl ether (20 mL) and filtered through a Buchner funnel. The filtrate was evaporated to dryness, redissolved in a minimum amount of hexanes, and purified by silica gel chromatography (8 mm diameter x 10 cm length) with hexanes as the eluent. After solvent removal, the isolated product was repurified under the same chromatographic conditions to afford the pure product as white crystals (0.110 g, 0.234 mmol, 33%).  $^1\text{H}$  NMR (400 MHz,  $\text{CDCl}_3$ ):  $\delta$  7.49 (d, 4H), 7.45 (s, 4H), 7.39 (d, 4H), 0.26 (s, 42H); the methine protons of the TiPS group were not observed, consistent with literature observations.<sup>32</sup>

**Synthesis of 1,3,5-tris({4'-[(triisopropylsilyl)ethynyl]phenyl}ethynyl)benzene 3.27.** In an inert atmosphere glovebox, precursor **3.23** (0.269 g, 0.950 mmol) was added to a 50-mL Schlenk flask containing 1,3,5-triiodobenzene (0.108 g, 0.238 mmol), CuI (0.011 g, 0.0119 mmol),  $(\text{PPh}_3)_2\text{PdCl}_2$  (0.0083 g, 0.0119 mmol), and TEA (20 mL). The resulting reaction mixture was then left stirring under nitrogen overnight. Analysis of the reaction mixture by TLC

(hexanes:ethyl acetate 95/5 v/v) suggested that the reaction had run to completion. The reaction mixture was then diluted with excess ethyl ether (20 mL), washed with aqueous HCl (1 N, 20 mL), dried over MgSO<sub>4</sub>, and gravity filtered. The resulting crude product was then redissolved in a minimum amount of hexanes, and passed through a silica gel column (2 cm diameter x 10 cm length) using hexanes as an eluent. After solvent removal, the isolated product was repurified under the same chromatographic conditions to afford a white crystalline material (~10%). <sup>1</sup>H NMR ((500 MHz, CDCl<sub>3</sub>): δ 7.48 (d, 4H), 7.47 (d, 4H), 7.45 (d, 4H), 7.38 (s, 3H), 0.26 (s, 63H)); the methine protons of the TiPS group were not observed, consistent with literature observations.<sup>32</sup>

### 3.5.3. Melting experiments (Section 3.2)

Hybridization mixtures of rSMDH<sub>3</sub>'s and unmodified DNA were formed by combining equimolar amounts of two complementary DNA species in PBS buffer at 50 °C, annealing the resulting mixture at 50 °C for 5 minutes, and allowing the solution to cool to room temperature over 8 h at room temperature. Aggregates were denatured by heating the samples from 15 °C to 70 °C at a rate of 1 °C per minute while monitoring the UV-vis absorbance at 260 nm at 0.1-°C intervals to determine the melting progress (Table 3.1). The van't Hoff enthalpy ( $\Delta H_{VH}$ ) was determined using the Varian Thermal Application software (version 3.0(182), Varian Australia Pty., Ltd.).

### 3.5.4. Demonstration of rSMDH<sub>3</sub> dimer formation by PAGE analysis

Using non-denaturing PAGE (10% polyacrylamide) ran at 4 °C, solutions containing high-concentration rSMDH<sub>3</sub> aggregates and low-concentration rSMDH<sub>3</sub> caged dimers were compared to purified rSMDH<sub>3</sub>-A and crude rSMDH<sub>3</sub>-A (vide supra, Figure 3.5), with all samples



containing ethidium bromide (10 vol% of a 1-mg/L solution). Converting the digital grayscale images to black-and-white allows for the estimation of the percent of each species. The intense spot seen for the low-concentration sample corresponds to 99% of the total signal, while the same region of the ‘streak’ seen for the concentrated sample corresponds only 49% of the sample.

### 3.5.5. Determining the number of cooperative duplexes $N_c$ for rSMDH<sub>3</sub> aggregates

From the slope ( $s$ ) of the melting temperature ( $T_m$ ) of unmodified DNA vs the natural log of salt concentration (Table 3.3, entries 1-6), the number of dissociated cations ( $n$ ) can be determined using Equation 3.1.<sup>16,18</sup>

$$s = \frac{nRT_m^2}{\Delta H_{VH}} \quad (3.1)$$

Solving for  $n$  using the  $T_m$  and the  $\Delta H_{VH}$  for each DNA:DNA mixture affords the number of dissociated cations per duplex. Equation 3.2 can now be used to find the number of cooperative duplexes ( $N_c$ ) for each of the rSMDH<sub>3</sub> mixtures (Table 3.3, entries 7-12).

$$s = \frac{N_c nRT_m^2}{\Delta H_{VH}} \quad (3.2)$$

**Table 3.3.** Melting data for unmodified DNA (DNA:DNA) duplexes and rSMDH<sub>3</sub> (rSMDH<sub>3</sub>:rSMDH<sub>3</sub>) aggregates.

Entry	Aggregate	[DNA] ( $\mu\text{M}$ )	[NaCl] (M) <sup>a</sup>	$T_m$ ( $^{\circ}\text{C}$ )	$\Delta H_{VH}$ (kJ)	$n$	$N_c$
1	DNA:DNA	3.80	0.08	39.8	427.1	3.91	–
2	DNA:DNA	3.80	0.15	44.1	416.4	3.71	–
3	DNA:DNA	3.80	0.30	50.1	433.2	3.71	–
4	DNA:DNA	0.38	0.08	33.8	377.5	3.25	–
5	DNA:DNA	0.38	0.15	39.2	410.7	3.42	–
6	DNA:DNA	0.38	0.30	43.2	400.6	3.25	–
7	rSMDH <sub>3</sub> :rSMDH <sub>3</sub>	3.80	0.08	37.5	325.2	–	0.86
8	rSMDH <sub>3</sub> :rSMDH <sub>3</sub>	3.80	0.15	41.5	357.5	–	0.97
9	rSMDH <sub>3</sub> :rSMDH <sub>3</sub>	3.80	0.30	49.0	345.3	–	0.89
10	rSMDH <sub>3</sub> :rSMDH <sub>3</sub>	0.38	0.08	43.2	850.8	–	2.90
11	rSMDH <sub>3</sub> :rSMDH <sub>3</sub>	0.38	0.15	51.5	868.4	–	2.68
12	rSMDH <sub>3</sub> :rSMDH <sub>3</sub>	0.38	0.30	56.0	1054	–	3.33

<sup>a</sup> NaCl concentration in a 10mM PBS buffer at 7.0 pH.

### 3.5.6. Melting experiments for Section 3.3

Each component was added to 1 mL of buffer (10 mM PBS, 0.15 M NaCl, 7.0 pH) in an equimolar ratio such that the total DNA concentration was 3.6  $\mu\text{M}$ , and heated to 90  $^{\circ}\text{C}$ . After cooling to room temperature over 8 h, the melting profile of the hybridized mixture was ascertained by heating the samples from 15  $^{\circ}\text{C}$  to 90  $^{\circ}\text{C}$  at a rate of 1  $^{\circ}\text{C}$  per minute while monitoring the increase in UV-vis absorbance at 260 nm at 0.1- $^{\circ}\text{C}$  intervals

## Chapter 4

### **Terthiophene-Based Polymer Nanoparticle Probes for DNA Detection**

Portions of this chapter appear in the following manuscript:

Stepp, B. R.; Boyle, M. M.; Srinivasan, S. R.; Nguyen, S. T. *Adv. Mater.* **2009**, to be submitted.

#### 4.1. DNA detection and signal amplification

DNA detection is an important area in modern research due to its broad utility in clinical diagnostics and forensics. As genetic diseases are caused by mutations in the genetic code, the ability to detect specific mutated sequences in a patient's genes can tell physicians if that person is prone to certain diseases. In addition, early detection of the presence of foreign genetic material in patients would alert doctors to pathogenic infections and allow for proactive treatments. DNA-based forensic studies could also be quickened by the use of a highly sensitive detection assay. In all of the aforementioned applications, the indicative target strands often exist only in trace amounts in a patient's blood sample and must be amplified before they can be reliably detected. As such, the last three decades have witnessed several innovations aimed at detecting oligonucleotides in low concentrations.<sup>1-5</sup>

To detect a DNA strand, the molecular recognition event between this target strand and a probe must be paired up with a signaling event that can be recognized by a macroscopic instrument. If the signaling mechanism is based on a molecular probe (Figure 4.1), each successful binding event leads only to a single-molecule-based signal, which would be difficult to assay in conventional settings. While recent innovations for detecting DNA have successfully coupled DNA-modified gold<sup>6</sup> and magnetic nanoparticles<sup>5</sup> to amplification processes, they necessitate extra modification steps. In this sense, a probe that possesses an intrinsically amplified signal should allow elimination of such modifications and greatly enhance DNA detection. This chapter describes our attempt to make such a probe from amphiphilic block copolymers.

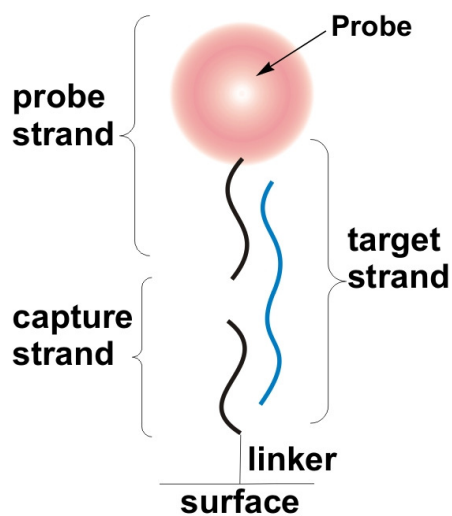


**Figure 4.1.** A typical DNA detection sandwich assay where a fully complimentary DNA duplex is formed when a surface-bound capture strand recruits a target strand to the surface, which then engages a probe-linked strand. A subsequent signaling event will allow a macroscale readout of this detection process; however, when the probe is a molecular entity each detection event will yield only a single-molecule-based signal.

## **4.2. Assembly of fluorescent/electrochemically active terthiophene-containing amphiphilic polynorbornenes into labeled polymer nanoparticles**

### **4.2.1. Introduction**

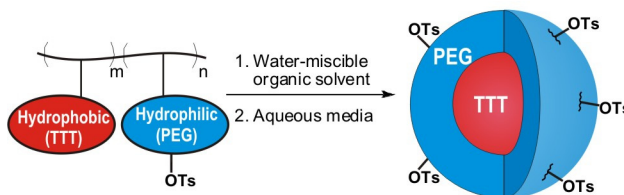
In recent years, “smart” nanoscale structures with a “functional payload” sequestered inside the core and a surface that can be modified with targeting groups have emerged as versatile platforms for the development of many biomedical applications.<sup>7-11</sup> Among the strategies that have been demonstrated for the deployment of such architectures, the self-assembly of amphiphilic block copolymers possessing functional side chains on each block is an attractive bottom-up method for synthesizing functional core-shell polymer nanoparticles (PNPs). In this fashion, we hypothesize that amphiphilic block copolymers comprising a hydrophobic block of the fluorescent/electrochemically active **ROMP-poly1** (described in chapter 2) and a hydrophilic block that allows for efficient, selective DNA functionalization (as elucidated in chapter 3) should facilitate the formation of PNP probes that are highly selective and intrinsically amplified.

#### **4.2.1.1. Eisenberg strategy for the synthesis of PNPs from amphiphilic block copolymers**

In the Eisenberg strategy for PNP formation in water, the amphiphilic block copolymer is first dissolved in a non-selective, water-miscible solvent, followed by the slow addition of a water, which is selective towards one of the blocks, inducing a microphase separation that results in a colloidal suspension of core-shell PNPs.<sup>12</sup> The hydrophilic block acts as a shell surrounding the hydrophobic core, protecting it as well as lending water solubility to the whole particle. In water, PNPs will start to form at a volume percentage of water known as the critical water content (CWC). The CWC of amphiphilic block copolymers with long hydrophobic blocks dissolved in either *N,N*-dimethylformamide (DMF) or dimethyl sulfoxide (DMSO) is typically

very low (3-5 vol% H<sub>2</sub>O),<sup>13,14</sup> leading to stable, kinetically locked<sup>15</sup> PNPs without the need for cross-linking (Scheme 4.1).

**Scheme 4.1.** The Eisenberg strategy for inducing the self-assembly of an amphiphilic block copolymer into a polymer nanoparticle.



#### 4.2.1.2. Payload-containing PNPs

In our modification of the Eisenberg strategy, one portion of the block copolymers is comprised of hydrophobic payload molecules that will assemble into a core in the presence of aqueous media.<sup>14</sup> The hydrophilic block can be further engineered to display a good leaving group at the surface of the PNP to facilitate additional modification with targeting moieties or other functionalities.<sup>16</sup> When targeted, a 200-nm-diameter PNP PNPs can carry up to  $10^7$  payload molecules,<sup>17</sup> delivering a surprisingly high number of active molecules per recognition event. Unlike other delivery vehicles where the payload is non-covalently sequestered inside a shell, linking the payload covalently to the polymer backbone eliminates the loading step; leaking of payload molecules from the core is not an issue. We have reported PNPs made with norbornene-based block copolymers containing very hydrophobic payload molecules such as indomethacin (CWC = 3-4 vol% in DMSO)<sup>14</sup> and doxorubicin (CWC = 5-8 vol% in DMSO)<sup>18</sup> that can be used for chemotherapeutic purposes. In the following sections, we extend this strategy to amphiphilic copolymers possessing a less hydrophobic terthiophene (TTT) payload together with a tosylate (OTs)-functionalized hydrophilic block.<sup>19,20</sup> We further demonstrate the ability to functionalize the resulting PNPs via displacement of the surface OTs groups. Because

TTT is both fluorescent and electrochemically active, TTT-cored PNPs functionalized with biologically active receptors on the PNP surface can potentially be used as analytical probes in bimodal biodiagnostic<sup>21</sup> applications.

## 4.2.2. Results and discussion

### 4.2.2.1. Synthesis of block copolymers $\text{TTT}_m\text{-}b\text{-(PEG-OTs)}_n$

We have shown previously that the terthiophene (TTT)-modified norbornene monomer **2.1** readily polymerizes in the presence of Grubbs first-generation catalyst.<sup>22</sup> Adding the more hydrophilic tosylated poly(ethylene glycol) (PEG-OTs)-modified norbornene monomer **4.2** to a growing ROMP chain of poly(**2.1**) results in an amphiphilic block copolymer  $\text{TTT}_m\text{-}b\text{-(PEG-OTs)}_n$  (Scheme 4.2), as indicated by the data in Table 4.1. The order of monomer addition is important, as demonstrated by the lower PDI (1.10 - 1.13) of the  $\text{TTT}_m\text{-}b\text{-(PEG-OTs)}_n$  polymers (made with poly(**2.1**) as the first block) in comparison to the reverse-synthesized polymer (PEG-OTs)<sub>15</sub>-*b*-TTT<sub>30</sub>, which has a higher PDI of 1.46. The higher 1.25 PDI for the initial (PEG-OTs)<sub>15</sub> block (Table 4.1, entry 1), compared to the lower 1.11-1.12 values for other (TTT)<sub>n</sub> blocks, up to n = 60 (Table 4.1, entries 2-5), can be used as an indicator that the homopolymerization of **4.2** is not quite “living”.<sup>23,24</sup> While the origin of this effect has not been investigated, we have observed similar PDI broadening for other block copolymers of **4.2**.<sup>16</sup> Because low polydispersity is an important requirement in the formation of PNPs,<sup>25,26</sup> only  $\text{TTT}_m\text{-}b\text{-(PEG-OTs)}_n$  polymers led to productive PNP formation (section 4.2.2.4).



**Scheme 4.2.** Reaction scheme for the general synthesis of a  $\text{TTT}_m\text{-}b\text{-(PEG-OTs)}_n$  block copolymer.

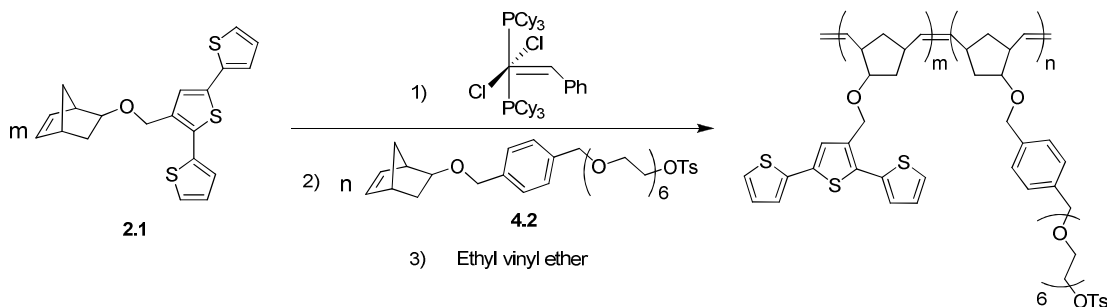


**Table 4.1.** Copolymer synthesis and analysis.

Entry	Polymer ( $A_n\text{-}b\text{-}B_m$ )	Grubbs's Monomer		$M_n$ of $A_n$ block (kD) <sup>b</sup>	PDI <sup>b</sup>	Monomer B (mmol)	Final $M_n$ (kD)	PDI
		Cat. (mmol)	A (mmol) <sup>a</sup>					
1	(PEG-OTs) <sub>15</sub> - <i>b</i> -TTT <sub>30</sub>	7.87	118	13.98	1.25	236.0	19.28	1.46
2	TTT <sub>30</sub> - <i>b</i> -(PEG-OTs) <sub>15</sub>	4.50	135	14.27	1.12	67.6	23.46	1.13
3	TTT <sub>40</sub> - <i>b</i> -(PEG-OTs) <sub>15</sub>	6.17	247	16.15	1.12	92.5	25.53	1.10
4	TTT <sub>45</sub> - <i>b</i> -(PEG-OTs) <sub>15</sub>	3.00	135	19.15	1.12	45.5	27.92	1.12
5	TTT <sub>60</sub> - <i>b</i> -(PEG-OTs) <sub>15</sub>	8.51	510	25.38	1.11	127.0	32.69	1.13

<sup>a</sup> Monomer A corresponds to the first monomer listed in the block copolymer name. <sup>b</sup> Data obtained for an aliquot taken before addition of monomer B.

#### 4.2.2.2. Fluorescence studies of terthiophene-containing materials

The viability of PNPs as an encapsulated carrier for fluorescent terthiophene units was determined by comparing the fluorescence spectrum of the block copolymer  $\text{TTT}_{60}\text{-}b\text{-(PEG-OTs)}_{15}$  to those of free terthiophene and free monomer **4.1** (Figure 4.2). As expected, the fluorescence spectrum of **2.1** is essentially identical to that of free terthiophene, and we were pleased to observe that fluorescence activity of the terthiophene unit within the polymer environment is not negatively hindered by its attachment to the poly(norbornene) backbone or by the clustering of many terthiophene units. Although exciplex formation<sup>27</sup> in the polymer sample appears to result in a red-shifted peak and 30% lower maximum intensity, the integrated peak intensity is actually 5% higher than free terthiophene at the same concentration. The broadening

of the terthiophene peak into the 500-nm range can be an asset in future deployment of the block copolymers into inexpensive hand-held devices using low-cost photodiodes with low-energy spectral-responses.<sup>28</sup>

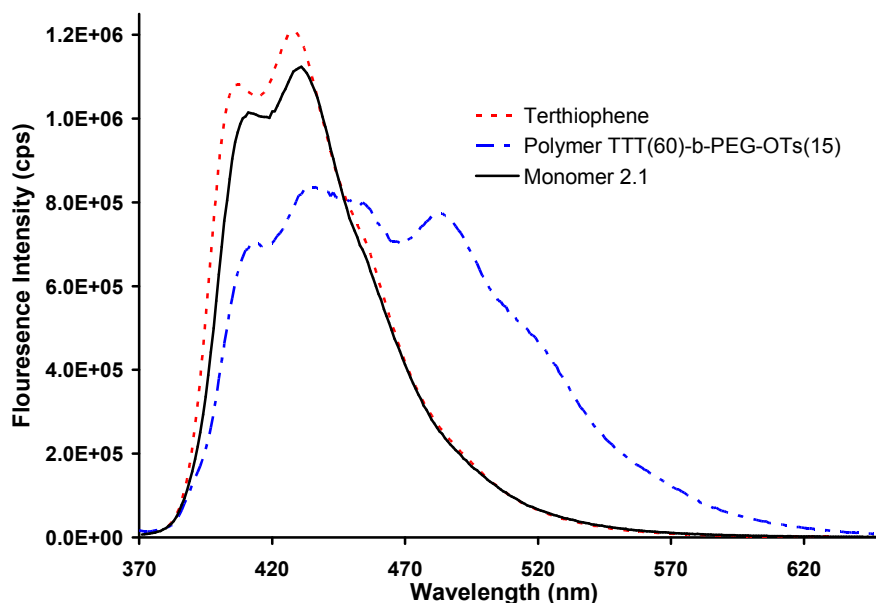


**Figure 4.2.** The fluorescence spectra of chloroform solutions of terthiophene, monomer **2.1**, and block copolymer TTT<sub>60</sub>-*b*-(PEG-OTs)<sub>15</sub>.

#### 4.2.3. Electrochemical studies of terthiophene-containing materials

Similar to the fluorescence study above, the feasibility of PNPs as an encapsulated carrier for redox active terthiophene units was determined by evaluating the redox properties of the block copolymer TTT<sub>60</sub>-*b*-(PEG-OTs)<sub>15</sub> against that of free terthiophene and free monomer **2.1**. In our cyclic voltammetric conditions, redox cycling of terthiophene and TTT<sub>60</sub>-*b*-(PEG-OTs)<sub>15</sub> samples allows the slow deposition of an insoluble poly(terthiophene) film on the working electrode.<sup>29</sup> Because poly(terthiophenes) are easier to oxidize than terthiophenes in solution,<sup>30</sup> the oxidation peak on-set for these samples shift from 1.0 to 0.7 V as the films are grown over several cycles (Figure 4.3). This shift is more dramatic for the block copolymer because sixty

TTT units are brought to the surface with the oxidation of each polymer chain. The increased signal at lower voltages could also be advantageous if these materials are deployed in battery-powered diagnostic devices. Interestingly, monomer **2.1** behaves very different from terthiophene and TTT<sub>60</sub>-*b*-(PEG-OTs)<sub>15</sub> under redox conditions: solutions of **2.1** do not deposit films of poly(terthiophene) on the working electrode, but instead form a slightly green-colored solution around the working electrode.

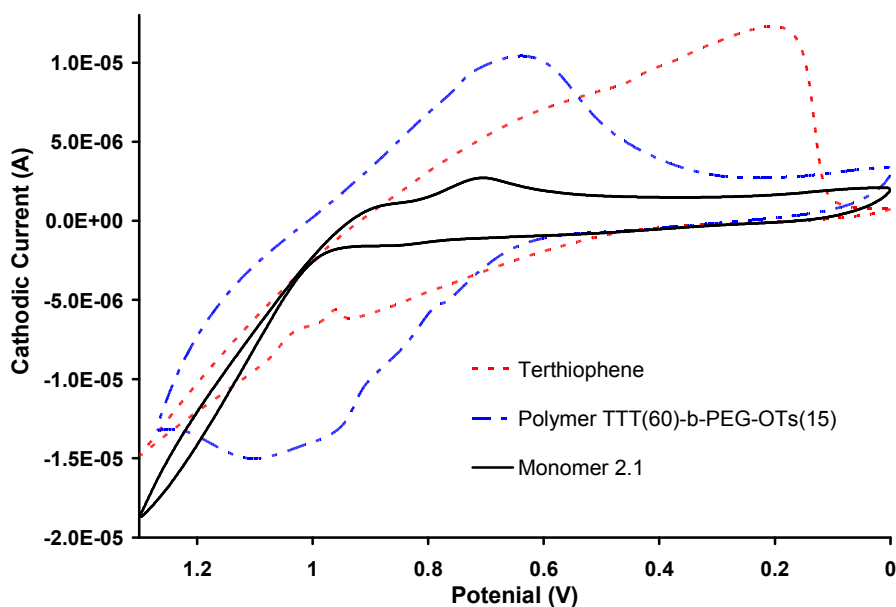


**Figure 4.3.** Cyclic voltammograms of terthiophene, monomer **4.1**, and block copolymer TTT<sub>60</sub>-*b*-(PEG-OTs)<sub>15</sub> after nine cycles between 0.0 and 1.30 V.

#### 4.2.4. PNP assembly

##### 4.2.4.1. Solvent optimization for the assembly of PNPs

As mentioned in section 4.2.1.1, forming PNPs from amphiphilic block copolymers requires first dissolving the polymer in a water-miscible solvent that is non-selective for either block of the copolymer, and slowly adding water to it to ‘precipitate out’ the locked core-shell structure. Although there are numerous water-miscible solvent options, the chemical

compatibility of the dialysis bags used in the dialysis step of PNP synthesis (see section 4.4.8) and the limited solubility of the copolymers (for example,  $\text{TTT}_m\text{-}b\text{-(PEG-OTs)}_n$  is insoluble in DMSO) limited our options to THF and DMF for this study. While the slow addition of water to a solution of  $\text{TTT}_m\text{-}b\text{-(PEG-OTs)}_n$  in either solvent results in a turbid suspension, indicating colloid formation (Table 4.2), DMF was preferred because the resulting PNPs were found to be more compact (Table 4.2, cf entries 3-5 vs 10-12) and physically more robust than those formed using THF during centrifugation and dialysis experiments (vide infra). Similar to previous studies,<sup>31</sup> the higher CWC (Figure 4.4) values of polymers dissolved in THF (>25 vol%  $\text{H}_2\text{O}$ ) (Table 4.2, entries 4-5) compared to those dissolved in DMF (~12 vol%  $\text{H}_2\text{O}$ ) (Table 4.2, entries 11-12) indicates that the THF/ $\text{H}_2\text{O}$  solvent system is less selective for the amphiphilic parent polymer than DMF/ $\text{H}_2\text{O}$ , leading to larger, less stable PNPs.

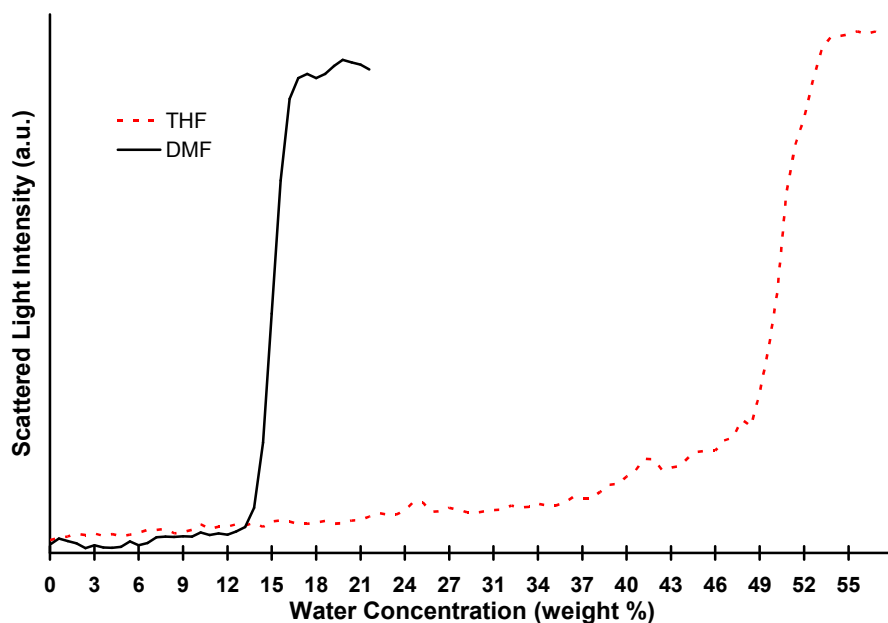


**Figure 4.4.** Static light-scattering data taken during water addition to solutions of  $\text{TTT}_{60}\text{-}b\text{-(PEG-OTs)}_{15}$  (0.010 wt%) in THF and DMF.

**Table 4.2.** Synthetic and characterization data for the PNPs used in this study.

Entry	Polymer	Solvent	Wt%	CWC (vol%)	Final H <sub>2</sub> O (vol%)	Diameter (nm)	PNP PDI
1	(PEG-OTs) <sub>15</sub> - <i>b</i> -TTT <sub>30</sub>	THF	0.010	–	43.7	ppt <sup>a</sup>	–
2	(PEG-OTs) <sub>15</sub> - <i>b</i> -TTT <sub>30</sub>	THF	0.100	–	43.7	ppt <sup>a</sup>	–
3	TTT <sub>30</sub> - <i>b</i> -(PEG-OTs) <sub>15</sub>	THF	0.010	–	43.7	500	0.17
4	TTT <sub>45</sub> - <i>b</i> -(PEG-OTs) <sub>15</sub>	THF	0.010	27.9	33.9	1000	0.01
5	TTT <sub>60</sub> - <i>b</i> -(PEG-OTs) <sub>15</sub>	THF	0.010	50.0	37.5	400	0.01
6	TTT <sub>40</sub> - <i>b</i> -(PEG-OTs) <sub>15</sub>	DMF	0.005	11.5	14.5	280	0.05
7	TTT <sub>40</sub> - <i>b</i> -(PEG-OTs) <sub>15</sub>	DMF	0.010	11.0	13.2	125	0.05
8	TTT <sub>40</sub> - <i>b</i> -(PEG-OTs) <sub>15</sub>	DMF	0.050	9.0	12.1	103	0.23
9	TTT <sub>40</sub> - <i>b</i> -(PEG-OTs) <sub>15</sub>	DMF	0.100	–	–	ppt <sup>a</sup>	–
10	TTT <sub>30</sub> - <i>b</i> -(PEG-OTs) <sub>15</sub>	DMF	0.010	12.5	19.8	115	0.14
11	TTT <sub>45</sub> - <i>b</i> -(PEG-OTs) <sub>15</sub>	DMF	0.010	12.0	30.0	130	0.01
12	TTT <sub>60</sub> - <i>b</i> -(PEG-OTs) <sub>15</sub>	DMF	0.010	13.3	23.1	291	0.38

<sup>a</sup> Polymer precipitated instead of forming a suspension of PNPs.

#### 4.2.4.2. Optimization of polymer loading in solutions for used for the formation of PNPs

To determine the ideal conditions for PNP formation, the initial mass of dissolved polymer in DMF was varied in the range of 0.005-0.1 wt% (Table 4.2). While 0.1-wt% loading was too concentrated and resulted in non-selective polymer precipitation during two different attempts (Table 4.2, entries 2 and 9), all but one of the lower loadings afforded PNPs. As expected, the (PEG-OTs)<sub>15</sub>-*b*-TTT<sub>30</sub> polymer was unsuitable for PNP synthesis due its high PDI value of 1.46: it quickly precipitated out of solution upon H<sub>2</sub>O addition, even at 0.01% loading (Table 4.2, entry 1). The broad distribution of polymer molecular weights in this sample corresponds to polymer chains with widely different solubilities, which eventually form insoluble aggregates opposed to PNP suspensions. For the model copolymer TTT<sub>40</sub>-*b*-(PEG-OTs)<sub>15</sub>, increasing polymer wt% lead to lower CWC and smaller particle size, which typically

signifies more robust particles, similar to that observed in previous studies.<sup>15</sup> The best combination of PDI and particle size was observed with 0.01-wt% loading and this was used for subsequent studies.

#### 4.2.4.3. Stability of PNPs

For the TTT-containing PNPs to be useful as scaffolds for subsequent addition of targeting groups and other functionalities, it is important that they are stable to physical manipulations, such as lyophilization and centrifugation, which are required in the functionalization processes.<sup>16</sup> At 0.01-wt% loading, while PNPs made from TTT<sub>30</sub>-*b*-(PEG-OTs)<sub>15</sub> were stable in solution, they easily lost their shapes upon air-drying on a TEM grid, consistent with the observation that TTT<sub>30</sub>-*b*-(PEG-OTs)<sub>15</sub> is low-melting. PNPs made from either TTT<sub>40</sub>-*b*-(PEG-OTs)<sub>15</sub> or TTT<sub>45</sub>-*b*-(PEG-OTs)<sub>15</sub> are both stable enough for TEM analysis; however, they appear “soft” and readily form undefined aggregates upon centrifugation or lyophilization (Figure 4.5, A and B).. Further increasing the hydrophobic block length to TTT<sub>60</sub>-*b*-(PEG-OTs)<sub>15</sub> resulted in more spherical PNPs that appear “rigid” and survive both centrifugation and lyophilization (Figure 4.5, C and D).

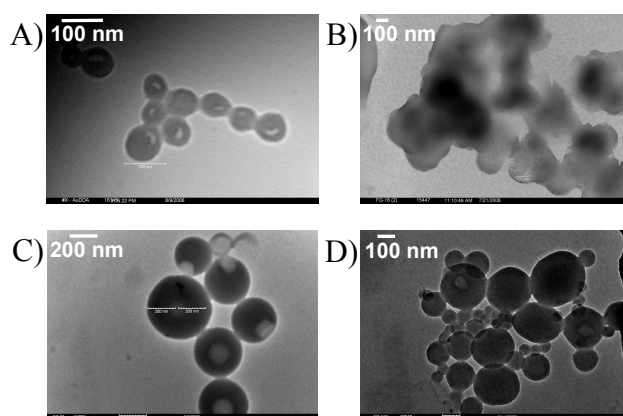


**Figure 4.5.** TEM images of two different dried PNP solutions before (left column) and after centrifugation (right column, 20 min at 1000 rpm). Images A and B are of TTT<sub>45</sub>-*b*-(PEG-OTs)<sub>15</sub>, while C and D are of TTT<sub>60</sub>-*b*-(PEG-OTs)<sub>15</sub>.

#### 4.2.5. Surface modification

Once suitably stable PNPs were formed, activity of their surface tosylates towards nucleophilic substitution was demonstrated by treating the PNPs with ethidium bromide monoazide in PBS buffer. Following purification, functionalization was verified by comparing the fluorescence spectra of DMF solutions of unmodified PNPs versus that of ethidium-modified PNPs (Figure 4.6), which clearly confirms the presence of ethidium on the surface of the latter. However, the best demonstration of ethidium substitution came from fluorescence microscopy: while the blue emission from the TTT groups is present in both samples (Figure 4.7, left column), the ethidium-specific red emission only appears in the ethidium-modified PNPs (Figure 4.7, right column). While nucleophilic displacement of OTs with ethidium bromide is shown here only as a proof of concept, the technique should be generally applicable with DNA and proteins.<sup>32</sup> Because each 200-nm PNP can associate one recognition event with up to  $10^7$  TTT molecules,<sup>17</sup> their analogous functionalization with bio-receptors should lead to highly amplified fluorescent probes that are suitable for diagnostic purposes.

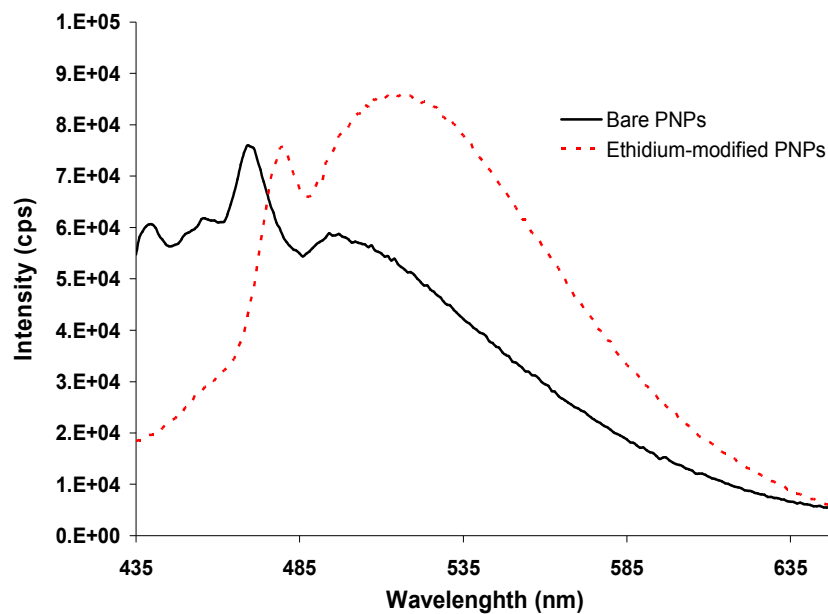


**Figure 4.6.** Fluorescence spectra of DMF solutions of bare PNPs and ethidium-modified PNPs.

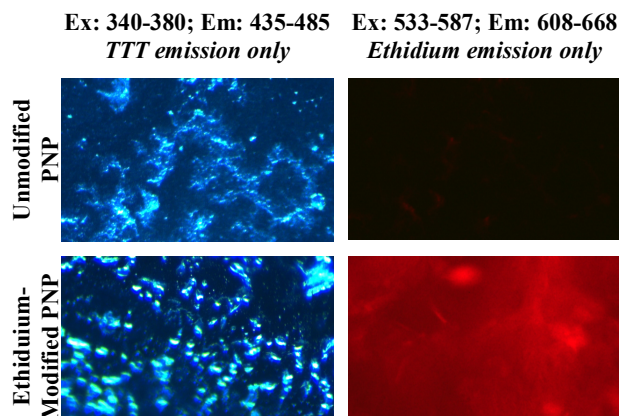


**Figure 4.7.** Fluorescence microscopy images of unmodified PNPs and ethidium-modified PNP after being dissolved in DMF and dried.

#### 4.2.6. Conclusions

Narrowly dispersed amphiphilic block copolymers of the form  $\text{TTT}_m\text{-}b\text{-(PEG-OTs)}_n$  can readily be made and assembled into core-shell PNPs. While many conditions afforded PNPs, optimization of polymer PDI, choice of non-selective solvent (DMF or THF), and hydrophobic block length were vital to accessing mechanically stable PNPs that can be further modified using



nucleophilic displacement chemistry. Analogous to free terthiophene, these amphiphilic block copolymers are both fluorescent and electrochemically active making them attractive for use as tags in biodiagnostics. In section 4.3, similar target-modified PNPs are used as analytical tags in a biodiagnostic application via fluorescence methods.

### **4.3. Labeled polymer nanoparticles as “loaded” probes for DNA detection**

#### **4.3.1. Introduction**

As mentioned in section 4.1.1, for most DNA detection applications the initial analyte DNA concentration in a given sample often lays far below the sensitivity of standard instrumentation, requiring an amplification procedure. The current industry standard for DNA amplification, polymerase chain reaction (PCR),<sup>2</sup> is a powerful tool that can enable the detection of merely a few sequences of DNA. The PCR method involves continuous replication of a target sequence of DNA initially present at very low concentration to a level where it can be easily detected. However, since this strategy involves repetitive enzyme-based replication, it is not immune to mistakes and can take hours (frequently days) to sufficiently amplify the target sequence. The overall DNA analysis can therefore take up to a week; far too long if the incubation period for a disease is only a few days. To diagnose illnesses more quickly, it is imperative that disease-specific sequences of DNA can be accurately detected at very low concentrations and on a timely basis.

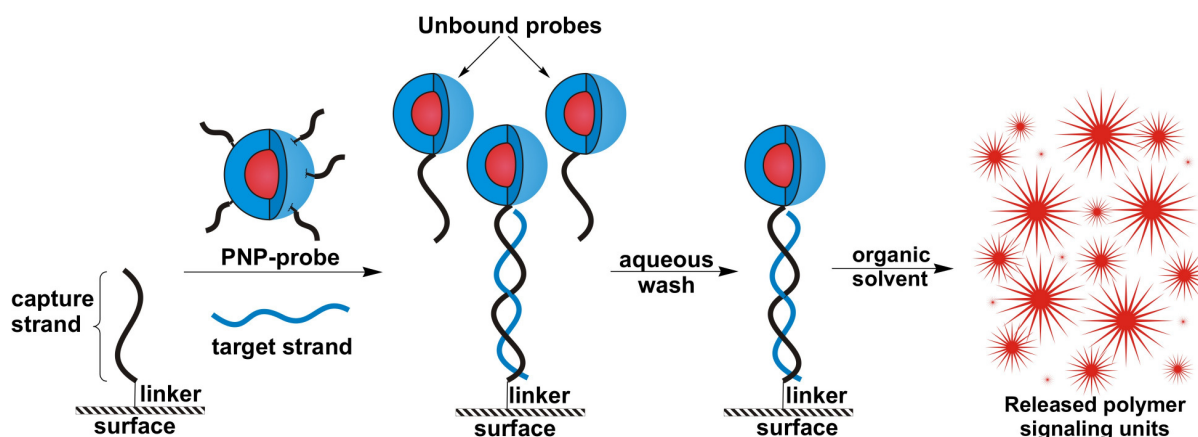
At the present, techniques to increase the sensitivity and efficiency in DNA detection assays are being explored in laboratories across the world.<sup>33</sup> Below, we describe a PNP-based, sequence-specific assay that does not require a separate amplification step, potentially enabling detection of DNA levels at better than femtomolar range. Application of this methodology to DNA detection could yield results in much shorter time periods than current technologies.

#### **4.3.2. Loaded Probes**

In the section 4.2, we discussed the block copolymerization of norbornene-modified terthiophene (TTT) and norbornene-modified poly(ethyleneglycol)-tosylate (PEG-OTs) monomers which resulted in well-defined, narrowly dispersed amphiphilic block copolymers of

the form  $\text{TTT}_m\text{-}b\text{-(PEG-OTs)}_n$  that were both fluorescent and electrochemically active. These copolymers were used to fabricate stable polymer nanoparticles (PNPs) with surface OTs groups and TTT cores. Activity of the OTs groups was verified by treatment of the core-shell PNPs with ethidium bromide monoazide to afford PNPs that were surface-functionalized with ethidium dye molecules. Given the high loading of TTT per PNP (section 4.2.5), we propose that their surface functionalization with DNA should lead to highly selective, payload-amplified fluorescent probes that are suitable for diagnostic purposes. In this section the progress towards a PNP-based DNA detection assay utilizing DNA functionalized TTT-core PNPs is described (Scheme 4.3).

**Scheme 4.3.** In a sandwich assay, as described in Figure 4.1, a PNP-based probe is brought to the surface through duplex formation with capture and a target strand. Unbound probes are washed away with aqueous rinses. When the bound PNPs are subsequently dissolved in organic solvent, up to  $10^7$  TTT groups would be released from a single 200-nm PNP leading to an amplified signal.



### 4.3.3. Results and discussion

#### 4.3.3.1. PNP probe formation

PNPs with surface OTs groups and TTT cores were assembled from amphiphilic block copolymers of  $\text{TTT}_{60}\text{-}b\text{-(PEG-OTs)}_{15}$  as described in section 4.2. They were then functionalized

with a probe DNA strand via incubation with amine-terminated DNA in PBS buffer (10 mM, 8.0 pH) (PNP probes). Following DNA-functionalization, PNP probes were treated with 13-nm gold nanoparticles (GNPs) that had been functionalized with either complementary or non-complementary DNA (DNA-GNPs), and interactions were visualized by transmission electron microscopy (TEM) (Figure 4.8). Proper functionalization was confirmed by the PNP-based probes only adhering to the complementary DNA-GNPs.

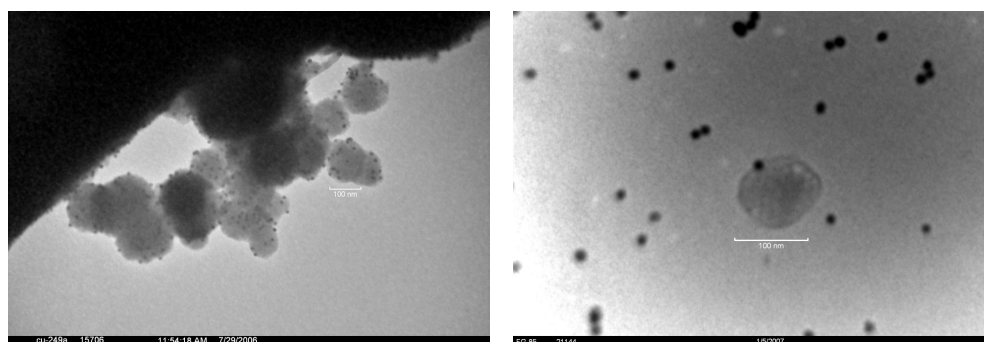


**Figure 4.8.** TEM images of PNP-based probes (large gray spheres) after incubation with complementary (left image) and non-complementary (right image) DNA-GNPs (small black spheres).

#### 4.3.3.2. DNA detection with PNP-based probes

Glass slides with a spherical depression (Figure 4.9) were first functionalized with 11-(trichlorosilyl)undecanoic acid NHS ester, as an amine reactive linker.<sup>34</sup> The slides were then incubated with the amine-terminated capture DNA strand, and rinsed with nanopure water to remove unreacted DNA strands. After rinsing the slides, sandwich assays were performed with 100  $\mu$ L samples containing target DNA and either polymer-based or PNP-based probes in buffered solution (10 mM PBS, pH 7.0, 0.3 M NaCl) (Figure 4.10).



**Figure 4.9.** Glass slides with either one or two spherical depressions (16 mm diameter; 0.50 mm depth) for holding liquid samples.

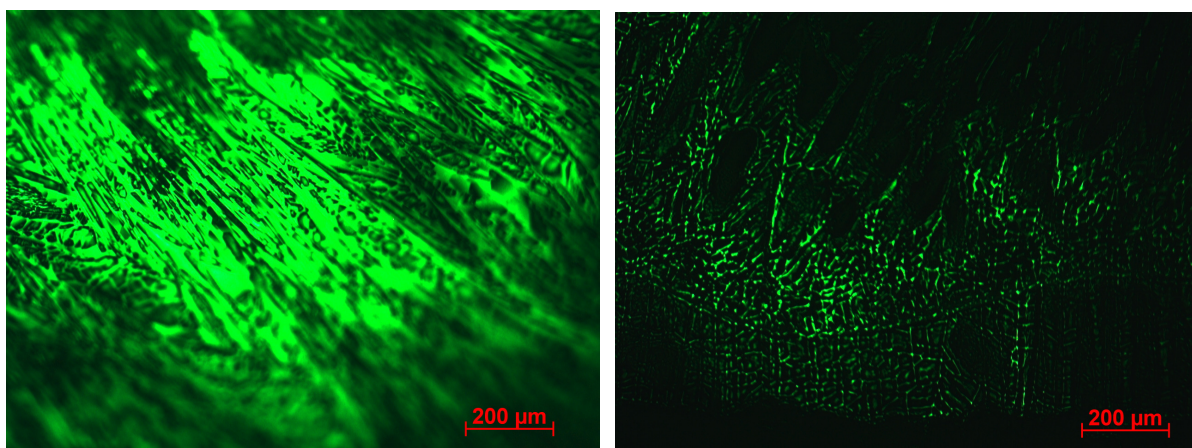


**Figure 4.10.** Fluorescence microscopy images following sandwich assays using glass slides with bound capture strands, 100 pM target DNA, and either PNP-based (Left) or polymer-based (Right) probes. After dissolving probes in methylene chloride, solvent is allowed to dry and a polymer film is formed which is subsequently viewed by fluorescence microscopy.

The distinct difference between the fluorescence microscopy images of the PNP-based sample and the polymer-based sample demonstrates the potential of the PNP-based probe system. However, there are several limitations to this glass-slide based platform. Primarily, the hybridization efficiency of the DNA is limited by the two-dimensional surface and the lower-limit of sensitivity is hindered due to fluorescence potential self-quenching in the film. As such, future work will include the development of capture-strand-modified microspheres that will

allow for three-dimensional interaction with target DNA and the PNP probes and will facilitate solution-phase fluorescence detection.

#### **4.3.4. Conclusions**

In summary, we have established that PNPs assembled from  $\text{TTT}_{60}\text{-}b\text{-(PEG-OTs)}_{15}$  block copolymers can be functionalized with amine-terminated DNA strands to make PNP-based probes. TEM visualization has verified the selectivity of the PNP probes towards complementary functionalized DNA-GNPs. The enhanced detection results obtained for PNP-based probes in an assay using capture strand-modified glass slides demonstrates their promise in the future work utilizing capture strand-modified polystyrene microspheres.

## 4.4. Experimental

### 4.4.1. General considerations

Polymer molecular weights were measured relative to polystyrene standards on a Waters gel-permeation chromatograph (GPC) equipped with Breeze software, a 717 autosampler, Shodex KF-G guard column, KF-803L and KF-806L columns in series, a Waters 2440 UV detector, and a 410 RI detector. HPLC-grade THF was used as the GPC eluent at a flow rate of 1.0 mL/min, and the instrument was calibrated using polystyrene standards (Aldrich, 15 standards, 760-1,800,000 Daltons). For GPC samples, a PDI of 1.0 is indicative of a monodisperse polymer sample.

Static light-scattering (SLS) experiments were performed on a DAWN-EOS multi-angle laser photometer (Wyatt Technology, Santa Barbara, CA) equipped with a He-Ne laser (632.8 nm). Dynamic light-scattering (DLS) measurements were performed on a Brookhaven Instruments Corp. photon correlation spectrometer (BI-200 SM goniometer) fitted with a Brookhaven Instruments BI-9000AT digital correlator and a 3-W argon-ion laser delivering monochromatic light of 514.5 nm at a scattering angle of 90°. A bath of filtered decalin (through a 0.2- $\mu$ m filter) surrounded the DLS cell, and the temperature was fixed at 25 °C. Data for each DLS sample was collected on a continuous basis for two minutes in sets of three. Based on the scattered light intensity of the solution, the average diameter of the particles and the monodispersity are calculated and given as the polydispersity index (PDI). In a DLS experiment, a PDI of zero equates to a monodisperse sample.

Transmission electron microscopy (TEM) work was performed on a Hitachi H8100 microscope operating at an accelerating voltage of 200 kV. TEM samples were prepared by

depositing 10  $\mu\text{L}$  of aqueous PNP solutions onto copper EM grids (Ted Pella, Inc., Redding, CA, 400 mesh, Formvar/carbon-coated). The samples were air-dried before TEM measurement.

Cyclic voltammetry (CV) data was acquired on a CHI900 scanning electrochemical microscope using a conventional three-electrode cell (Pt wire working electrode, Ag/AgCl reference electrode, and Pt wire counter electrode).

Fluorescence spectra were obtained on a Jobin Yvon-SPEX Fluorolog fluorometer using a conventional quartz cell (1-cm path length) and HPLC grade solvents. Fluorescence microscopy was performed using a Zeiss Axiovert 200M microscope with a mercury excitation lamp, an AxioCam MRc5 for recording color digital images, and Axiovision software for image processing. Excitation and emission light were passed through a pair of fluorescence filters before viewing (excitation filter options: 340-380, 460-500, or 533-587 nm; emission filter options: 435-485, 510-560, or 608-682 nm).

#### 4.4.2. Materials

Terthiophene-modified norbornene (3'-(*exo*-5-norbornene-2-oxy)methyl-2,2':5',2''-terthiophene, **2.1**) and tosylated hexaethylene glycol-modified norbornene (**4.2**) were synthesized using published procedures.<sup>16,22</sup> All other reagents and reagent grade solvents were purchased from Acros Organic, Strem Chemicals Inc., or Aldrich Chemical Company and used as received. Dry methylene chloride was prepared by passing HPLC-grade methylene chloride over neutral alumina via a Dow-Grubbs solvent system.<sup>35</sup> Dry solvent was collected under argon, degassed under vacuum, and stored under nitrogen in a Strauss flask prior to use. Nanopure water (18.2 M $\Omega$  cm resistivity) was obtained from a Milipore system (Mili-Q Biocel). Dialysis tubes



(Spectra/Por Float-a-lyzer RC, 10-mL, MWCO = 8000) were purchased from Spectrum Laboratories (Rancho Dominguez, CA).

Syntheses of DNA sequences were performed on an Expedite 8909 Nucleic Acid system. Unmodified DNA was purified on an Agilent 1100 HPLC equipped with a Varian Dynamax column (250 mm x 10.0 mm (L x ID), Microsorb 300-10 C18) using a gradient method beginning with 100 vol% 0.03M TEAA (TEAA = triethylammonium acetate) in ultrapure water, and increasing to 50 vol% acetonitrile (containing 5 vol% of 0.03M aqueous TEAA buffer) over 50 minutes, with a flow rate of 3 mL/min. Absorption spectra and melting analyses of DNA materials were recorded on a Varian Cary 300 Bio UV-Vis spectrophotometer using a Starna quartz cell (path length = 10 mm).

#### 4.4.3. General polymer synthesis

Block copolymers with varying ratios of pendant terthiophene (TTT) and tosylated polyethylene glycol (PEG-OTs) groups were prepared via ring-opening metathesis polymerization (ROMP) using controlled stoichiometries of monomers **2.1** and **4.2** (vide supra, Scheme 4.2). The molecular weight and PDI of the synthesized block polymers were determined by GPC (vide supra, Table 4.1).

**Synthesis of (TTT)<sub>30</sub>-b-(PEG-OTs)<sub>15</sub>.** In an inert-atmosphere glovebox, a solution of Cl<sub>2</sub>(PCy<sub>3</sub>)<sub>2</sub>Ru=CHPh catalyst (6 mg, 4.5 μmol) in dry CH<sub>2</sub>Cl<sub>2</sub> (1 mL) was added in a single dose to a 20-mL scintillation vial containing a stirred solution of monomer **2.1** (50 mg, 135.0 μmol) in dry CH<sub>2</sub>Cl<sub>2</sub> (4 mL). After stirring for 30 min at room temperature, an aliquot (100 μL) was removed, quenched with ethyl vinyl ether (100 μL), and analyzed by GPC. Subsequently, a solution of monomer **4.2** (44 mg, 67.6 μmol) in CH<sub>2</sub>Cl<sub>2</sub> (1 mL) was added to the reaction in a

single dose and the resulting mixture was allowed to stir for an additional 30 min. Following termination by the addition of ethyl vinyl ether (1 mL), the copolymer (TTT)<sub>30</sub>-*b*-(PEG-OTs)<sub>15</sub> (87 mg, 93% yield) was isolated as an off-white solid by precipitation into cold pentanes (200 mL), filtering, and washing with pentanes (3 x 50 mL).

#### 4.4.4. Fluorescence of terthiophene, monomer **2.1**, and polymer TTT<sub>60</sub>-*b*-(PEG-OTs)<sub>15</sub>

Solutions (10<sup>-6</sup> M in HPLC grade CHCl<sub>3</sub>) of terthiophene, monomer **2.1**, and polymer TTT<sub>60</sub>-*b*-(PEG-OTs)<sub>15</sub> were each irradiated at 352 nm and the fluorescence spectra were collected from 371-650 nm.

#### 4.4.5. Electrochemistry of terthiophene, monomer **2.1**, and polymer TTT<sub>60</sub>-*b*-(PEG-OTs)<sub>15</sub>

Solutions (10<sup>-4</sup> M in 0.1 M tetrabutylammonium hexafluorophosphate (TBAPF<sub>6</sub>) in HPLC grade CH<sub>2</sub>Cl<sub>2</sub>) of terthiophene, monomer **4.1**, and polymer TTT<sub>60</sub>-*b*-(PEG-OTs)<sub>15</sub> were each scanned 10 times between 0.0 and 1.3 V at a scan rate of 100 mV/s.

#### 4.4.6. General preparation of PNPs

As mentioned above, formation of PNPs involves slow addition of water to a dilute solution of copolymer in a water-miscible organic solvent. This process is monitored by SLS to identify the CWC for the copolymer solution, at which point the intensity of scattered light suddenly and significantly increases, signifying nanoparticle formation (Figure 4.4). After further addition of water to ensure complete particle formation (*vide supra*), suspensions of particles were dialyzed to remove all the organic solvents following a method developed by Eisenberg and coworkers.<sup>12</sup> Average PNP diameter and PDI were determined by DLS analysis (Table 4.2), followed by visualization of PNP samples using TEM.

**Preparation of PNPs from (TTT)<sub>30</sub>-*b*-(PEG-OTs)<sub>15</sub>.** A stock solution of copolymer (TTT)<sub>30</sub>-*b*-(PEG-OTs)<sub>15</sub> (0.01 wt%) in DMF was stirred for 4 h at room temperature to ensure

complete polymer solubilization. An aliquot (8.0 mL) was transferred to a 20-mL scintillation vial and allowed to stir vigorously. Nanopure water was added to the stirring copolymer solution at a rate of 25  $\mu\text{L}$  per minute using a micro-pipette, with an SLS reading taken after each addition until the solution reached the CWC. To ensure complete particle formation, nanopure water addition was continued at the same rate until the solution contained  $\sim 44$  vol%  $\text{H}_2\text{O}$ . An aliquot (10 mL) of the resulting solution was placed in a dialysis tube and dialyzed against nanopure water in a 500-mL Erlenmeyer flask with the dialysis solution changed every 30 min for the first 6 h and then every 8 h for the next 24 h. Complete removal of DMF from the filtrate was verified by UV-vis spectroscopy as indicated by the disappearance of the UV cut-off for DMF at 270 nm. The nanoparticle suspension (10.2 mL) was removed from the dialysis membrane and stored in a 20-mL scintillation vial at 10  $^\circ\text{C}$ .

#### **4.4.7. Functionalization of PNPs with ethidium bromide monoazide**

Tosylated-PNP solutions containing 0.01 wt% copolymer were prepared as described in section 4.4.6. An aliquot (500  $\mu\text{L}$ , 54  $\mu\text{g}$  of copolymer) was transferred to a 1.5-mL Safe-Lock Eppendorf tube, centrifuged for 30 min at 10K rpm to a solid pellet, which was removed from the supernatant via decantation. The resulting solid pellet of PNPs were re-suspended upon mild vortexing in PBS buffer (250  $\mu\text{L}$ , 10 mM, pH = 8.5) containing ethidium bromide monoazide (1 mg) and set on a platform shaker (112 rpm) at room temperature for 18 h. Purification of the ethidium-modified PNPs was achieved using centrifuge filters (Centricon YM-100, MWCO = 100,000, Millipore, Billerica, MA) with PBS buffer (10 mM, pH = 7.0). Filtration was repeated (5 times) until no fluorescence (Ex: 472 nm) signal was observed in the filtrate. The ethidium-modified PNPs were dissolved in DMF/ $\text{H}_2\text{O}$  (2:1 v/v), examined by SLS measurement to

verified that no PNPs remained, and centrifuge-filtered (Centricon YM-3, MWCO = 3,000, Millipore, Billerica, MA) to facilitate removal of any non-covalently bound ethidium bromide. The fluorescence activity of the dissolved ethidium-modified PNPs was compared to that of the unmodified PNPs using solution fluorimetry and fluorescence microscopy.

#### **4.4.8. General procedure for the preparation of DNA-functionalized PNPs**

Tosylated PNP solutions containing 0.01 wt% copolymer were prepared as stated above. An aliquot (500  $\mu$ L, 54  $\mu$ g of copolymer) was transferred to a 1.5-mL Safe-Lock Eppendorf tube and centrifuged for 30 min at 10K rpm to a solid pellet. The supernatant was removed and the PNPs were re-suspended in PBS buffer (250  $\mu$ L, 10 mM, pH = 8.5, [NaCl] = 81 mM) upon mild vortexing. An aliquot (100  $\mu$ M) of the appropriate 5'-amine-modified oligonucleotide (5'-NH<sub>2</sub>-TTT-TTT-CTT-ATC-AAT-ATT-3') in the same PBS buffer was added and the foil-wrapped suspension was set on a platform shaker (112 rpm) at room temperature for 18 h. Purification of the DNA-modified PNPs was achieved using centrifuge filters (Centricon YM-100, MWCO = 100,000) (Millipore, Billerica, MA) with PBS buffer (10 mM, pH = 7.0, [NaCl] = 0.15 M).

To verify DNA functionalization of the PNPs, an aliquot (10  $\mu$ L) of the DNA-modified PNPs was transferred to a separate Eppendorf tube. To this tube was added an aliquot (1  $\mu$ L, 10nM gold) of GNPs (13 nm) functionalized with the complementary DNA sequence (5'-SH-TTT-TTT-AAT-ATT-GAT-AAG-3') in PBS buffer (10 mM, pH = 7.0, [NaCl] = 0.15 M). The suspension was heated at 45 °C for 1 min and allowed to cool to room temperature overnight. Hybridization between the PNPs and the GNPs was confirmed by TEM. Simultaneously, control experiments were carried out between the DNA-functionalized PNPs and the GNPs (13 nm) functionalized with a non-complementary DNA sequence (5'-SH-TTT-TTT-CTT-ATC-AAT-

ATT-3'). Both experiments were performed in the same manner as described above and analyzed by TEM.

#### **4.4.9. Preparation of DNA modified TTT<sub>60</sub>-*b*-(PEG-OTs)<sub>15</sub>**

DNA modified PNPs made using TTT<sub>60</sub>-*b*-(PEG-OTs)<sub>15</sub> were prepared as described above. Following purification, half of the sample was centrifuge filtered with nanopure water (3 x 1 mL) to exchange out the PBS buffer. The solution was then frozen and lyophilized to dryness. The remaining powder was brought up in 250  $\mu$ L DMF/H<sub>2</sub>O (2:1 v/v), and examined by SLS measurement to verified that no PNPs remained.

#### **4.4.10. DNA Detection using PNP and polymer probes**

Glass slides with a spherical depression (16 mm diameter; 0.50 mm depth) were first functionalized with 11-(trichlorosilyl)undecanoic acid NHS ester (1 mg/mL in toluene for 1h), as an amine-reactive linker, following published methods.<sup>10</sup> The slides were then incubated for 8 h with the 3'-amine-terminated DNA capture strand (5'-TAA-CAA-TAA-CCT-TTT-TTT-NH<sub>2</sub>-3') in PBS buffer ([DNA] = 200  $\mu$ M, [PBS] = 10 mM, pH = 8.5, [NaCl] = 81 mM), and rinsed with nanopure water to remove unreacted DNA strands. After rinsing the slides, DNA detection assays were performed with 1000- $\mu$ L samples containing target DNA (5'-GGA-TTA-TTG-TTA-AAT-ATT-GAT-AAG-3' –ranging from 0 to 1  $\mu$ M in target DNA) and either PNP probes or polymer probes (both made from TTT<sub>60</sub>-*b*-(PEG-OTs)<sub>30</sub>) in buffered solution (10 mM PBS, pH 7.0, 0.3 M NaCl). After 4 hours the slides were rinsed with PBS buffer (5 x 2 mL), and methylene chloride (1 mL) was added to dissolve the bound PNPs. Following evaporation of solvent, fluorescence microscopy was used to visualize the intensity of TTT on the surface.

**Chapter 5**

**Epilogue**

The focus of this thesis has been to demonstrate the advantageous properties of the hybrid materials that result from chemically linking two or more dissimilar components. Specifically, it has been shown that the properties of organic small molecules can be enhanced when these molecules are elaborated into polymers and coupled to the native recognition properties of biomaterials such as DNA. The ensuing hybrids have been employed in the development of materials for biodiagnostic and electronic applications.

### **5.1. Summary and outlook for chapter 2**

In chapter 2, the native properties of poly(terthiophene) were improved by attaching the terthiophene groups onto a poly(norbornene) backbone prior to polymerization. Polymer films made from this material possess enhanced thermal-stability and surface smoothness. As opposed to the localized three-dimensional nuclei that form during electrochemical deposition of native terthiophene, which lead to rough films, the poly(norbornene) backbone facilitates two-dimensional film-growth by bringing numerous terthiophene groups to the surface over a relatively large surface area. These improved surface properties aided the fabrication of fluorescent multicomponent nano-scale rods synthesized by the electrochemical deposition of gold, silver, and cross-linked polymer into the pores of an anodized aluminum oxide template.

In addition to performing the photo-physical studies needed to evaluate the fluorescence properties of the multicomponent nano-scale rods, further work in this area could include the development of new pendant groups on the poly(norbornene) backbone. For example, increasing the unit-length of the pendant oligo(thiophene) on the poly(norbornene) backbone from 3 thiophene units (terthiophene) to 5 thiophene units (pentathiophene) would increase the poly(thiophene) composition of the cross-linked polymer and could improve the conductivity of

the hybrid materials. Other thiophene derivatives with tunable electrochromicities<sup>1</sup> and conductivities<sup>2</sup> could also benefit from the enhanced transparency and stability of the cross-linked films, making possible “smart” windows with color-changing ability or solar cell applications.

## 5.2. Summary and outlook for chapter 3

Chapter 3 focused on elucidating the parameters that lead to the enhanced melting characteristics observed for DNA hybrid materials. Rigid small-molecule DNA hybrids (rSMDHs) where three DNA strands are attached to a rigid tris(phenylacetylene) core through benzyl phosphate bonds were used to form caged rSMDH:rSMDH dimers with enhanced melting behaviors, observable for the first time in a well-defined DNA hybrid system. Importantly, this result showed that enhanced melting behaviors in DNA hybrid materials is dependant on closely spaced (25-40 Å) parallel DNA duplexes, and requires as few as three cooperative duplexes.

While the synthesis of the benzyl phosphate-linked rSMDHs yielded sufficient material for testing, the synthetic route was not amiable to diversification. To this end, the small-molecule DNA hybrid (SMDH) platform was extended to flexible SMDHs (fSMDHs) with alternating poly(ethylene glycol) spacers between three DNA strands and towards modularly constructed rSMDHs with DNA strands linked to the small-molecule core via triazole linkages. In both of these two cases, commercial availability of precursors and modularity of the synthetic routes were distinct advantages.

Current and future work could be concentrated on synthesizing the core materials needed to thoroughly evaluate the effects of geometry and DNA-density on the melting properties of DNA hybrids. Notably, the construction of a face-to-face rSMDH:rSMDH dimer with no



parallel duplexes, compared to three parallel duplexes in the cage dimer (vide supra), would lend support to hypothesized requirement of having parallel duplexes. Additionally, hybrids with two DNA strands attached could be used to test whether two is the lowest number of cooperative duplexes required for enhanced melting.

### **5.3. Summary and outlook for chapter 4**

The work in chapter 4 outlined the development of a “loaded”, intrinsically amplified probe for DNA diagnostics through the combination of the fluorescent signaling properties of the poly(norbornene-terthiophene) materials studied in chapter 2 and the recognition properties of the DNA hybrid materials used in chapter 3. Polymer nanoparticles (PNPs) were assembled from amphiphilic block copolymers containing fluorescent terthiophene groups and functionalized with DNA to create a PNP-DNA hybrid material which was implemented as a probe in a DNA detection assay. Compared to the probes made from the free polymer, the signal from the PNP probes was amplified by at least two orders of magnitude.

The first step towards improving this system would be to move from a two-dimensional assay on a glass slide to a three-dimensional assay using glass beads. Doing so would improve the kinetics of DNA duplex formation between the surface, target, and probe strands, while also facilitating a more reliable and quantifiable solution-phase readout. Sensitivity could be further enhanced by changing the signaling portion of the block copolymer to a improved redox couple such as ferricinium/ferrocene, a better fluorophore like fluorescein, or a molecule that has been optimized for localized surface plasmon resonance (LSPR) such as rhodamine 6G.<sup>3</sup> Combining the amplification properties of the PNP probes with an already highly sensitive technique such as LSPR could yield a truly superior detection platform.



## References

## Chapter 1

- (1) *Hybrid Materials: Synthesis, Characterization, and Applications*; Kickelbick, G., Ed.; Wiley-VCH Verlag GmbH & Co. KGaA: Weinheim, Germany, 2007.
- (2) Prockop, D. J.; Kivirikko, K. I. *N. Engl. J. Med.* **1984**, *311*, 376-386.
- (3) <http://en.wikipedia.org/wiki/Nacre>, accessed: August 08, 2008.
- (4) Lin, A.; Meyers, M. A. *Mater. Sci. Eng., A* **2005**, *390*, 27-41.
- (5) Fengel, D.; Wegener, G. *Wood: Chemistry, Ultrastructure, Reactions*; Walter de Gruyter: Berlin and New York, 1988.
- (6) Brandstrom, J. *Nord. Pulp & Paper Res. J.* **2004**, *19*, 13-17.
- (7) Freestone, I.; Meeks, N.; Sax, M.; Higgitt, C. *Gold Bulletin* **2007**, *40*, 270-277.
- (8) JoseYacaman, M.; Rendon, L.; Arenas, J.; Puche, M. C. S. *Science* **1996**, *273*, 223-225.
- (9) Sargeant, T. D.; Guler, M. O.; Oppenheimer, S. M.; Mata, A.; Satcher, R. L.; Dunand, D. C.; Stupp, S. I. *Biomaterials* **2008**, *29*, 161-171.
- (10) Gratzel, M. J. *Photochem. Photobiol. A: Chem.* **2004**, *164*, 3-14.
- (11) [http://upload.wikimedia.org/wikipedia/commons/4/4c/Solar\\_Spectrum.png](http://upload.wikimedia.org/wikipedia/commons/4/4c/Solar_Spectrum.png), accessed: August 08, 2008.
- (12) Aldaye, F. A.; Sleiman, H. F. *Angew. Chem., Int. Ed.* **2006**, *45*, 2204-2209.
- (13) Gothelf, K. V.; Thomsen, A.; Nielsen, M.; Clo, E.; Brown, R. S. *J. Am. Chem. Soc.* **2004**, *126*, 1044-1046.
- (14) Li, Y. G.; Tseng, Y. D.; Kwon, S. Y.; D'Espaux, L.; Bunch, J. S.; Mceuen, P. L.; Luo, D. *Nat. Mater.* **2004**, *3*, 38-42.
- (15) Mueller, J. E.; Du, S. M.; Seeman, N. C. *J. Am. Chem. Soc.* **1991**, *113*, 6306-6308.
- (16) Shih, W. M.; Quispe, J. D.; Joyce, G. F. *Nature* **2004**, *427*, 618-621.
- (17) Stewart, K. M.; McLaughlin, L. W. *J. Am. Chem. Soc.* **2004**, *126*, 2050-2057.
- (18) Frutos, A. G.; Smith, L. M.; Corn, R. M. *J. Am. Chem. Soc.* **1998**, *120*, 10277-10282.
- (19) Saghatelian, A.; Voelcker, N. H.; Guckian, K. M.; Lin, V. S. Y.; Ghadiri, M. R. *J. Am. Chem. Soc.* **2003**, *125*, 346-347.
- (20) Wu, G.; Seeman, N. C. *Nat. Computing* **2006**, *5*, 427-441.

- (21) Becerril, H. A.; Stoltenberg, R. M.; Wheeler, D. R.; Davis, R. C.; Harb, J. N.; Woolley, A. T. *J. Am. Chem. Soc.* **2005**, *127*, 2828-2829.
- (22) Daubendiek, S. L.; Ryan, K.; Kool, E. T. *J. Am. Chem. Soc.* **1995**, *117*, 7818-7819.
- (23) Eckardt, L. H.; Naumann, K.; Pankau, W. M.; Rein, M.; Schweitzer, M.; Windhab, N.; von Kiedrowski, G. *Nature* **2002**, *420*, 286-286.
- (24) Nielsen, M.; Dauksaite, V.; Kjems, J.; Gothelf, K. V. *Bioconjugate Chem.* **2005**, *16*, 981-985.
- (25) Summerer, D.; Marx, A. *Angew. Chem., Int. Ed.* **2002**, *41*, 89-90.
- (26) Gaylord, B. S.; Heeger, A. J.; Bazan, G. C. *J. Am. Chem. Soc.* **2003**, *125*, 896-900.
- (27) Marti, A. A.; Puckett, C. A.; Dyer, J.; Stevens, N.; Jockusch, S.; Ju, J.; Barton, J. K.; Turro, N. J. *J. Am. Chem. Soc.* **2007**, *129*, 8680-8681.
- (28) Yu, C. J.; Wan, Y.; Yowanto, H.; Li, J.; Tao, C.; James, M. D.; Tan, C. L.; Blackburn, G. F.; Meade, T. J. *J. Am. Chem. Soc.* **2001**, *123*, 11155-11161.
- (29) Gibbs, J. M.; Park, S. J.; Anderson, D. R.; Watson, K. J.; Mirkin, C. A.; Nguyen, S. T. *J. Am. Chem. Soc.* **2005**, *127*, 1170-1178.
- (30) Taton, T. A.; Mucic, R. C.; Mirkin, C. A.; Letsinger, R. L. *J. Am. Chem. Soc.* **2000**, *122*, 6305-6306.
- (31) Jin, R. C.; Wu, G. S.; Li, Z.; Mirkin, C. A.; Schatz, G. C. *J. Am. Chem. Soc.* **2003**, *125*, 1643-1654

## Chapter 2

- (1) Chiang, C. K.; Fincher, C. R.; Park, Y. W.; Heeger, A. J.; Shirakawa, H.; Louis, E. J.; Gau, S. C.; MacDiarmid, A. G. *Phys. Rev. Lett.* **1977**, *39*, 1098-1101.
- (2) *Handbook of Conducting Polymers*; Skotheim, T. A.; Elsenbaumer, R. L.; Reynolds, J. R., Eds., 1997.
- (3) Bradley, D. D. C.; Brown, A. R.; Burn, P. L.; Burroughes, J. H.; Friend, R. H.; Greenham, N. C.; Gymer, R. W.; Holmes, A. B.; Kraft, A. M.; Marks, R. N. *Nature* **1993**, *125*, 120-133.
- (4) Greenham, N. C.; Moratti, S. C.; Bradley, D. D. C.; Friend, R. H.; Holmes, A. B. *Nature* **1993**, *365*, 628-630.
- (5) Ferraris, J. P.; Eissa, M. M.; Brotherston, I. D.; Loveday, D. C. *Chem. Mater.* **1998**, *10*, 3528-3535.
- (6) Shirota, Y.; Noma, N.; Mikawa, H. *Synth. Met.* **1987**, *18*, 399-404.
- (7) Nawa, K.; Miyawaki, K.; Imae, I.; Noma, N.; Shirota, Y. *J. Mater. Chem.* **1993**, *3*, 113-114.
- (8) Roncali, J. *Chem. Rev.* **1992**, *92*, 711-738.
- (9) Rasmussen, S. C.; Pickens, J. C.; Hutchison, J. E. *J. Heterocycl. Chem.* **1997**, *34*, 285-288.
- (10) Eales, R. M.; Hillman, A. R. *J. Electroanal. Chem.* **1988**, *250*, 219-223.
- (11) Berggren, M.; Gustafsson, G.; Inganas, O.; Andersson, M. R.; Hjertberg, T.; Wennerstroem, O. *J. Appl. Phys.* **1994**, *76*, 7530-7534.
- (12) Inganaes, O.; Berggren, M.; Andersson, M. R.; Gustafsson, G.; Hjertberg, T.; Wennerstroem, O.; Dyreklev, P.; Granstroem, M. *Synth. Met.* **1995**, *71*, 2121-2124.
- (13) McCullough, R. D.; Lowe, R. D.; Jayaraman, M.; Anderson, D. L. *J. Org. Chem.* **1993**, *58*, 904-912.
- (14) Davidson, K.; Ponsonby, A. M. *Synth. Met.* **1999**, *102*, 1512-1513.
- (15) Fujihira, M.; Do, L. M.; Koike, A.; Han, E. M. *Appl. Phys. Lett.* **1996**, *68*, 1787-1789.
- (16) Higginson, K. A.; Zhang, X. M.; Papadimitrakopoulos, F. *Chem. Mater.* **1998**, *10*, 1017-1020.

- (17) Yasuda, T.; Fujita, K.; Nakashima, H.; Tsutsui, T. *Jpn. J. Appl. Phys., Part 2* **2003**, *42*, L967-L969.
- (18) del Valle, M. A.; Cury, P.; Schrebler, R. *Electrochim. Acta* **2002**, *48*, 397-405.
- (19) Watson, K. J.; Wolfe, P. S.; Nguyen, S. T.; Zhu, J.; Mirkin, C. A. *Macromolecules* **2000**, *33*, 4628-4633.
- (20) Schwab, P.; Grubbs, R. H.; Ziller, J. W. *J. Am. Chem. Soc.* **1996**, *118*, 100-110.
- (21) Schwab, P.; France, M. B.; Ziller, J. W.; Grubbs, R. H. *Angew. Chem., Int. Ed.* **1995**, *34*, 2039-2041.
- (22) Tourillon, G.; Garnier, F. *J. Electroanal. Chem.* **1982**, *135*, 173-178.
- (23) Zotti, G.; Schiavon, G. *J. Electroanal. Chem.* **1984**, *163*, 385-388.
- (24) Laakso, J.; Osterholm, J. E.; Nyholm, P.; Stubb, H.; Punkka, E. *Synth. Met.* **1990**, *37*, 145-150.
- (25) Stein, P. C.; Bolognesi, A.; Catellani, M.; Destri, S.; Zetta, I. *Synth. Met.* **1991**, *41*, 559-562.
- (26) Yamamoto, T.; Morita, A.; Maruyama, T.; Zhou, Z. H.; Kanbara, T.; Sanechika, K. *Polym. J.* **1990**, *22*, 187-190.
- (27) Wrighton, M. S.; Palazzotto, M. C.; Bocarsly, A. B.; Bolts, J. M.; Fischer, A. B.; Nadjro, L. *J. Am. Chem. Soc.* **1978**, *100*, 7264-7271.
- (28) Kossmehl, G.; Greczmiel, T.; Plieth, W. *Macromol. Chem. Phys.* **1994**, *195*, 3655-3664.
- (29) Krische, B.; Zagorska, M. *Synth. Met.* **1989**, *28*, C263-C268.
- (30) Kittlesen, G. P.; White, H. S.; Wrighton, M. S. *J. Am. Chem. Soc.* **1984**, *106*, 7389-7396.
- (31) Morvant, M. C.; Reynolds, J. R. *Synth. Met.* **1998**, *92*, 57-61.
- (32) Paul, E. W.; Ricco, A. J.; Wrighton, M. S. *J. Phys. Chem.* **1985**, *89*, 1441-1447.
- (33) Thackeray, J. W.; White, H. S.; Wrighton, M. S. *J. Phys. Chem.* **1985**, *89*, 5133-5140.
- (34) Kaneto, K.; Kohno, Y.; Yoshino, K.; Inuishi, Y. *Chem. Commun.* **1983**, 382-383.
- (35) Groenendaal, L.; Zotti, G.; Aubert, P. H.; Waybright, S. M.; Reynolds, J. R. *Adv. Mater.* **2003**, *15*, 855-879.
- (36) Imae, I.; Nawa, K.; Ohsedo, Y.; Noma, N.; Shirota, Y. *Macromolecules* **1997**, *30*, 380-386.

- (37) Ohsedo, Y.; Imae, I.; Noma, N.; Shirota, Y. *Synth. Met.* **1996**, *81*, 157-162.
- (38) Li, F.; Albery, W. J. *Electrochim. Acta* **1992**, *37*, 393-401.
- (39) Schrebler, R.; Grez, P.; Cury, P.; Veas, C.; Merino, M.; Gomez, H.; Cordova, R.; del Valle, M. A. *J. Electroanal. Chem.* **1997**, *430*, 77-90.
- (40) Shim, S.-Y.; Lim, D.-K.; Nam, J.-M. *Nanomed.* **2008**, *3*, 215-32.
- (41) Chen, W.; Grouquist, D.; Roark, J. *J. Nanosci. and Nanotechnol.* **2002**, *2*, 47-53.
- (42) Barazzouk, S.; Hotchandani, S. *J. Appl. Phys.* **2004**, *96*, 7744-7746.
- (43) Ozin, G. A. *Adv. Mater.* **1992**, *4*, 612-649.
- (44) Hulteen, J. C.; Martin, C. R. *J. Mater. Chem.* **1997**, *7*, 1075-1087.
- (45) Nicewarner-Pena, S. R.; Freeman, R. G.; Reiss, B. D.; He, L.; Pena, D. J.; Walton, I. D.; Cromer, R.; Keating, C. D.; Natan, M. J. *Science* **2001**, *294*, 137-141.
- (46) Bowers, M. J.; McBride, J. R.; Rosenthal, S. J. *J. Am. Chem. Soc.* **2005**, *127*, 15378-15379.
- (47) Kang, Y.; Kim, D. *Sol. Energy Mater. Sol. Cells* **2006**, *90*, 166-174.
- (48) Stoermer, R. L.; Cederquist, K. B.; McFarland, S. K.; Sha, M. Y.; Penn, S. G.; Keating, C. D. *J. Am. Chem. Soc.* **2006**, *128*, 16892-16903.
- (49) Park, S.; Chung, S. W.; Mirkin, C. A. *J. Am. Chem. Soc.* **2004**, *126*, 11772-11773.
- (50) Park, S.; Lim, J. H.; Chung, S. W.; Mirkin, C. A. *Science* **2004**, *303*, 348-351.
- (51) Li, X. H.; Lu, M.; Li, H. L. *J. Appl. Polym. Sci.* **2002**, *86*, 2403-2407.
- (52) Wang, S.; Querner, C.; Emmons, T.; Drndic, M.; Crouch, C. H. *J. Phys. Chem. B* **2006**, *110*, 23221-23227.
- (53) Chung, I.; Witkoskie, J. B.; Cao, J. S.; Bawendi, M. G. *Phys. Rev. E: Stat. Phys., Plasmas, Fluids*, **2006**, *73*, 011106-1 - 011106-7.
- (54) Cannone, F.; Chirico, G.; Bizzarri, A. R.; Cannistraro, S. *J. Phys. Chem. B* **2006**, *110*, 16491-16498.
- (55) Fan, C. H.; Wang, S.; Hong, J. W.; Bazan, G. C.; Plaxco, K. W.; Heeger, A. J. *Proc. Natl. Acad. Sci. U. S. A.* **2003**, *100*, 6297-6301.
- (56) Li, K. R.; Stockman, M. I.; Bergman, D. J. *Phys. Rev. Lett.* **2003**, *91*, 227402-1 - 227402-4.



- (57) Pangborn, A. B.; Giardello, M. A.; Grubbs, R. H.; Rosen, R. K.; Timmers, F. J. *Organometallics* **1996**, *15*, 1518-1520.

### Chapter 3

- (1) Bertram, L.; Blacker, D.; Mullin, K.; Keeney, D.; Jones, J.; Basu, S.; Yhu, S.; McInnis, M. G.; Go, R. C. P.; Vekrellis, K.; Selkoe, D. J.; Saunders, A. J.; Tanzi, R. E. *Science* **2000**, *290*, 2302-2303.
- (2) Martin, E. R.; Scott, W. K.; Nance, M. A.; Watts, R. L.; Hubble, J. P.; Koller, W. C.; Lyons, K.; Pahwa, R.; Stern, M. B.; Colcher, A.; Hiner, B. C.; Jankovic, J.; Ondo, W. G.; Allen, F. H.; Goetz, C. G.; Small, G. W.; Masterman, D.; Mastaglia, F.; Laing, N. G.; Stajich, J. M.; Ribble, R. C.; Booze, M. W.; Rogala, A.; Hauser, M. A.; Zhang, F. Y.; Gibson, R. A.; Middleton, L. T.; Roses, A. D.; Haines, J. L.; Scott, B. L.; Pericak-Vance, M. A.; Vance, J. M. *JAMA* **2001**, *286*, 2245-2250.
- (3) Miglani, G. S. *Advanced Genetics*; Alpha Science: Pangbourne, UK, 2002.
- (4) Syvanen, A. C.; Soderlund, H. *Nat. Biotechnol.* **2002**, *20*, 349-350.
- (5) Storhoff, J. J.; Marla, S. S.; Bao, P.; Hagenow, S.; Mehta, H.; Lucas, A.; Garimella, V.; Patno, T.; Buckingham, W.; Cork, W.; Muller, U. R. *Biosens. Bioelectron.* **2004**, *19*, 875-883.
- (6) Ferguson, J. A.; Boles, T. C.; Adams, C. P.; Walt, D. R. *Nat. Biotechnol.* **1996**, *14*, 1681-1684.
- (7) Hakala, H.; Heinonen, P.; Iitia, A.; Lonnberg, H. *Bioconjugate Chem.* **1997**, *8*, 378-384.
- (8) Storhoff, J. J.; Elghanian, R.; Mucic, R. C.; Mirkin, C. A.; Letsinger, R. L. *J. Am. Chem. Soc.* **1998**, *120*, 1959-1964.
- (9) Gaylord, B. S.; Heeger, A. J.; Bazan, G. C. *J. Am. Chem. Soc.* **2003**, *125*, 896-900.
- (10) Marti, A. A.; Puckett, C. A.; Dyer, J.; Stevens, N.; Jockusch, S.; Ju, J.; Barton, J. K.; Turro, N. J. *J. Am. Chem. Soc.* **2007**, *129*, 8680-8681.
- (11) Yu, C. J.; Wan, Y.; Yowanto, H.; Li, J.; Tao, C.; James, M. D.; Tan, C. L.; Blackburn, G. F.; Meade, T. J. *J. Am. Chem. Soc.* **2001**, *123*, 11155-11161.
- (12) Gibbs, J. M.; Park, S. J.; Anderson, D. R.; Watson, K. J.; Mirkin, C. A.; Nguyen, S. T. *J. Am. Chem. Soc.* **2005**, *127*, 1170-1178.
- (13) Mirkin, C. A.; Letsinger, R. L.; Mucic, R. C.; Storhoff, J. J. *Nature* **1996**, *382*, 607-609.
- (14) Drabek, J. *Electrophoresis* **2001**, *22*, 1024-1045.
- (15) Taton, T. A.; Mucic, R. C.; Mirkin, C. A.; Letsinger, R. L. *J. Am. Chem. Soc.* **2000**, *122*, 6305-6306.

- (16) Jin, R. C.; Wu, G. S.; Li, Z.; Mirkin, C. A.; Schatz, G. C. *J. Am. Chem. Soc.* **2003**, *125*, 1643-1654.
- (17) Park, S. Y.; Lee, J. S.; Georganopoulou, D.; Mirkin, C. A.; Schatz, G. C. *J. Phys. Chem. B* **2006**, *110*, 12673-12681.
- (18) Gibbs-Davis, J. M.; Schatz, G. C.; Nguyen, S. T. *J. Am. Chem. Soc.* **2007**, *129*, 15535-15540.
- (19) Long, H.; Kudlay, A.; Schatz, G. C. *J. Phys. Chem. B* **2006**, *110*, 2918-2926.
- (20) Kudlay, A.; Gibbs, J. M.; Schatz, G. C.; Nguyen, S. T.; de la Cruz, M. O. *J. Phys. Chem. B* **2007**, *111*, 1610-1619.
- (21) Park, S. Y.; Stroud, D. *Phys. Rev. B: Condens. Matter* **2003**, *68*, 224201/1-224201/11.
- (22) Lukatsky, D. B.; Frenkel, D. *J. Chem. Phys.* **2005**, *122*, 214904/1-214904/11.
- (23) Lutz, J. F. *Angew. Chem., Int. Ed.* **2007**, *46*, 1018-1025.
- (24) Watson, K. J.; Park, S. J.; Im, J. H.; Nguyen, S. T.; Mirkin, C. A. *J. Am. Chem. Soc.* **2001**, *123*, 5592-5593.
- (25) Mammen, M.; Shakhnovich, E. I.; Deutch, J. M.; Whitesides, G. M. *J. Org. Chem.* **1998**, *63*, 3821-3830.
- (26) Shchepinov, M. S.; Mir, K. U.; Elder, J. K.; Frank-Kamenetskii, M. D.; Southern, E. M. *Nucleic Acids Res.* **1999**, *27*, 3035-3041.
- (27) Lewis, F. D.; Wu, Y. S.; Liu, X. Y. *J. Am. Chem. Soc.* **2002**, *124*, 12165-12173.
- (28) Salunkhe, M.; Wu, T. F.; Letsinger, R. L. *J. Am. Chem. Soc.* **1992**, *114*, 8768-8772.
- (29) Kibbe, W. A. *Nucleic Acids Res.* **2007**, *35*, W43-W46.
- (30) Erdelyi, M.; Gogoll, A. *J. Org. Chem.* **2001**, *66*, 4165-4169.
- (31) Petricci, E.; Radi, M.; Corelli, F.; Botta, M. *Tetrahedron Lett.* **2003**, *44*, 9181-9184.
- (32) Huang, C. C.; Lin, Y. C.; Lin, P. Y.; Chen, Y. J. *Eur. J. Org. Chem.* **2006**, 4510-4518.
- (33) Chandra, K. L.; Zhang, S.; Gorman, C. B. *Tetrahedron* **2007**, *63*, 7120-7132.
- (34) Hu, X.; Tierney, M. T.; Grinstaff, M. W. *Bioconjugate Chem.* **2002**, *13*, 83-89.
- (35) Miller, G. P.; Kool, E. T. *Org. Lett.* **2002**, *4*, 3599-3601.
- (36) Miller, G. P.; Kool, E. T. *J. Org. Chem.* **2004**, *69*, 2404-2410.

- (37) Pangborn, A. B.; Giardello, M. A.; Grubbs, R. H.; Rosen, R. K.; Timmers, F. J. *Organometallics* **1996**, *15*, 1518-1520.

## Chapter 4

- (1) Kleppe, K.; Ohtsuka, E.; Kleppe, R.; Molineux, I.; Khorana, H. G. *J. Mol. Biol.* **1971**, *56*, 341-361.
- (2) Mullis, K.; Faloona, F.; Scharf, S.; Saiki, R.; Horn, G.; Erlich, H. *Cold Spring Harbor Symp. Quant. Biol.* **1986**, *51*, 263-273.
- (3) Siebert, P. D.; Chenchik, A.; Kellogg, D. E.; Lukyanov, K. A.; Lukyanov, S. A. *Nucleic Acids Res.* **1995**, *23*, 1087-1088.
- (4) Hengen, P. N. *Trends Biochem. Sci.* **1995**, *20*, 372-373.
- (5) Stoeva, S. I.; Lee, J. S.; Thaxton, C. S.; Mirkin, C. A. *Angew. Chem., Int. Ed.* **2006**, *45*, 3303-3306.
- (6) Elghanian, R.; Storhoff, J. J.; Mucic, R. C.; Letsinger, R. L.; Mirkin, C. A. *Science* **1997**, *277*, 1078-1081.
- (7) Popielarski, S. R.; Pun, S. H.; Davis, M. E. *Bioconjugate Chem.* **2005**, *16*, 1063-1070.
- (8) Gu, F.; Zhang, L.; Teply, B. A.; Mann, N.; Wang, A.; Radovic-Moreno, A. F.; Langer, R.; Farokhzad, O. C. *Proc. Natl. Acad. Sci. U. S. A.* **2008**, *105*, 2586-2591.
- (9) Pan, D.; Turner, J. L.; Wooley, K. L. *Chem. Commun.* **2003**, 2400-2401.
- (10) Yoon, T. J.; Yu, K. N.; Kim, E.; Kim, J. S.; Kim, B. G.; Yun, S. H.; Sohn, B. H.; Cho, M. H.; Lee, J. K.; Park, S. B. *Small* **2006**, *2*, 209-215.
- (11) Wei, Q. S.; Ji, J.; Shen, J. C. *Macromol. Rapid Commun.* **2008**, *29*, 645-650.
- (12) Gao, Z. S.; Varshney, S. K.; Wong, S.; Eisenberg, A. *Macromolecules* **1994**, *27*, 7923-7927.
- (13) Zhang, L. F.; Eisenberg, A. *Polym. Adv. Technol.* **1998**, *9*, 677-699.
- (14) Bertin, P. A.; Watson, K. J.; Nguyen, S. T. *Macromolecules* **2004**, *37*, 8364-8372.
- (15) Zhang, L. F.; Shen, H. W.; Eisenberg, A. *Macromolecules* **1997**, *30*, 1001-1011.
- (16) Bertin, P. A.; Gibbs, J. M.; Shen, C. K. F.; Thaxton, C. S.; Russin, W. A.; Mirkin, C. A.; Nguyen, S. T. *J. Am. Chem. Soc.* **2006**, *128*, 4168-4169.
- (17) Number of terthiophene (TTT) molecules per PNP =  $(v \times \rho \times w \times N_A)/MW$ ; where  $v$  = volume of a PNP with 200 nm diameter =  $4/3\pi r^3 = 4.19 \times 10^{-15} \text{ cm}^3$ ,  $\rho$  = density  $\sim 1.0 \text{ g/cm}^3$ ,  $w$  = weight ratio of TTT in TTT<sub>60-b</sub>-PEG(OTs)<sub>15</sub> = 0.7 g(TTT)/g(TTT<sub>60-b</sub>-

PEG(OTs)<sub>15</sub>),  $MW$  = molecular weight of TTT = 247 g/mole, and  $N_A$  = Avogadro's Number =  $6.022 \times 10^{23}$  molecules/mole.

- (18) Bertin, P. A.; Smith, D. D.; Nguyen, S. T. *Chem. Commun.* **2005**, 3793-3795.
- (19) Yang, G.; Ran, Y. Q.; Yalkowsky, S. H. *J. Pharm. Sci.* **2002**, *91*, 517-533.
- (20) Nandi, I.; Bari, M.; Joshi, H. *AAPS PharmSciTech* **2003**, *4*, 71-79.
- (21) van Tilborg, G. A. F.; Mulder, W. J. M.; Deckers, N.; Storm, G.; Reutelingsperger, C. P. M.; Strijkers, G. J.; Nicolay, K. *Bioconjugate Chem.* **2006**, *17*, 741-749.
- (22) Watson, K. J.; Wolfe, P. S.; Nguyen, S. T.; Zhu, J.; Mirkin, C. A. *Macromolecules* **2000**, *33*, 4628-4633.
- (23) Schwab, P.; France, M. B.; Ziller, J. W.; Grubbs, R. H. *Angew. Chem., Int.* **1995**, *34*, 2039-2041.
- (24) Schwab, P.; Grubbs, R. H.; Ziller, J. W. *J. Am. Chem. Soc.* **1996**, *118*, 100-110.
- (25) Nguyen, D.; Zhong, X. F.; Williams, C. E.; Eisenberg, A. *Macromolecules* **1994**, *27*, 5173-5181.
- (26) WilczekVera, G.; Danis, P. O.; Eisenberg, A. *Macromolecules* **1996**, *29*, 4036-4044.
- (27) Birks, J. B. *Rep. Prog. Phys.* **1975**, *38*, 903-974.
- (28) For examples of photodiode spectral response curves see: <http://sales.hamamatsu.com/assets/html/ssd/si-photodiode/index.htm>, accessed: August 08, 2008.
- (29) Stepp, B. R.; Nguyen, S. T. *Macromolecules* **2004**, *37*, 8222-8229.
- (30) Jang, S.-Y.; Sotzing, G. A.; Marquez, M. *Macromolecules* **2002**, *35*, 7293-7300.
- (31) Yu, Y. S.; Zhang, L. F.; Eisenberg, A. *Macromolecules* **1998**, *31*, 1144-1154.
- (32) For commercial example of tosylated nanoparticles see: [http://tools.invitrogen.com/content/sfs/brochures/Surface\\_Activated\\_Dynabeads\\_web.pdf](http://tools.invitrogen.com/content/sfs/brochures/Surface_Activated_Dynabeads_web.pdf), accessed: August 08, 2008.
- (33) Zhang, N.; Appella, D. H. *J. Am. Chem. Soc.* **2007**, *129*, 8424-8425.
- (34) Boman, F. C.; Musorrafiti, M. J.; Gibbs, J. M.; Stepp, B. R.; Salazar, A. M.; Nguyen, S. B. T.; Geiger, F. M. *J. Am. Chem. Soc.* **2005**, *127*, 15368-15369.
- (35) Pangborn, A. B.; Giardello, M. A.; Grubbs, R. H.; Rosen, R. K.; Timmers, F. J. *Organometallics* **1996**, *15*, 1518-1520.

## Chapter 5

- (1) Gaupp, C. L.; Welsh, D. M.; Rauh, R. D.; Reynolds, J. R. *Chem. Mater.* **2002**, *14*, 3964-3970.
- (2) Leriche, P.; Blanchard, P.; Frere, P.; Levillain, E.; Mahon, G.; Roncali, J. *Chem. Commun.* **2006**, 275-277.
- (3) Zhao, J.; Jensen, L.; Sung, J. H.; Zou, S. L.; Schatz, G. C.; Van Duyne, R. P. *J. Am. Chem. Soc.* **2007**, *129*, 7647-7656.

**Curriculum Vitae**



## Brian Richard Stepp

- BORN** Hendersonville, North Carolina, 1978
- ADDRESS** 1900 Blueslate Ct., Raleigh, NC 27603
- EDUCATION**
- NORTHWESTERN UNIVERSITY - Evanston, IL**  
 Doctor of Philosophy, Organic Chemistry, July 2008  
 Thesis Advisor: Prof. SonBinh T. Nguyen
- NORTH CAROLINA STATE UNIVERSITY - Raleigh, NC**  
 Bachelor of Science, Chemistry, May 2002  
 Bachelor of Science, Pulp and Paper Science and Technology, May 2002  
 Advisor: Prof. Christopher B. Gorman
- EXPERIENCE**
- NORTHWESTERN UNIVERSITY - Evanston, IL**  
**Graduate Research Assistant, November 2002–July 2008**
- Acquired funds, purchased equipment, set-up, and maintained a shared-use bio-molecule synthesis and characterization facility with capabilities including: DNA and Protein synthesis, HPLC purification, UV-vis spectroscopy, and fluorometry
  - Synthesized oligonucleotides with covalently bound small-organic molecules and evaluate the effect of unit-structure on oligonucleotide hybridization/dehybridization properties
  - Designed and synthesized fluorescent/redox-active polymer nanoparticles with surface-bound oligonucleotides for self-amplified gene detection applications
  - Synthesized and characterized cross-linked poly(norbornene-terthiophene) films and noble metal-poly(norbornene-terthiophene) nanoscale rods for nanoscale electronic applications.
  - Served as mentor for seven undergraduate researchers working as part of the Research Experience for Undergraduates (REU) summer program and as undergraduate research assistants during the school year
    1. **Omar Abdullah:** Paper in undergraduate journal *Nanoscope*
    2. **Dorothea L.F. Koh:** Paper in undergraduate journal *Northwestern Undergraduate Research Journal*; Paper in *Journal of the American Chemical Society*; Outstanding undergraduate honors thesis award, Northwestern biomedical engineering (BME) department, 2006; Best poster, Northwestern undergraduate research symposium, Spring 2006; Graduate school in BME at Stanford
    3. **Anup B. Shah:** Graduate school in mechanical engineering at Stanford
    4. **Megan M. Boyle:** Paper in *Polymer Preprints*; Paper in undergraduate journal, *Nanoscope*; Paper to be submitted, *Adv. Mater.*; Graduate school in chemistry at Northwestern
    5. **Sharan R. Srinivasan:** Paper in *Polymer Preprints*; Paper in undergraduate journal, *Nanoscope*; Paper to be submitted, *Adv. Mater.*
    6. **Emily C. Mirkin:** Paper in undergraduate journal, *Nanoscope*
    7. **David G. Dillon:** Undergraduate honors thesis in chemistry, Spring 2008
  - Collaborated with Profs. George Schatz and Franz Geiger in the Northwestern chemistry department and Prof. Vinayak Dravid in the Northwestern materials science and engineering department on the theory and materials chemistry of thin organic and bio-organic films
  - Participated in Preparing Future Faculty (PFF), a training program for graduate students who aim for a career in academia
- NORTHWESTERN UNIVERSITY - Evanston, IL**  
**Tutor and Teaching Assistant, September 2000–July 2008**
- Taught five quarters of organic chemistry lab sessions
  - Tutored students independently through three quarters of sophomore organic chemistry

**NORTH CAROLINA STATE UNIVERSITY - Raleigh, NC****Undergraduate Research Assistant, August 2000–May 2002**

- Synthesized water soluble dendrimers with redox active iron sulfur cores
- Completed multi-step synthesis on an individual project

**NORTH CAROLINA STATE UNIVERSITY - Raleigh, NC****Teaching Assistant, January 2001–May 2001**

- Taught second-semester undergraduate organic chemistry lab course
- Independently responsible for a class of 20 students

**RESEARCH SKILLS**

- Proficient in reaction design and multi-step organic synthesis
- Capable of efficient project management and mentorship
- Skilled in air-free techniques and purification methods including column-chromatography, TLC, preparatory-HPLC, and various distillations
- Expertise in HPLC, NMR, UV/vis, fluorometry, optical/fluorescence microscopy, TEM, SEM, and electrochemistry
- Competent in using software packages like ChemDraw Pro, Corel Draw, Spartan, Agilent Tech. ChemStations and scientific databases like SciFinder and Beilstein Commander
- Mechanically inclined, with the ability to diagnose and repair instrumental problems

**AWARDS and RECOGNITION**

**Best Poster Award**, Colloids Division, ACS National meeting in Chicago, Spring 2007

**Work Highlighted**, "Latest News" Chemical and Engineering News, 2007 85(23)

**NSF/NSEC Fellowship Award**, Northwestern University, Fall 2006

**NSF/NSEC Outstanding Research Award**, Northwestern University, Fall 2006

**Undergraduate Research Award Grant**, North Carolina State University, Fall 2001

**PUBLICATIONS**

1. "Terthiophene-containing Polymer Nanoparticle Probe for Amplified DNA Detection" **Stepp, B. R.**; Boyle, M. M.; Srinivasan, S. R.; Nguyen, S. T. *Adv. Mater.*, **2008**, to be submitted.
2. "Progress toward "Click"-based Small-Molecule DNA Hybrids: Synthesis of Precursors to Acetylene Terminated Cores and Azide-Functionalized Arms" Mirkin, E.M.; Stepp, B.R.; Nguyen, S.T. *Nanoscape*, **2008**, 5, 4-13.
3. "DNA at Aqueous/Solid Interfaces—Chirality-Based Detection via Second Harmonic Generation Activity" Boman, F. C.; Gibbs-Davis, J. M.; Heckman, L.; **Stepp, B. R.**; Nguyen, S. T.; Geiger, F. M. *J. Am. Chem. Soc.*, **2008** 130 (30) ASAP.
4. "Cooperative Melting in Caged Dimer of Rigid Small Molecule-DNA Hybrids" **Stepp, B. R.**; Gibbs-Davis, J. M.; Koh, D. L. F.; Nguyen, S. T. *J. Am. Chem. Soc.*, **2008**, 130 (30), 9628–9629.
5. "Making "Sense" of DNA" Stokes, G. Y.; Gibbs-Davis, J. M.; Boman, F. C.; **Stepp, B. R.**; Condie, A. G.; Nguyen, S. T.; Geiger, F. M. *J. Am. Chem. Soc.*, **2007**, 129 (24), 7492-7493.
6. "Synthesis of polymer nanoparticles from amphiphilic block copolymers for DNA detection via amplified fluorescence" **Stepp, B. R.**; Boyle, M. M.; Srinivasan, S.; Smith, D.; Nguyen, S. T. *Polym. Prepr. (Am. Chem. Soc., Div. Polym. Chem.)*, **2006**, 47(2), 791.
7. "Small-Molecule DNA Hybrid Model Studies" Koh, D. L. F.; **Stepp, B. R.**; Nguyen, S. T. *Northwestern Undergraduate Research Journal*, **2006**, 3, 40-50.
8. "Development of Bioorganic Polymer Composites for the Directed Assembly of Functional Materials" Abdullah, O.; **Stepp, B. R.**; Nguyen, S. T. *Nanoscape*, **2006**, 3, 6-11.
9. "DNA Single Strands Tethered to Fused Quartz/Water Interfaces Studied by Second Harmonic Generation" Boman, F. C.; Musorrafiti, M. J.; Gibbs, J. M.; **Stepp, B. R.**; Salazar, A. M.; Nguyen, S. T.; Geiger, F. M. *J. Am. Chem. Soc.*, **2005**, 127(44), 15368-15369.

10. "Organic-DNA hybrids: Detection capabilities and thermal properties" Davis, J. G.; Park, S. -J.; **Stepp, B. R.**; Modi, P.; Koh, D. L. F.; Mirkin, C. A.; Nguyen, S. T. *Polym. Prepr. (Am. Chem. Soc., Div. Polym. Chem.)*, **2005**, 46(2), 1142-1143.
11. "Enhancement of the Physical Properties of Poly((2-terthiophenyl)norbornene) through Cross-Linking Pendant Terthiophenes" **Stepp, B. R.**; Nguyen, S. T. *Macromolecules*, **2004**, 37(22), 8222-8229.

**SELECTED  
PRESENTATIONS**

- "Modular approaches toward small-molecule DNA hybrids" **Stepp, B. R.**; Gibbs-Davis, J. M.; Koh, D. L. F.; Nguyen, S. T., Talk given at the 234th ACS National Meeting, Aug. 19-23, **2007**.
- "Polymer Nanoparticles Synthesized from Amphiphilic Block Copolymers as Probes for DNA Detection" **Stepp, B. R.**; Boyle, M.; Srinivasan, S.; Smith, D.; Davis, J. G.; Nguyen, S. T., Poster presented at the 233rd ACS National Meeting, Mar. 25-29, **2007**.
- "Small-Molecule DNA Hybrids (SMDH's): Syntheses and Recognition Properties" **Stepp, B. R.**; Davis, J. G.; Koh, D. L. F.; Nguyen, S. T., Poster presented at the 232nd ACS National Meeting, Sept. 10-14, **2006**.
- "Synthesis of Polymer Nanoparticles from Amphiphilic Block Copolymers for DNA Detection via Amplified Fluorescence" **Stepp, B. R.**; Boyle, M.; Srinivasan, S.; Nguyen, S. T., Poster presented at the 232nd ACS National Meeting, Sept. 10-14, **2006**.
- "Synthesis and Characterization of AAO-Templated Metal-Polymer Nanorods Incorporating Cross-Linked Poly((2-terthiophenyl)norbornene)" **Stepp, B. R.**; Shah, A. B.; Nguyen, S. T., Poster presented at the 232nd ACS National Meeting, Sept. 10-14, **2006**.
- "Small-Molecule-DNA Hybrid Materials" **Stepp, B. R.**, Northwestern University Chemistry Departmental Seminar, June, **2005**.